Faculty of Science and Engineering

WASM: Minerals, Energy and Chemical Engineering

Forward Modelling and Inversion of the Ultrasonic Wave Propagation Through a Homogeneous and Porous Rock

Michel Nzikou Mamboukou

This thesis is presented for the Degree of

Doctor of Philosophy

of

Curtin University

March 2019

Declaration

To the best of my knowledge and belief this thesis contains no material previously published by any other person except where due acknowledgement has been made.

This thesis contains no material which has been accepted for the award of any other degree or diploma in any university.

Signature: 

Date: _____March 6, 2018_____

Acknowledgements

I would like to express my sincere gratitude to my supervisor, Professor Boris Gurevich, for his leadership, observation and guidance during my Ph.D. His solid support and continuous input in this research helped me successfully complete my Ph.D. I am greatly inspired and impressed by his immense expertise. He has given me much insightful advice and many comments that have assisted me to complete my thesis. With his guidance, I learned how to conduct research with confidence, and I enjoy the research process more now. He is not only a supervisor for me but a mentor who guides my understanding of science.

I am thankful for the funding provided by the Curtin Reservoir Geophysics Consortium (CRGC). Thank you for their financial support without it this project would not have been possible.

Thank you to Professor Maxim Lebedev for making the Curtin Rock Physics laboratory available for my project. Thank you Dr Mahyar Madadi for his support in computational modelling, numerical simulation and coding insights which inspired me to became expert in finite element methods software like Abaqus. A special thank you to the members of the Geophysics department. Cheers to my colleagues Alexey Yurikov and Nazanin Nourifard for sharing their experimental data. Big thank you to Dr Miroslav Brajanovski for working with me: your help is much appreciated.

Of course, my adventure would not happen without God and my family. I dedicate this work to my late father Michel M. Nzikou and my mother Lembe Rose. I am especially grateful to my very special “frangine” Princia Nzikou Mamboukou who continuously supported me from day one. A big thank you to Mary Kanyingi for helping me strike through this journey.

Abstract

The main goal of this thesis is the estimation of the elastic and viscoelastic parameters using the inversion of measured ultrasonic waveforms. The developed inversion workflow contains a number of optimization functions that minimize the error between measured and synthetic waveforms.

Elastic properties of homogeneous and isotropic samples are usually estimated from ultrasonic data using traveltimes estimated via methods such as first break picking or cross-correlation. The accuracy of these methods can be affected by velocity dispersion and attenuation. Therefore, developing alternative methods that do not suffer (or suffer to a lesser degree) from these effects, particularly in ultrasonic frequencies, is very important.

To model waveforms in elastic media, I developed Python modules that automate the use of commercial software Abaqus. Then I developed an inversion workflow tailored specifically for a controlled transmission experiment using ultrasonic source and receiver. I then extended the Python modules to viscoelastic media using the so-called Prony formulation with single relaxation time.

To build a robust inversion model that estimates the viscoelastic parameters, I first designed a forward modelling workflow in Abaqus for cylindrical samples. Then, I estimated the elastic parameters of known homogeneous and isotropic samples by a grid-search algorithm. I applied this approach to an ultrasonic experiment performed during gas desorption in the nanoporous glass. In the modelling, I assumed that, at a given pressure, the cylindrical sample effectively consists of two distinct parts: a fully saturated inner core and an outer shell with uniform liquid saturation of about 40 %. The simulation results give the vapour pressure dependency of the phase velocity and of the apparent attenuation, which agrees very well with published laboratory data. This demonstrates consistency and high accuracy of the developed inversion workflow and the validity of the underlying two-layer model.

Finally, the inversion was applied to estimate velocity and attenuation using ultrasonic waveforms recorded for an air-dry sandstone sample at different relative humidities. I used mode separation to perform *P*- and *S*-waves waveform inversion separately in the time domain, allowing the estimation of *P*- and *S*-wave velocities and attenuation. These velocity and attenuation estimate largely agree with estimates by the centroid frequency shift method.

Contents

Chapter 1: Introduction

Real materials exposed to an external force change their shape and volume i.e. they become deformed. The magnitude and form of the deformation are related to the material properties as well as the magnitude of the force the material is exposed to. If the deformed material returns to its initial state after force ceases to act, such a material is called elastic. The elastic properties control how the material will deform in the presence of applied force so they are macroscopic attributes originating from the microstructure of the material.

The elastic properties of such material can be measured by a number of methods. Usually, the elastic parameters are measured indirectly using waves that propagate through the material this is because in exploration projects it is easier to measure quantities that are directly related to elastic parameters such as the velocity and attenuation of the wave.

These measurements have applications in exploration geophysics, medical imaging, and non-destructive testing (NDT). In exploration seismology, waves are used to delineate aquifers or find mineral bodies such as copper, gold and iron etc. Information that can be obtained from seismic data is related to the velocity and attenuation of different wave modes. But these wave attributes are uniquely related to the structure of the material. Therefore, other measurements are needed to gain a deeper insight into the properties of the medium and to calibrate the field measurements. Ultrasonic transmission methods performed on rock samples in the laboratory are one of the additional techniques to extract important parameters of real rocks. The data obtained from this method can be easily processed and used to estimate the velocity and attenuation, which can then be used to calibrate seismic surveys during exploration or production in order to better estimate subsurface properties.

A rock's inner structure always has one or more characteristic spatial scales, such as grain or pore size. Also, there can be inhomogeneity in a structure such as fractures or partially saturated regions. During wave propagation through such materials, some micro processes are triggered so that the energy is dissipated, causing wave decay known as attenuation, which can be measured by inspecting the recorded waveforms. When attenuation occurs, it is always accompanied by velocity dispersion (dependency of wave velocity on frequency).

Because of the above-mentioned effect, there is a need to compare wave velocities measured at different frequencies. Therefore, waveform attenuation and velocity dispersion is a topic of

interest in exploration geophysics, because they are related to both the rock and fluid properties and can provide useful insight in tracing the hydrocarbon from subsurface seismic techniques.

Ultrasonic measurements are done on core samples using a source and receiver transducer. The transducers are made from piezoelectric material that produces electric voltage as a consequence of applied mechanical stress and vice versa. For a standard measurement, the sample is sandwiched between source and receiver transducers. Better contact between the transducers and the sample allows higher-quality data. Usually, the recorded waveforms allow the estimation of the traveltimes and consequently the wave velocities.

To estimate the elastic properties, the first step is to measure traveltimes from the recorded waveforms. This is measured using either manual first break picking or another method such as cross-correlation. Knowing the traveltimes and the measured sample length, the velocity of different wave modes are estimated. Wave velocities are directly related to both compressional and shear moduli and density. From the measured density and estimated velocities, the elastic moduli are then calculated. During the wave propagation, part of the energy is dissipated in the form of heat, causing the amplitude to decay, which can be directly measured. From it, one can calculate the attenuation coefficients.

The shape of the measured waveforms is influenced by many factors such as boundary reflections and unwanted noise, sample inhomogeneities and viscous pore fluid causing attenuation. These effects can cause errors in the quantitative estimation of the elastic parameters. Hence, developing an alternative method that minimizes misfit error between observed and measured data, might be beneficial in optimising laboratory setups that suffer from unwanted effects.

The best method so far for estimating elastic and viscoelastic properties is waveform inversion. For this to be reliable, forward modelling is needed. Prior to attempting any inversion, it is best practice to have a sensible agreement between modelled and measured data from known samples. Investigating the wave propagation in a homogeneous and isotropic sample can help understand complex media such as a viscoelastic medium. This process can be very challenging when dealing with various layers of the earth. However, in the ultrasonic measurement of a homogeneous sample only a few parameters are needed for inversion.

In order to achieve higher accuracy from laboratory measurements, several factors such as the source input, the sample and transducer contact geometry should be accounted for. In this

study, the modelling of transducer source and receiver is bypassed either by using a directly measured input signal or by cutting it from the reference waveform.

In this thesis I develop a numerical method that aims to estimate the elastic and viscoelastic properties of rock samples using waveform inversion. The specific objectives are as follows:

- Develop a forward model that matches the measured ultrasonic waveforms
- Design a workflow to use a source signal from laboratory measurements for modelling purposes
- Create an inversion algorithm
- Optimize the workflow
- Test the workflow on synthetic data, and
- Apply the algorithm to measured data.

This thesis focuses on forward and inversion modelling using Abaqus software. First, a forward model of the ultrasonic wave in a homogeneous and isotropic medium is developed. Then, to avoid a costly iterative search of the elastic parameters, I develop an automated model to estimate the elastic parameters such as Young Modulus (E), Poisson ratio (ν), *P*-wave velocity (V_P), *S*-wave velocity (Vs) and attenuation quality factors (Q_P and Q_S)

The structure of the thesis is as follows:

In chapter 2, a brief introduction presents various ways to measure elastic and viscoelastic properties in the laboratory. Emphasis is given to ways of estimating both the velocity and attenuation. Also, their advantages and shortcoming are highlighted. Similarly, a brief inversion overview is discussed.

In chapter 3, a homogeneous and isotropic sample is considered and an efficient forward modelling workflow is introduced and used to build the synthetic waveforms. To achieve the best model, the transducer width is ignored and assumed to be the transducer sample surface contact. Using known material and transducer parameters, I proceed with Ricker wavelet source input as a test in the forward model. To check the robustness of the workflow, I use both *P*- and *S*-wave sources to investigate the waveform convergence.

Chapter 4 extends the workflow to the ultrasonic measured data of a homogeneous sample. I use two samples, namely Aluminium (AL) and Polymethyl methacrylate (PMMA). I investigate the various effects discussed in previous chapters. Then, I invert the elastic parameters of AL and PMMA using waveform misfit between synthetic and measured data. Since *P*-wave

amplitude is observed in the waveforms acquired using the *S*-wave transducer, I assume that a pure *S*-wave model input is not sufficient to recover the measured waveform accurately. Therefore, I consider a few degrees of inclination for the source input.

I then apply the forward-modelling workflow

In order to investigate the anomaly in the relative moduli changes observed in Vycor glass, desorption of hexane is modelled in Chapter 5. Then, I assume that a homogeneous and isotropic sample is composed of two circular shells such that the inner radius is fully saturated (100 %), while the outer one is 40 % saturated. To investigate the attenuation of the signal, I iteratively increase the radius of the inner shell until it reaches the sample radius.

In Chapter 5 I apply my forward modelling workflow to ultrasonic measurements performed during vapour desorption in a nanoporous glass sample. Desorption occurs when a fully saturated sample is immersed in vapour with gradually decreasing pressure. Ultrasonic measurements performed during desorption show a rather confusing pattern. It was previously suggested that, at a given vapour pressure, the cylindrical sample can be divided into two parts: a 100% saturated inner core (with a radius depending on vapour pressure) and an outer shell with uniform liquid saturation of about 40 %. To explore if this is true, I use my workflow to numerically simulate the ultrasonic experiment described in the literature. Since in this case the source input is unknown, I use Ricker and sinusoidal wavelet as source inputs. The pressure dependency of the phase velocity and of the apparent attenuation estimated from the simulated waveforms match the laboratory measurements very well.

In Chapter 6, I use my inversion workflow to estimate velocity and attenuation from measured waveforms. Specifically, I apply my viscoelastic inversion workflow to ultrasonic waveforms recorded for an air-dry sandstone sample at different relative humidities (RH). The viscoelastic effects are modelled using the so-called Prony formulation with a single relaxation time. To increase the robustness of the algorithm and reduce the number of unknown parameters, I use mode separation to perform *P*-and *S*-waves waveform inversion separately in the time domain. The attenuation results broadly agree with estimates by the centroid frequency shift method, but also show a modest frequency dependency of *Q*, which can be used to gain further insight into the mechanism of ultrasonic attenuation in room-dry rocks.

Chapter 2: Background

The focus of my research is the estimation of the moduli of elasticity and dissipation factors through numerical inversion of waveforms of ultrasonic waves propagating through cylindrical samples of rocks or other elastic and viscoelastic materials. This estimation approach uses the wave motion theory in elastic and viscoelastic media, numerical simulations of these processes, waveform inversion methods and technology of laboratory ultrasonic measurements. These background topics are summarised in this chapter.

2.1. Elasticity

The mechanics of elastic solid bodies are defined using physics principles. The smallest elastic noted elementary volume (EV*)* is assumed to be much larger than the intermolecular distance and regarded as infinitely short (see Figure 2.1).

Figure 2.1: Skeleton of both undeformed (dash line) and deformed (solid line) volume (Brajanovski 2010).

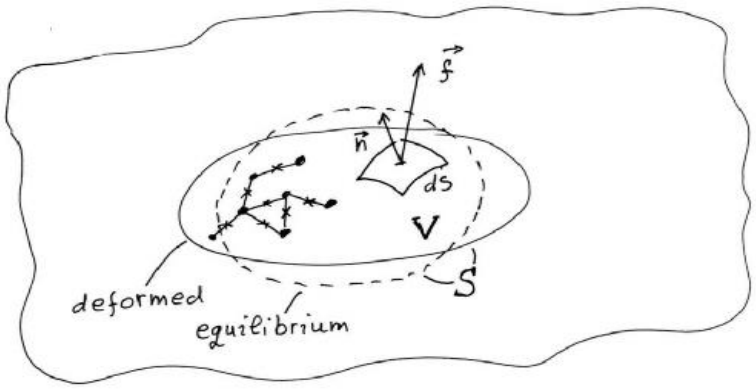

Once compression is applied to EV, volume and shape changes known as strain occur. This process is defined by the vector displacement ***u*** of the elementary volume. For two adjacent points in the medium, their square distance is related to ε_{ik} (Landau and Lifshitz 1970). Mathematically, the strain ε_{ik} using index summation convention is given by:

$$\varepsilon_{ik} = \frac{1}{2}\left(\frac{\partial u_i}{\partial x_k} + \frac{\partial u_k}{\partial x_i} + \frac{\partial u_m}{\partial x_k}\frac{\partial u_m}{\partial x_i}\right) \tag{2.1}$$

where *i, k* and *m* are the indices corresponding to the axes of an orthogonal Cartesian reference system. The quadratic term in the expression for the strain tensor (2.1) is a second order term in displacement and can be neglected in comparison with the other two terms, reducing the strain tensor to

$$\varepsilon_{ik} = \frac{1}{2}\left(\frac{\partial u_i}{\partial x_k} + \frac{\partial u_k}{\partial x_i}\right) \tag{2.2}$$

After deformation the body is no longer in equilibrium, causing a change in position. This results in internal forces acting to restore the initial state. Due to the short range of action of these forces, they cancel out inside *EV*. The forces surrounding EV act on its surface only. Their sum can be written as the divergence of stress σ_{ik}

$$f_i = \frac{\partial}{\partial x_k}\sigma_{ik}. \tag{2.3}$$

The volume integral of f_i can be transformed using Gauss formula,

$$\int_V f_i dV = \int_V \frac{\partial}{\partial x_k}\sigma_{ik} dV = \oint_S \sigma_{ik} n_k dS \tag{2.4}$$

where n_k is a unity vector orthogonal to element surface (*dS*), *dV* is a element volume (Figure 2.1). A positive traction $\sigma_{ik} n_k$ represents the external forces acting on the outer surface of EV, while a negative sign is the action of internal forces on the surface of EV.

Mathematically, the strain energy potential W is useful to describe the effect of deformation using stress and strain ε_{ik} (Aki and Richards, 1980),

$$dW = \sigma_{ik} d\varepsilon_{ik} \tag{2.5}$$

so that σ_{ik} can be written as

$$\sigma_{ik} = \frac{\partial W}{\partial \varepsilon_{ik}}. \tag{2.6}$$

Traditionally, for strain energy potential the Free energy (*F*) is taken in the case of isothermal (slow) processes. That is how basic elastic parameters μ and λ are derived (Landau and Lifshitz 1970). Free energy is given using the Taylor expansion:

$$F = F_0 + \frac{1}{2}\lambda\varepsilon_{ii}^2 + \mu\varepsilon_{ik}^2. \tag{2.7}$$

In Equation 2.7, F_0 is the free energy of undeformed frame, μ and λ are the Lamé coefficients, and can be written as:

$$F = \mu\left(\varepsilon_{ik} - \frac{1}{3}\delta_{ik}\varepsilon_{mm}\right)^2 + \frac{1}{2}K\varepsilon_{mm}^2 \tag{2.8}$$

where the bulk modulus $K = \lambda + (2/3)\mu$ with μ the shear moduli and λ Lamé, and δ_{ik} is the delta function. For solid and elastic bodies, *F* can be generalized by

$$F = \frac{1}{2}c_{ijlk}\varepsilon_{ik}\varepsilon_{jl}, \tag{2.9}$$

which yields the general form of Hooke's law given by:

$$\sigma_{ik} = c_{ijlk}\varepsilon_{jl} \tag{2.10}$$

where c_{ijlk} is called the elastic stiffness tensor. This is a fourth rank tensor, which in the case of an isotropic elastic medium has only real non-zero diagonal elements. In the isotropic and elastic assumption, the stiffness tensor elements contain only μ and either K or λ. They are directly connected to the compressional and shear attributes. Therefore, *P*- and *S*-wave transducers are the best candidates to use in ultrasonic experiments and modelling.

2.2. Viscoelasticity and Prony formulation

Linear elasticity idealization (Hooke's law), described above, is very often not enough to describe real rocks and other porous materials, which exhibit viscous-like as well as elastic characteristics. This combination of behaviour is described by poroelasticity and viscoelasticity.

The poroelastic approach to the rock description is built on Biot's model (Biot 1956). It is constructed on the hypothesis that rocks contain a linear matrix (elastic and porous) with moving viscous fluid in the interconnected pores. Compacted grains are coupled to the elastic grain, and moving fluid within the pore space. A single fluid is assumed to fully saturate the pore space. Other effects such as chemical and thermal are ignored.

Instead of using poroelasticity, sometimes it is better to use viscoelasticity to derive the same results. A viscoelastic material has an elastic (rock frame) and a viscous component (fluid). During loading and unloading, a viscoelastic material loses energy which is converted into heat (Meyers and Chawla 2009, McCrum *et al.* 2003). Unlike elasticity, in a viscoelastic medium, the stress and strain are time-dependent variables. For constant stress, the strain rises with time (creep). However, when the opposite is considered, the stress decreases with time (relaxation). Additionally, the stiffness components depend on the loading rate of change, which causes velocity dispersion. For cyclic loading (harmonic wave), a hysteresis occurs, which leads to energy dissipation. These phenomena cause the wave attenuation (McCrum *et al.* 2003, Meyers and Chawla 2009).

Even a small viscoelastic effect can be significant in some applications: therefore, in such materials, their design or analysis should include their viscoelastic effect. This knowledge is based on measurement. The theory of viscoelasticity describes the time-dependent behaviour of such materials in the convolutional form (Christensen 2003, 2005):

$$\sigma_{ij}(t) = \int_{-\infty}^{t} c_{ijlk}(t-\tau)\frac{d\varepsilon_{kl}(\tau)}{d\tau}d\tau \qquad (2.11)$$

where c_{ikjl} *(t)* is now time-dependent stiffness tensor. The components of this tensor are the relaxation functions of the material. They are basic material properties and the counterparts of the elastic moduli. In fact, if the relaxation function tensor were independent of time, Equation 2.11 could be rewritten as:

$$\boldsymbol{\sigma}(t) = \int_{-\infty}^{t} \boldsymbol{c}(t-\tau)\, \dot{\boldsymbol{\varepsilon}} d\tau \tag{2.12}$$

Or alternatively:

$$\boldsymbol{\varepsilon}(t) = \int_{-\infty}^{t} \boldsymbol{J}(t-\tau)\, \dot{\boldsymbol{\sigma}} d\tau \tag{2.13}$$

where the creep tensor time function is given by $\boldsymbol{J}(t)$. Equation 2.12 and 2.13 show that the creep and relaxation functions have a kind of reciprocal relationship. Assuming the strain to be a harmonic function of time (oscillation) with initial strain value $\boldsymbol{\varepsilon}_0$:

$$\boldsymbol{\varepsilon}(t) = \boldsymbol{\varepsilon}_0 e^{i\omega t} \tag{2.14}$$

where ω is the circular frequency of oscillation, then substituting Equation 2.14 into stress strain relation 2.12 gives

$$\boldsymbol{\sigma}(t) = \boldsymbol{c}^*(\omega)\boldsymbol{\varepsilon}_0 e^{i\omega t}. \tag{2.15}$$

The complex value relaxation function $\boldsymbol{c}^*$ is defined by

$$\boldsymbol{c}^*(\omega) = \boldsymbol{c}'(\omega) + i\boldsymbol{c}''(\omega) \tag{2.16}$$

where $\boldsymbol{c}'$and $\boldsymbol{c}''$ represent the storage and loss modulus of the material (Christensen 2003, 2005).

The attenuation or inverse quality factor is obtained by dividing the relaxation's imaginary and real parts. Experimentally, $\boldsymbol{c}'$and $\boldsymbol{c}''$ can be measured using a modulated amplitude technique known as harmonic motion imaging (HMI) for example (Vappou *et al.* 2009).

In order to model real viscoelastic material, a number of rheological models have been proposed. For example, the Generalized Maxwell model was used to model creep and relaxation behaviour in real rocks (Christensen 2005, Barbero 2013). Here I choose to use the generalized Maxwell model (see Figure 2.2) because it is very general and is the approach implemented in Abaqus. By using a number of relaxation times, the generalised Maxwell model can approximate any viscoelastic rheology, such as Zener, Standard Linear Solid, etc.

Figure 2.2: n-Maxwell elements in parallel representing a Generalized Maxwell model. Each Maxwell element has a dashpot (η_i) connected in series to a spring (E_i). The single spring E_∞ represent the final or long-term modulus (Equilibrium modulus).

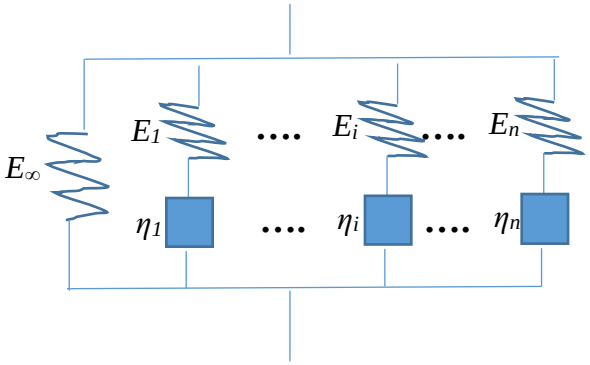

The Generalized Maxwell model with spring and multiple dashpots are shown in Figure 2.2. In this configuration, the total stress is written in the following form:

$$\sigma(t) = \varepsilon_0 E_\infty + \sum_{i=1}^{n} \varepsilon_0 E \exp\left(\frac{-t}{\tau_m}\right) = \varepsilon_0 \left[E_\infty + \sum_{i=1}^{n} E_i \exp\left(\frac{-t}{\tau_i}\right)\right] \quad (2.17)$$

From equation 2.17, the relaxation modulus is written as:

$$E(t) = \frac{\sigma(t)}{\varepsilon_0} = E_\infty + \sum_{i=1}^{n} E_i \exp\left(\frac{-t}{\tau_i}\right) \quad (2.18)$$

Equation 2.18 is the Prony formulation of the time dependent relaxation modulus. E_∞ and $E(t)$ are the equilibrium and instantaneous moduli. The pair (E_i,τ_i) is referred as the Prony pair. Other parameters such as shear/bulk modulus *G*/*K* can be computed by interchanging *E* with *G*/*K* (Vappou *et al.* 2009).

2.3. Ultrasonic experiment

In order to measure the elastic parameters in the laboratory, ultrasonic frequency source and receivers are used. Compressional and shear wave source and receivers are widely used. The source or receivers are piezoelectric material which can measure changes in pressure, strain, or force by converting them to electrical charges. For a simple ultrasonic experiment as shown in Figure 2.3 (*a*), a sample is sandwiched between a source and receiver. The receiver uses the piezoelectric effect to convert the received signal into electrical voltage (waveform) that can be processed. This approach can be enhanced in various ways, such as by using Laser Doppler Interferometer as a receiver (Figure 2.3b) and delay rods (Figure 2.3c).

To model transmitted ultrasonic waveforms, knowledge of the input signal is required. To estimate the elastic parameters, I experiment using *P*- and *S*-waves transducers. I will investigate 3D samples of PMMA and AL as well as other setups.

Figure 2.3: A sample sandwiched between source and receiver transducers (a). (b) A laser source is used instead of the transducer, (c) the sample is sandwiched between two delay samples.

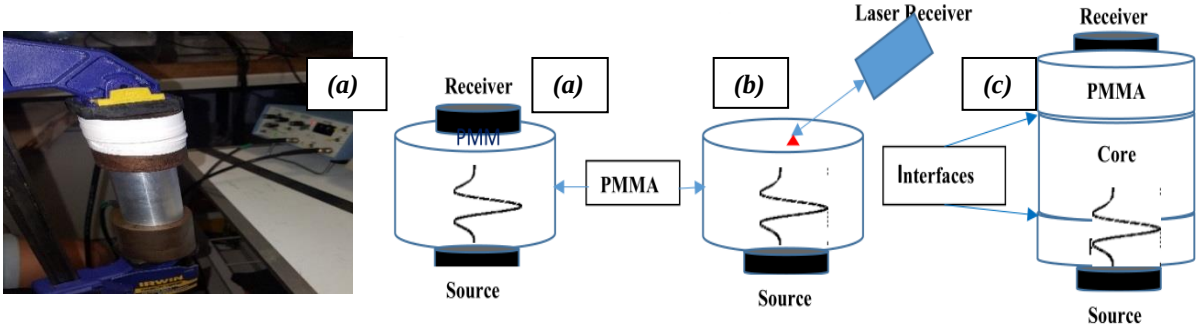

To measure the displacement waveforms, I will follow the task below:

- Measure the input signal by putting the transducers in contact with each other
- Mount the sample between two transducers similar to Figure 2.3(*a)*
- Then sandwich the core sample under investigation between two PMMAs, which are directly in contact with the source and receiver transducers (Figure 2.3(*c)*)
- Finally, run the experiment in Figure 2.3(*a)* for various relative humidity.

2.4. Estimation of properties

In order to estimate the elastic parameters of the measured sample, ultrasonic signals are used. They are affected by inhomogeneities in the sample, wave scattering (neglected in this work because the wavelength is of a higher order than characteristic scale of inhomogeneities) and the intrinsic viscous heat generation causing dispersion and attenuation. In this section, I will discuss ways to estimate velocity and attenuation.

2.4.1. Velocity/Modulus

A standard way to estimate wave velocities is from wave arrival times. Therefore, the arrival time should be measured first. This is done using by either manually picking first break traveltimes or using an automatic cross-correlation algorithm. A significant effort has been put into measuring and estimating wave velocities in seismic bands using force-deformation methods (Batzle *et al.* 2006, Spencer 1981, Liu and Peselnick 1983). Also, a study of velocity

dispersion in sandstone was done by Wei et al., (Wei *et al.* 2017). More generally, wave field effects have been investigated using source/receiver transducers at ultrasonic frequencies for a homogeneous and isotropic cylindrical sample (Yoshimitsu *et al.* 2016, Lee and Waite 2009, Shragge *et al.* 2015, Kolesnikov 2008, Vernik and Nur 1992, Nzikou *et al.* 2018).

Velocity estimation using first-break traveltimes still remains a challenge because of the waveform amplitude threshold (Dellinger and Vernik 1994, Qi *et al.* 2015). Also, a constant threshold was applied to all measured signals using autoregressive AIC-picker methods (Beloborodov 2017, Kruger *et al.* 2013). Amplitude threshold has successfully been used to estimate the elastic parameters of rocks: however, the signal-to-noise ratio could be small enough to cause erroneous estimation of traveltimes. The signal-to-noise ratio is affected by several factors:

- Strong boundary effects (Rasolofosaon and Zinszner 2014, Yoshimitsu *et al.* 2016);
- Dispersion (Mikhaltsevitch *et al.* 2014, Qi *et al.* 2015, Sun *et al.* 2009);
- Unwanted wave packets travelling with the velocity of the main features (Lee and Waite 2009).

To deal with these issues we need to filter out unwanted wave packets (Saether *et al.* 2016), or use other processing techniques such as digital integration stacking or exponential averaging, to enhance features that could shadow *P* or *S*-wave (Liu *et al.* 2018, Norose *et al.* 2015). In this thesis, the measured sample will not be subjected to confining pressure. For a free surface experiment, I will model elastic and viscoelastic parameters using waveforms with a higher signal-to-noise ratio. Then I will compute the wave velocities through the different samples.

2.4.2. Attenuation

Seismic wave amplitude decay is caused by a variety of elastic processes: for example scattering and geometric spreading, in which the wavefield total energy is conserved. The other cause of attenuation is inelastic dissipation (energy dissipating into heat). The latter is of great importance for geophysicists because attenuation is the result of fluid occurrence and motion in the pore within the rock matrix (Müller *et al.* 2010).

There are several methods to estimate the attenuation: for example, the spectral ratio, (McDonal *et al.* 1958), time marching (Gladwin and Stacey 1974), frequency shift (Quan and Harris 1997), amplitude modelling (Jannsen *et al.* 1985), wavelet-broadening (Hatherly 1986), wave-

inversion (Amundsen and Rune 1994) and sweep signals (Matsushima *et al.* 2014). All these methods are not suitable for all studies (Tonn 1991). The most popular is the spectral ratio, which is used for measuring seismic attenuation. However, its application requires extraction of the direct-arrival few cycles to separate unnecessary events from the waveforms (Matsushima *et al.* 2008). Attenuation is affected by the window sizes (Sams and Goldberg 1990) and this dependence is due to spectral leakage (Matsushima *et al.* 2008). Although such a spectral leakage effect can be reduced by increasing the window length, longer windows may extract unwanted events from observed data. Therefore, various window lengths will be investigated to quantify the divergence of the results. This analysis will help prevent arbitrary and biased results from occurring during the modelling of viscoelastic parameters in the sandstone sample.

Wave velocity and attenuation are key parameters for seismic exploration: unfortunately, they are measured in the laboratory mostly in ultrasonic frequency (10^5 Hz -10^6 Hz), a much higher frequency than that of seismic exploration (10^1 Hz*)*. Therefore, when comparing field and laboratory data, the velocity dispersion of saturated rocks should be taken into account (Pimienta *et al.* 2015, Brajanovski 2010). An interesting experiment using seismic frequency was done using force-oscillation apparatus available at the Rock Physics Laboratory at Curtin University (Mikhaltsevitch *et al.* 2014).

Recently, the effect of water sorption experiment was conducted and the elastic moduli and attenuation change was estimated (Yurikov, *et al.* 2018). Hossain (2017) reported the effect of elastic properties changes of Bentheim sandstone using static measurement (Hossain 2017), and Pimenta *et al.* (2014) show the frequency dependence of elastic parameters for limestone and sandstone for different relative humidity (RH) (Pimienta *et al.* 2014). Also, the properties of soft tissues were quantified using ultrasonic-based methods by Vappou *et al.* (Vappou *et al.* 2009) and modelled using a viscoelastic response (Sharma and Kumaraswamy 2018). The amplitude-modulated imaging method they developed estimated the viscoelastic amplitude attenuation, which was validated using the Prony formulation (Vappou *et al.* 2009).

2.4.3. Some issues with existing estimation methods

Both experimental and numerical methods produce unwanted events. These events might be caused by the approach itself, or the way the measurements were conducted.

The main experimental issue is the noise: in other words the amplitude threshold for low signal-to-noise ratio close to first break arrivals. This might result in erroneous first-break picking due to the intrinsic attenuation and scattering (Lee and Waite 2009). The sample's geometry has also a significant effect on measured waveforms. It might affect the waveform amplitude and first-break arrivals especially when the ratio of the sample over transducer diameter is close to 1. This causes the complexity in the velocity estimation (Lee and Waite 2009, Yoshimitsu *et al.* 2016). Also, source displacement input knowledge is very important. The source transducers finite small size increases the complexity even more because of radiation pattern (Alles *et al.* 2010, Daley and Hron 1977).

Some of the experimental challenges could be avoided in numerical modelling either by measuring or cutting the input signal from the recorded signals (Nzikou et. al., 2018). Also, the effect of wave cross-talk and the mixing of domains (time and frequency) increases the non-linearity of the methods (Vappou *et al.* 2009). A limited knowledge of attenuation and dispersion in modelling can possibly introduce erroneous results (Shukui *et al.* 2015, Shin *et al.* 2002).

A further challenge is the estimation of viscoelastic properties. The dynamic analysis of viscoelastic materials is treated numerically using finite element methods by many authors (Vappou *et al.* 2009, Assie *et al.* 2010, Wang *et al.* 2016). This method, used to numerically solve the integral equations, is based on the division of the medium (sample) into small parts (finite elements (FE)). Elements are of different geometrical shapes and sizes.

Also, to estimate the wave attenuation due to saturation and viscosity, I use the same procedures for source input. Then, I build an automated model in Abaqus using an inversion grid-search method (GSM) to match the experimental waveform. Abaqus finite element analysis *(*FEA*)* previously known as ABAQUS is a multiphysics computer-aided engineering software. I use the Abaqus/Explicit module which is a special-purpose FEA for solving explicit integration problems (Smith 2014).

2.5. Inversion

By solving inverse problems i.e. knowing the output data and the input signal, estimates of material properties are obtained. These estimates are not unique but hopefully very probable. As a part of solving an inverse problem, the forward problem is iteratively used.

The first obstacle is the low signal ratio close to the first-break. One way to avoid this is to invert the measured waveforms: i.e., to find the best possible match for the output signals given an input signal. Recently, with the rapid increase in computation power, full-waveform inversion (FWI) is used in mineral resources exploration to assess subsurface properties from seismic data subsurface properties (Tarantola 1986, Zhang and McMechan 2010, Thierry and Lambare 1995). This is a very expensive and challenging approach because of unknown variables for the various earth layers. Luckily, in laboratory experiments, using ultrasonic frequency FWI is much more feasible because only a few parameters are needed. For example, using a single source and receiver transducer, not enough data are available to constraint anisotropy and heterogeneity, therefore, one can assume a homogeneous and isotropic medium. Then, it needs to be inverted only for elastic velocities V_P and V_S, and attenuation factors Q_P and Q_S.

Prior to attempting any inversion, it is best practice to have a sensible agreement between modelled and measured data from known samples. Limited to 2D, Shragge et al. (2015) simulated the elastic velocities observed in laboratory data. Also, they image fractures in cylindrical samples, and their work could possibly be extended in 3D. However, there are a lot of challenges when dealing with 3D modelling, especially when the material is subjected to various constraints. The aim of this work is to offer a few solutions to reduce the above limitations described above. I design and develop an inversion workflow that retrieves the wave propagation through the sample improving its fidelity (waveform misfit) using parameters sweep.

One of the popular inversion approaches is the grid search method (GSM). This method has been widely used in exploration projects for V_P and V_S estimation, and for directions and magnitudes of principal stresses (Shan *et al.* 2007, Liesa and Lisle 2004, Nzikou *et al.* 2018, Ramsay and Lisle 2000, Sato and Yamaji 2006). This method is based on a search for the best elastic parameters such as E within a chosen interval. As shown in Nzikou *et al.* (2018), the cost of computation can be very large. To achieve minimal computational cost for realistic rocks I test the influence of gridding and window sizes. In a homogenous and isotropic sample, this GSM inversion workflow searches for E and ν. However, to invert measured waveforms using an *S*-wave source in a viscoelastic medium more parameters are required. To get the best estimation of these parameters, a mode decomposition in a time domain inversion was used (Wang and Cheng 2017).

The interest in correcting time-dependent mechanical behaviour of real rocks is still growing. One of the ways to correct the time delay seen in viscoelastic materials is to use Prony formulation in the time domain (Vappou *et al.* 2009). My main goal is the estimation of the parameters of viscoelastic media through accurate modelling of the waveforms in Abaqus. In order to fulfil these objectives, I test and validate the results for homogeneous and isotropic samples using waveform convergence and different grid sizes as well as mesh types. Then, I apply the inversion workflow to estimate viscoelastic parameters for a saturated Bentheim sandstone sample (Nzikou *et al.* 2018).

Chapter 3: Modelling of ultrasonic waves in elastic and viscoelastic media using Abaqus software

In order to mimic a realistic ultrasonic experiment, I have built a forward modelling approach using Abaqus finite-element software. In this chapter, I firstly give a brief overview of finite element analysis and Abaqus software. A general modelling workflow is presented for both elastic and viscoelastic behaviour. The viscoelastic model is described using the Prony formulation. Secondly, I model the synthetic elastic waveform, which should correspond to measured waveforms using ultrasonic *P*- and *S*-wave transducers. By using a standard isotropic sample, I examine a few issues that can affect the accuracy of the modelling. These issues are the waveform convergence (the traveltimes of different first arrivals for various grid sizes should coincide) and transducer size effects. Understanding these factors will help in modelling the experimental data acquired using AL and PMMA samples, which is discussed in the next chapter. Finally, the Prony formulation is used in this chapter to model the ultrasonic waveforms in viscoelastic media. The developed viscoelastic workflow will later allow the inversion of viscoelastic parameters such as Q_p and Q_S for a real rock sample.

3.1. Introduction

In a real material, imposed harmonic disturbance of stress (or pressure) causes a wave i.e. the propagation of the oscillations of medium. These waves can be used to reveal the material's physical properties. Depending on the constitutive relations describing the real materials (rocks for instance), there are a few types of wave: elastic, viscoelastic, poroelastic and so on. All of these types of wave's propagation in rocks can be simulated numerically using finite element analysis (FEA).

3.2. Finite Element Analysis (FEA)

Finite Element Method (FEM) is widely used to model and analyse material properties. This method numerically solves the integral equations dividing the medium into distinct finite elements. Elements could be of different geometrical shape and sizes. This method has found numerous application in fields involving continuous media (such as geoscience), where the finite element shape is not obvious. Then a combination of different *FE* shape is used.

The behaviour of a continuous medium (its response to harmonic load in this study) can be described by differential or integral equations, which in most cases cannot be solved analytically. In FEM, the continuum is divided into small (but finite) elements such that each element can be considered homogeneous. Then the integrals involved in the overall equations can be approximated by sums over the elements. This is an alternative to the finite difference method (FDM), where derivatives involved in differential equations are approximated by finite differences (Zienkiewicz *et al.* 2013, Smith 2014). To estimate the material properties the FEM finds its practical applications, for instance in the paper written by Arregui *et al.* (Arregui-Mena *et al.* 2018) for instance.

With current computer power, the discrete problem can easily be solved using a large number of finite elements. FEA includes the use of mesh that divides a complex system into a number of small finite elements. Unlike other numerical methods such as FDM which always use a rectangular grid (Peiró and Sherwin 2005), FEA is a more general approach and can use a variety of meshes depending on the geometry of the problem. Thus, this approach is adopted in this thesis through the use of Abaqus/Explicit.

3.2.1. Abaqus/ Explicit

Abaqus FEA known previously as ABAQUS is a finite element analysis and computer-aided engineering software (Smith 2014). I used the Abaqus/Explicit module, which is a special-purpose FEA for solving explicit integration problems (Smith 2014).

The equation of motion for particle displacement *u*, when mass does not change with time, is given by an equation

$$M\ddot{u} = L_e - L_i \tag{3.1}$$

where the mass is *M*, dots define time derivative, L_e and L_i are the external and internal load vectors. Because the aim of this work is to investigate ultrasonic wave propagation through rocks in the context of linear aproximation only small deformations and stresses are considered.

The equation of motion is numerically integrated using the Forward Euler or Central difference algorithm in Equation (3.2) (Barbero 2007, 2013, Smith 2014).

$$\begin{cases} \dot{u}^{(i+1/2)} = \dot{u}^{(i-1/2)} + \ddot{u}^{(i)} \dfrac{\Delta t^{(i+1)} + \Delta t^{(i)}}{2} \\ u^{i+1} = u^{i} + \Delta t^{(i+1)} \dot{u}^{(i+1/2)} \end{cases} \tag{3.2}$$

where *u* and $\dot{u}$ are the particle displacement and particle velocity, Δt is step time, the $^{(i)}$ and $^{(i\pm1/2)}$ are the increment and mid-increment values. Advantages of using the explicit module are:

- Nodal acceleration $\ddot{u}$ can be computed at any given time such as
$$\ddot{u}|_t = M^{-1}(L_e - L_i)|_t \tag{3.3}$$
- No iterations are required in the equation solvers (3.2 and 3.3) to update the accelerations, velocities and displacements with a change of increments $^{(i)}$.

The explicit module is used here to calculate and display the synthetic ultrasonic waveforms propagated through a cylindrical sample. Moreover, the same procedure is applied to compute the elastic/viscoelastic parameters of the cylindrical and cubical sample in future chapters.

3.3. Modelling workflow

In order to simulate a real experiment that involved a cylindrical sample and a disc-shaped piezoelectric (PZT) transducer, I used the parameters shown in Table 3.1, where *L* and *D* are the sample length and diameter, PZT and SZT are the *P*- and *S*-wave transducers, *E* and *v* are the Young modulus and Poisson ratio, and ρ the sample density.

Table 3.1: Modelling parameters

L ***(mm)***	***D*** ***(mm)***	***PZT*** ***(mm)***	***SZT*** ***(mm)***	***E*** ***(GPa)***	**ρ** ***(Kg/m^3)***	**ν**
50	50	19	19	60	1200	0.3

The user interactively creates the sample geometry and then defines its material properties and vice versa. This is achieved by moving from one Abaqus module to the other. Each module produces output data. A combination of these outputs forms an input file (model itself) that is submitted to the solver (Barbero 2013, Smith 2014).

Figure 3.1: Abaqus model of a cylindrical sample with dimensions 50x50 mm. The orange arrows represent the incident uniform source input. The yellow dash line represents the axis of rotation or the compression direction.

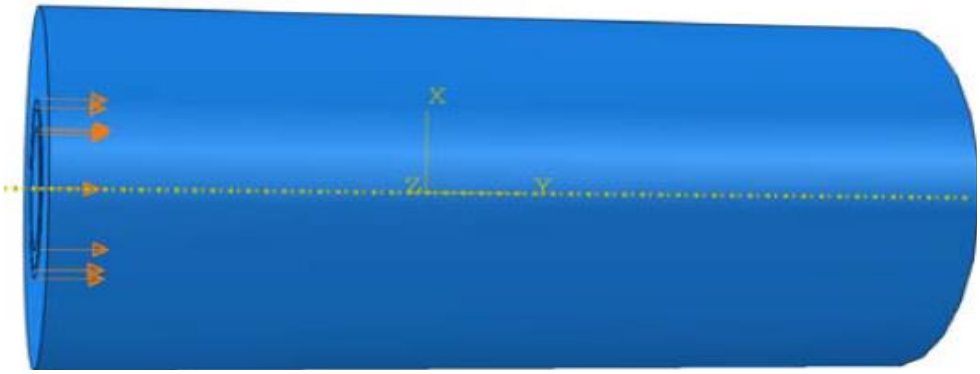

In order to build a model as shown in Figure 3.1 and create ultrasonic synthetic waveforms that can later be compared with ultrasound waveforms from the real sample, the user is required to:

1-Build the geometry of the model

For a 3D cylindrical sample, as shown in Figure 3.1, the length and diameter are inputs to the geometry based tools of the CAD utility module. Then a cylindrical model is built using extrusion, sweeping or revolution techniques.

2- Construct the transducer geometry

In a realistic experiment, the transducers are directly in contact with the sample surface (base of the cylinder). The transducers are represented by a circular disc-shaped area centred by an axis of symmetry (yellow dash line of Figure 3.1). Let U_1, U_2, U_3 be the displacement magnitude along (X, Y, Z) coordinates as shown in Figure 3.1. The *P*-wave source input displacement vector (orange arrow of Figure 3.1) is activated by setting the displacement boundary (*BC*) $U_2=1E\text{-}9m$ and $U_1= U_3=0$. For shear, either $U_1 \neq 0$ while $U_2= U_3=0$ or replace index 1 by 3.

3- Specify the material properties:

In order to model isotropic elastic medium, three input parameters such as *E*, ν and ρ are required. However, in a viscoelastic medium, I assume that General Maxwell (GM) model is sufficient to accurately describe accurately the wave propagation. In Abaqus, the GM model is implemented through the Prony formulation, in which the time-dependent *E(t)* caused by a step function load of the medium is described by an equation:

$$E(\mathrm{t}) = E_0\left(1 - \sum_{\mathrm{i}=1}^{\mathrm{n}} k_{\mathrm{i}}\,(1 - \mathrm{e}^{-{}^{-t}/_{\tau_{\mathrm{i}}}})\right) \tag{3.4}$$

where *E(t)* and E_0 are the instantaneous and equilibrium modulus, with the subscript (*i)* dropped, *k* is the ratio of the equilibrium and the instantaneous modulus and the relaxation time τ i.e. the period needed to drop down from the equilibrium value of *k e*-times.

The Prony formulation for viscoelastic media requires that *k* and τ, be the additional input parameters (Vappou *et al.* 2009, Arregui-Mena *et al.* 2018). In this chapter, I use E_0 as the input parameter for modelling, however, *E(t)* can also be used as input parameters as well. In the future chapters, the two choices (E_0 and *E(t)*) will be cross-correlated in a specific sandstone sample analysis.

After the model is built with all the required parameters, the next step is to specify the mesh and create the job, which is then executed to build synthetic waveforms. To reduce the run time for large analysis, the user does the following:

- Parallel execution through *GPGPU* acceleration job,
- Parallel execution through various machine-*CPU* as used in this study.

3.4. Elastic waveforms modelling

Three major steps are required to generate waveforms in Abaqus/Explicit

1- Geometrical modelling of the setup as shown in Figure 3.1 (section 3.3),
2- Run the job which is processed by the analyzer. This shows the displacement u at any given time. From this step, the model must be specified as a set of finite elements known as mesh (I will discuss this in details in the next section) in order to execute the model.
3- Visualize the waveforms through Abaqus or other software such as Matlab (as in this study).

Given the parameters in Table 1, the elastic velocities can be calculated using equations

$$V_P = \sqrt{\frac{E(1-\nu)}{\rho(1+\nu)(1-2\nu)}} \tag{3.5}$$

$$V_S = \sqrt{\frac{E}{2\rho(1+\nu)}} \tag{3.6}$$

where subscript P and S stands for P- and S-wave. E, ρ and ν are elastic parameters.

For quality control, the modelled waveforms will be cross-correlated with a reference trace to assess P- and S-waves time arrivals. Then these results will be compared with the results of Equations 3(5-6). I use the cross-correlation and velocity estimation from the P- and S-wave peak amplitude and first arrival traveltimes to discuss the convergence of waveforms.

In order to achieve the best waveform modelling, I show the four most popular mesh types and discuss the factors that can result in waveform misfit. However, to reduce misfit error between the measured and model output waveforms, all traces have to be normalized separately with a different normalization coefficient and this process will be referred to as "waveform normalization".

3.4.1. Specifying mesh

Once the geometry and properties are defined, to execute the model the user needs to build a mesh with finite elements. There are two ways to generate a mesh:

1- Manually using mesh editor, or

2- Solid map meshing, where the user constructs volumes (as shown in Figure 3.2) areas and points that can automatically be meshed to get the nodal distribution.

In Figure 3.2(*a-d*) the four popular meshes are shown. They are the Hexagonal–dominated (denoted as HEXD), the Tetrahedral (or TET), the Wedge and the Hexagonal (referred to HEX). Many of these mesh types connect nodes to form triangles and wedges using triangulation methods such as the Delaunay triangulation and the Voronoi diagram, and they are easily accessible in Abaqus (Smith 2014, Brostow and Dussault 1978, Cavendish *et al.* 1985, Boubez *et al.* 1986, Kam 2010).

Figure 3.2: Various mesh grid types in an Abaqus 3D model of a 50x50 mm sample. These meshes are not all available when using the axisymmetric modelling module for example.

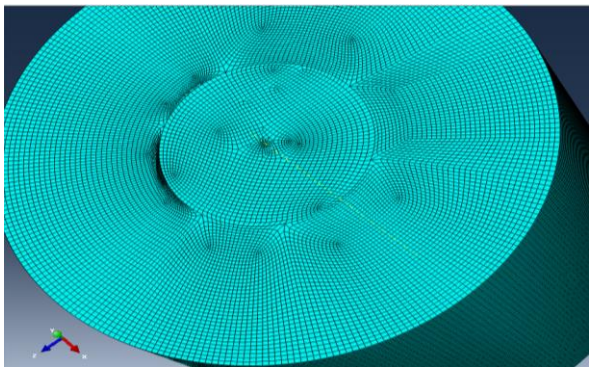

a: Hex-dominated (1396713 Elements)

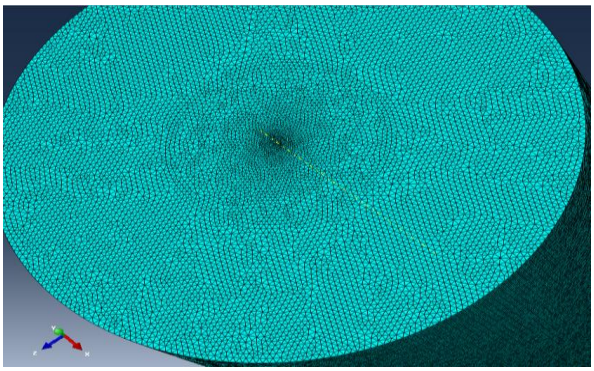

b: Tethadrehal (Tet) (2845145 Elements)

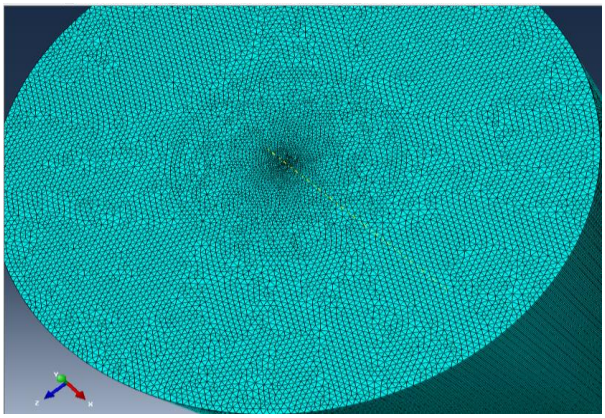

c: Wedge (2141190 Elements)

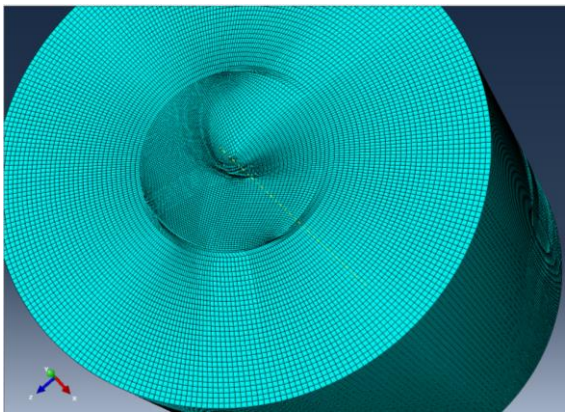

d: Hex (1725384 Elements)

3.4.2. Waveforms convergence

As mentioned above the waveform convergence depends on the size of the grid Δx. The numerical stability of FEA ensures convergence when the Courant-Friedrichs-Levy (*CFL*) satisfies the following equation:

$$C \equiv \frac{|\dot{u}|\Delta t}{\Delta x} \leq C_{max} \tag{3.7}$$

where *C* define the Courant number and Δx is the span interval. Commonly, C_{max} = 1 however, larger values of C_{max} can be accepted in implicit integration, because the matrix solvers are less sensitive to numerical instability (Kam 2010, Trefethen 1996, Peterseim and Schedensack 2007, Hujeirat 2003). In Abaqus, the *CFL* criterion is automatically tested for any given grid size provided that the user does not input the step time Δt. This greatly reduces the computational time (for fixed step time Δt the analysis is longer).

Let have a look at the following example. For a given Vp=8204 m/s and Vs=4385 m/s, at 1.0 MHz frequency assuming Δt=10 μs, the stability of the waveform requires that:

- For *P*-wave convergence $\Delta x \geq 0.082m$,
- For *S*-wave convergence $\Delta x \geq 0.041m$.

After all input data are defined, model execution of the model gives waveforms as output. The waveforms convergence is shown in Figure 3.3(*a-b*), for a homogeneous and isotropic sample using a *P*-wave source (Figure 3.3*a*) and *S*-wave source (Figure 3.3*b*) with Ricker wavelet amplitude (Wang 2015). The magenta, red, and blue colours represent the grid sizes 0.09, 0.01, 0.008, and 0.0045 mm, one-to-one. In Figure 3.3(*a)* synthetic waveforms converge for grid sizes less or equal to 0.01 mm. However, each grid produces a slightly different amplitude of both *P*- and *S*-wave arrivals. This difference might be due to the nodal distribution difference (Note that the finer the grid, the higher the number of nodes). The *P*-waves converge better.

Figure 3.3: Panels (a) to (b) show the displacement waveforms using a P-wave (top) and S-wave (bottom) for four different grid sizes 0.09, 0.01, 0.008, 0.0045 mm. The model uses a 3D 50x50 mm sample and the Ricker wavelet source amplitude with frequency of 1MHz.

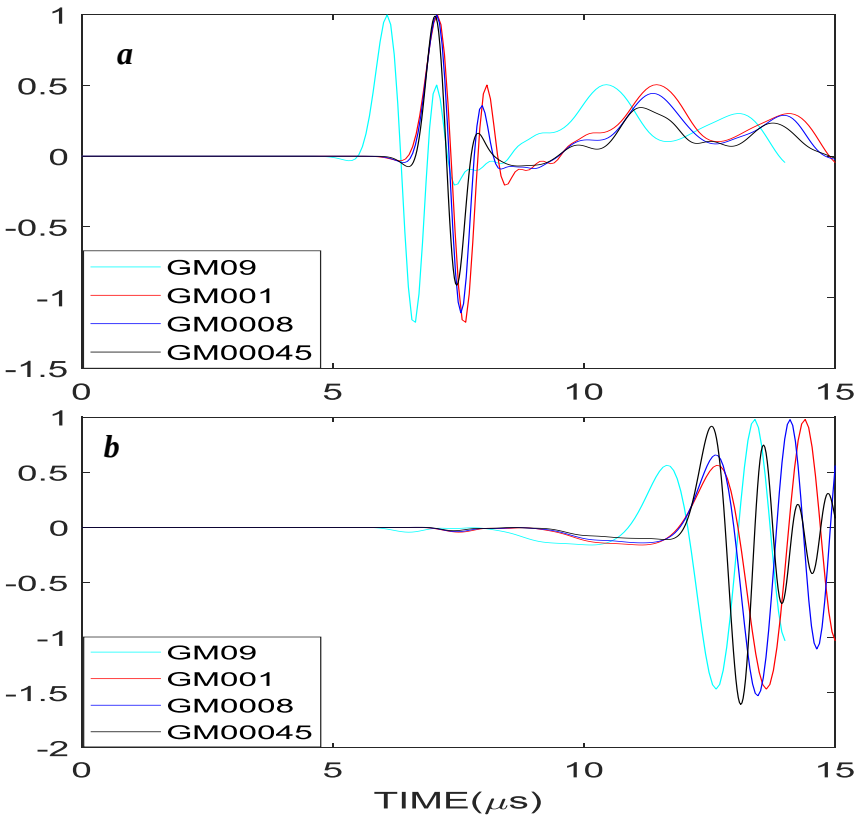

3.4.3. Wave velocity estimation

In order to estimate wave velocities, I had to firstly estimate arrival times using cross-correlation and peak amplitude traveltimes for waveforms roughly satisfying convergence criterion and secondly compute the velocity. Waveforms from the very coarse grid (0.9 mm) are not considered in the following work. Since the model deals with an isotropic elastic medium, the phase velocity computed from the moduli is the same as the group velocity (waveform). Therefore, for quality control, I estimated the group velocities. For future reference, cross-correlation estimated velocities are labelled as V_P and V_S, while peak amplitude traveltime estimated velocities as V_{PP} and V_{SS}. Figure 3.4 compares wave velocities obtained with the above two methods against the theoretical values.

From Figure 3.4 it can be seen that *P*-wave waveforms (red colour) converge faster than *S*-wave (blue). Also, by increasing the number of nodes from coarse (0.01 mm) to finer (0.0045 mm) grids, the *S*-waves tend to converge. The velocities estimated from the cross-correlation method are faster than the peak amplitude estimated velocities (Figure 3.4). The peak amplitude

estimated velocities are used for calibration purpose as a lower velocity bound of the sample's true velocity.

Figure 3.4: P- and S-wave velocity convergence using a global mesh grid with the size of 0.01, 0.008 and 0.0045 mm. Red and blue colours represent P-and S-wave velocities respectively. The solid, dash and star lines are the calculated using density, Young modulus, and Poisson ratio, the cross-correlated or first break picking and the peak amplitude velocities.

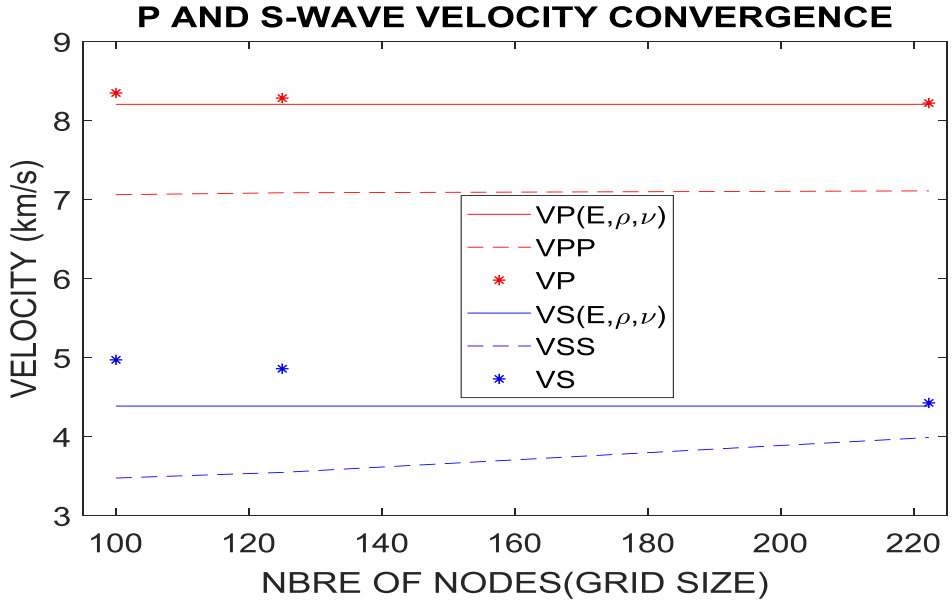

Note that error in wave velocity estimation depends on grid size. Quantitatively, the *P*-wave velocity error is larger than that of *S*-wave. The velocity error in *Vp* decreases from 1.74 % to 0.1 % for a grid departure from a coarse 0.01 mm to the finer grid of *0.0045 mm*, while the error in *Vs* falls from 13 % to 0.9 %. This is possibly due to the irregular convergence of the waveforms.

3.4.4. Computational cost and mesh type effect on the waveform

Assuming that the waveform convergence criterion is met, a particular mesh can still have a different effect on the waveform amplitude. In this section, I investigate the mesh effects modelling the waveforms using HEX, TET and HEXD.

For example, as shown in Figure 3.2, using a grid size of *0.45 mm*, a HEXD mesh has 1,396,713 elements, far fewer than the number of elements of a TET mesh (2,845,145 elements). Therefore, a HEXD mesh has a shorter computational time. However, if the sample has curvatures of complex shape, other meshing techniques can be implemented (Barbero 2013, Smith 2014, Ho-Le 1988).

In figure 3.5, I show the modelled waveforms using HEX (red), HEXD (blue) and TET (black) meshes. Regardless of the time cost for each mesh type, they all reproduce roughly the same first break. It could be seen that in the time interval 6 to 10 µs, HEX and HEXD meshes correlate well. In changing one mesh type to the other a slight amplitude difference is observed.

Figure 3.5: Model waveforms of a 50x50 mm sample using mesh grid size 0.05x0.01 mm and 1 MHz P-wave source. Three type of meshes are compared: HEX, HEXD and TET meshes represented in red, blue and black respectively.

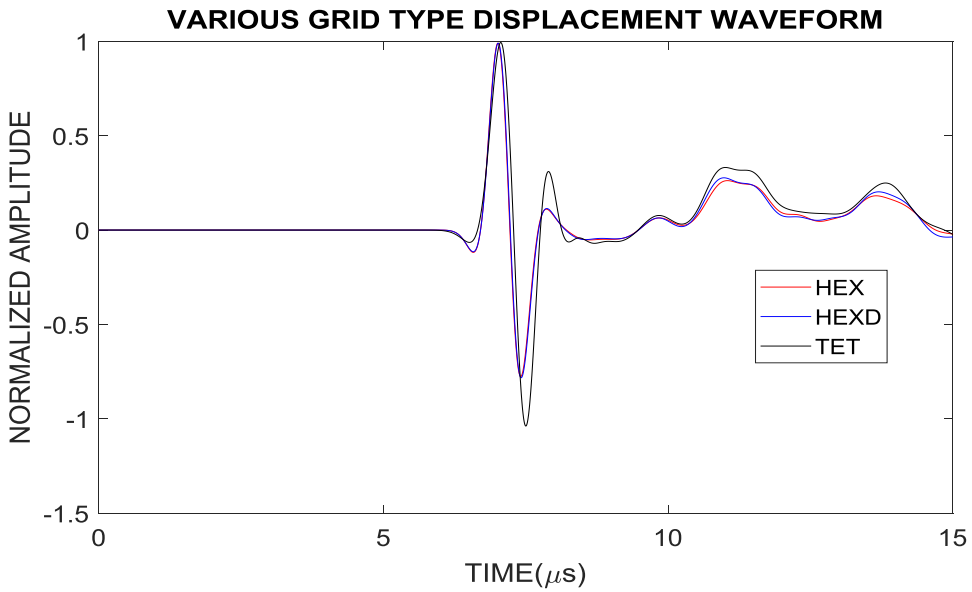

3.4.5. Normalization and transducer size effect

In this section, the waveform normalization is examined first, then secondly I compute *Vp* and V_S using various transducer sizes and their effect on the waveform amplitude. The main problem is that the number of synthetic traces is high but the recorded trace in a real experiment will be just one. The question is what to do with all these synthetic traces in order to represent just one real trace? It is possible to do two procedures: normalization and averaging. The order of these two procedures is very important. This fact could be seen in the following example:

Let the diameter of the receiver-sample contact be of 19 mm. For finite mesh HEX with a grid size of 0.05x0.01 mm, 700 synthetic traces are generated. For comparison with a single recorded measured trace, the 700 synthetic traces need to be processed. The process of waveform normalization is then performed in two ways:

1- I normalize individual trace before averaging (NBA). Each trace out of 700 waveforms is normalized to 1. Then, the newly normalized set is averaged as shown in red in Figure 3.6;

2- I compute the average of the 700 traces resulting in one trace, then normalize that trace to 1. This will be referred to as ABN (see Figure 3.6, blue curve).

Figure 3.6: Model waveforms of a 50x50 mm sample using HEX mesh grid size 0.05x0.01 mm and 1 MHz P-wave source. Red and blue colours represent the results estimated using NBA and ABN methods. NBA refers to the normalization before averaging, while ABN is the average before normalization.

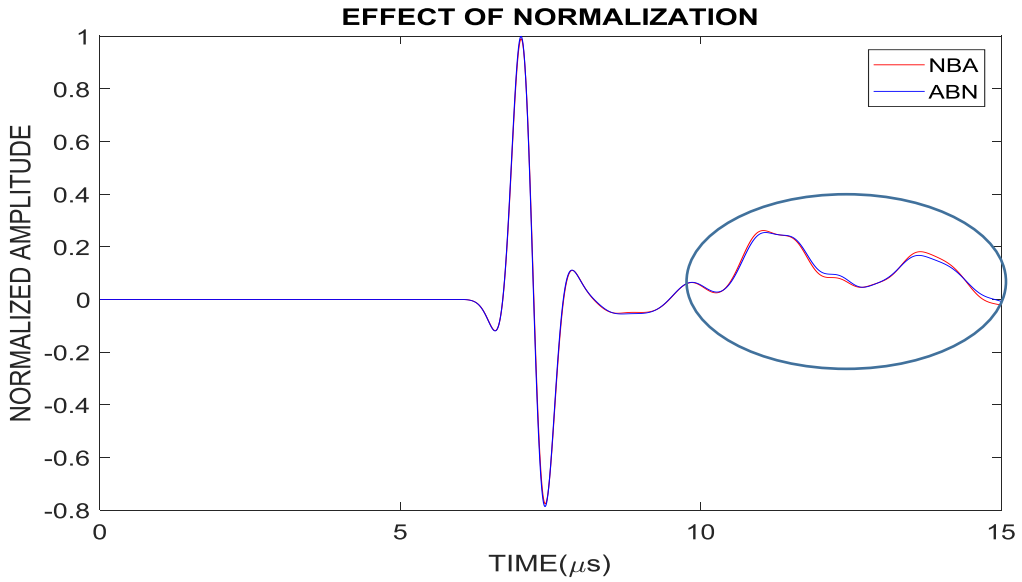

The *P*-wave first break travel time and amplitude agree for the various normalization methods. However, a slight difference is observed for later events which could be caused by reflected wave arrivals from the boundary of the sample (circled area in Figure 3.6). This difference could be more significant when the ratio of the sample diameter to the receiver diameter is higher.

Figure 3.7: Model waveforms using 50x50 mm sample using mesh grid size 0.05x0.01 mm and ultrasonic P-wave source with diameters 20 mm (HEX mesh), 15mm(HEX mesh) and 8mm (TET mesh), respectively.

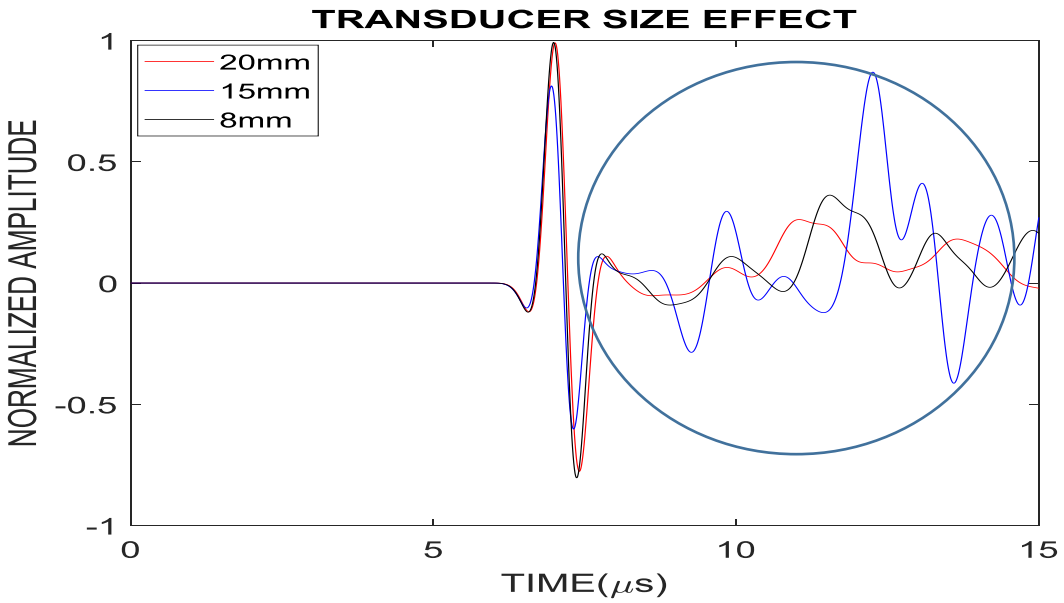

In addition to the previous issue, the size of the receiver sample contact also affects the waveform amplitude. The effect of transducer size on the waveform amplitude is investigated using three transducers with diameters 20 mm, 15 mm and 8 mm. Figure 3.7 shows the results for 1.0 MHz source frequency. The source and receiver are the same. It can be seen that the *P*-wave waveform amplitude increases linearly with the size of the transducer. The bigger the diameter, the higher the *P*-wave amplitude, because the larger transducer transfers more energy into the sample. Since the transducer size is fixed in this study, it will not be discussed in future chapters.

3.4.6. S-wave waveforms and velocity analysis

Laboratory studies have shown that *S*-wave transducers, apart from strong *S*-waves, produce sufficiently strong *P*-waves as well. Therefore, they give a way of estimating both *P*- and *S*-waves velocities and attenuation from one measurement. In the measurement using the *S*-wave source, *P*-wave arrival is weaker but can still be identified as arriving much earlier than the *S*-wave (Yurikov *et al.* 2018; Lebedev *et al.* 2013). In this section, the *S*-wave transducer is used to model displacement waveform in the sample of Table 1. The various effects observed using a *P*-wave source in the previous section are valid for *S*-wave as well. The focus of this section is to build the displacement waveforms using *S*-wave transducers and estimate the velocity of

P- and *S*-waves from their arrival times. Figure 3.8 shows the transmitted ultrasonic waveform using a *S*-wave source. Both *P*-and *S*-wave first breaks arrivals are visually identifiable.

In Figure 3.9, the wave velocities are compared for both *P* and *S*-wave sources. It shows that the velocity difference between the modelled and calculated wave velocities using equations 4-5 is about 0.6 %, 3 % and 1.2 % for V_P (*P*-wave source), V_P (*S*-wave source), and *Vs* (*S*-wave source), respectively. The slight delay of about 2.4 % in V_P between *P*- and *S*-wave sources could be due to the direct compression of the sample using the *P*-wave source.

Figure 3.8: Model displacement waveforms using the 50x50 mm sample, for a grid size RMxGM=0.05x0.01 mm and S-wave source with Ricker wavelet amplitude. The source input diameter is 19 mm and the source frequency is 1MHz.

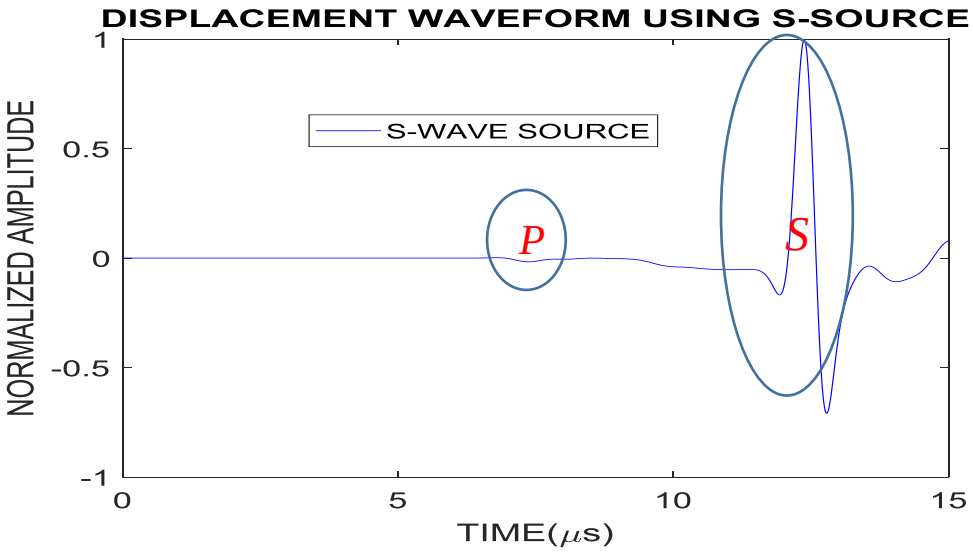

Figure 3.9: Elastic velocities of 50x50 mm sample using P-wave source (solid black) and S-wave source (solid blue and dash blue) compared with the theoretical values of P (solid red) and S (red dash line).

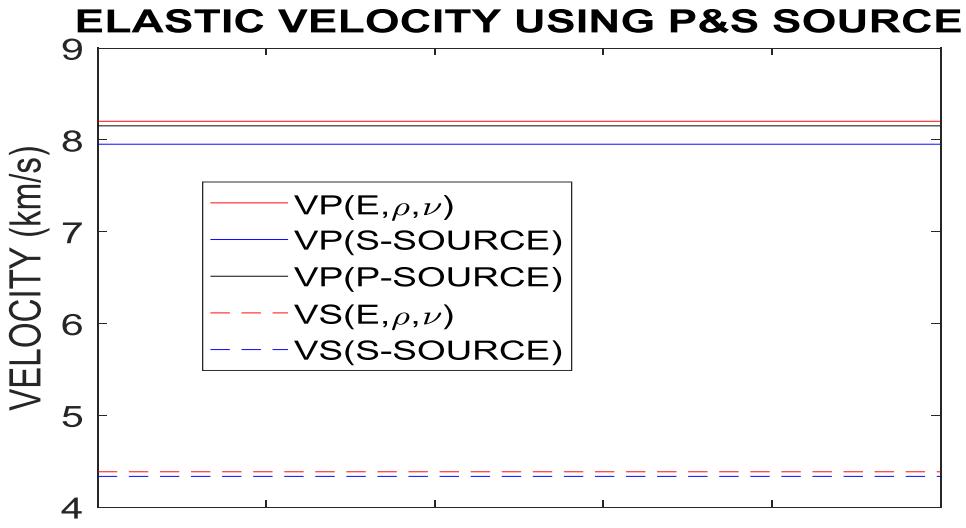

3.5. Viscoelastic waveform simulation

After the modelling of waveforms in an elastic medium, the aim of this section is to simulate waveforms for a viscoelastic medium. The amplitudes of the waveforms are additionally dependent on parameters called Prony pairs, mathematically describing the effect of internal viscous forces in the medium.

The following test is useful for the future chapter to guide our inversion decision of the Prony pair *k* and *g*. I use a *P*-wave source/receiver with 1.0MHz frequency in direct contact with a 50x50 mm cylindrical sample. The modelling parameters are given for the elastic case as E=69 GPa, ν=0.35 and ρ=1200 kg/m^3. I apply the Prony formulation in Equation (3.4) for fixed *k* and τ while the dimensionless shear modulus *g* varies.

3.5.1. *V*iscoelastic modelling using a *P*-wave transducer

In order to model the viscoelastic ultrasonic waveform, I defined the viscoelastic parameters as follows: *k*=0.5, τ=1e-9 (s) and *g* vary from 0.1 *to* 0.5 with the increment of *0.1*. The waveforms result in elastic (red) and viscoelastic (other colours) are shown in Figure 3.10. It could be seen that traces are similar for any given value of *g*. However, there is a slight amplitude difference for *P*-waves.

In order to make future inversion possible, it is necessary to find the best range for *k* and *g*. In Figure 3.11 the velocity linearly decreases with increasing *g*, while the amplitude rapidly decreases during the transition of the medium from elastic to viscoelastic. Quantitatively, the transition from elastic to viscoelastic medium led to a 20 % of *P*-wave amplitude drop while in the viscoelastic medium, for the variation of *g* from 0.1 *to* 0.5, only a 4 % change of the *P*-wave amplitude is observed.

Figure 3.10: Viscoelastic model waveforms compared with elastic model (red) transmitted through a 50x50 mm sample using a 19mm P-wave transducer with frequency 1.0 MHz. (a) shows the full wave train for various value of g, and (b), the P-wave amplitude is zoomed for visual comparison between various value of g.

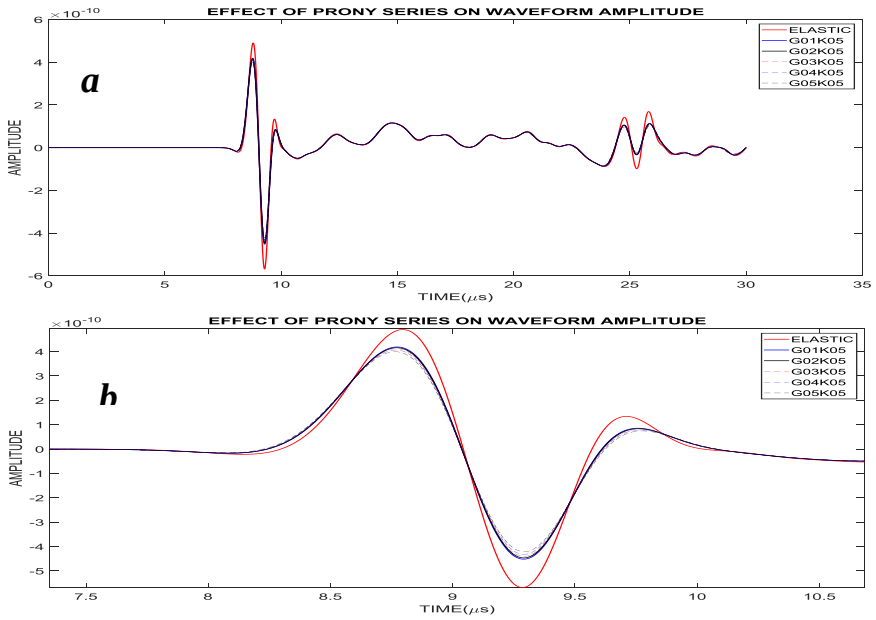

Figure 3. 11: Velocity (top) and amplitude (bottom) estimated from the waveforms shown in Figure 3.10 for various values of g.

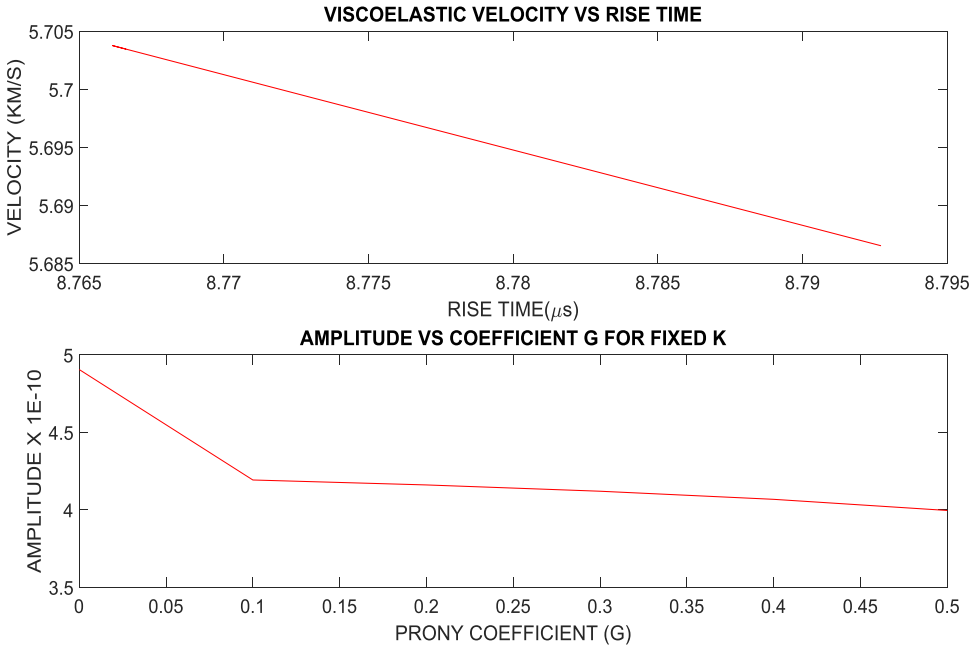

3.6. Discussion

Considering a finite-size disc-shaped transducer, it is clear that the convergence of the waveforms relies on the mesh grid size. The amplitude of *P*- and *S*-waves can be accurately modelled.

A robust waveform model might require a large computational cost. The amplitudes of *P*- and S-waves depend on the mesh type and are similar for various transducer sizes (Fig. 3.6). However, the events following *P*-wave arrivals are more prominent for a source with a smaller diameter (circled area in Fig. 3.7). This direct wave has the same amplitude using NBA and ABN methods. Individual traces need to be normalized then averaged to avoid a misfit between later events (Fig. 3.6).

A shear wave transducer is advantageous and can be used to fully estimate the elastic parameters. The effects of sample 3D geometry have been simulated and show that the transmitted waveforms from the cylindrical sample in the laboratory using either *P* or *S*-wave sources can be modelled using Abaqus. The transmitted waves can be distorted by the converted and reflected waves, especially for later events. However, this work focuses on robust *P*- and *S*-waves modelling therefore, effects of later events will be ignored in the following chapters.

Viscoelastic waveforms can be modelled using Prony formulation. The velocity and amplitude changes observed using a *P*-wave source could provide an insight into the best choice of *k* and *g*. This will reduce the computational cost. Also, using a shear wave source for simulation of a real experiment will help to solve the complex behaviour of both *P*- and *S*-waves in a real sample.

Chapter 4: Experimental results using Aluminium and PMMA samples

In order to validate the methods described in chapter 3, I conducted an experiment using two cylindrical samples of PMMA and AL. The aim is to apply the forward modelling workflow to experimental data. After validation of the forward model, I develop a robust inversion method to estimate elastic moduli of the above samples. Both *P*-and *S*-wave transducers are used as source and receivers in the ultrasonic frequency range. The robustness of the full-wave inversion for a homogeneous and isotropic medium is shown to be sufficient to estimate the elastic parameters of the above-mentioned samples.

4.1. Introduction

I consider statistically a homogeneous and isotropic sample. Materials could be a multiphase aggregate with randomly distributed phases, porous solid, or a combination of both. My goal is to estimate the elastic properties of such real samples using the numerically developed forward model in chapter 3 for inversion purposes.

I used forward modelling of samples of known parameters. I have chosen PMMA and AL because they are widely used for equipment tests and calibration (Meza *et al.* 2007, Siva *et al.* 2005). Then, I compared the inverted elastic parameters with those from forward models. This serves as a validation for my inversion algorithm, which will later be applied on real rocks that could make geophysical exploration projects more complex.

4.2. Experimental setup

The experimental goal is to record the waveforms transmitted through the samples which were emitted by either *P*- or *S*-wave finite-size transducers. Figures 4.1 illustrates the setup that was used to acquire data for the sample of AL (and PMMA).

The ultrasonic *P*- and *S*-wave transducers used in this experiment emit a wave packet of 1 MHz central frequency and their diameters are reported in Table 4.1. In one experiment shown in Figure 4.1(*b*) the aim was to record the surface motion of the transducer and to use it as the source input for the numerical modelling of the data acquired in the other experiment shown in Figure 4.1(a). The transmitted signal in AL was acquired by putting both source and receiver transducers in direct contact with the flat side of the sample under a voltage of 100 V. In order to keep the stability of the sample source and sample receiver contact, the entire system was clamped (see in Fig 4.1(*a*)).

In the table below the measured properties of the samples are shown, where *L* and *D* are the lengths and the diameter of the sample, and PZT and SZT are the diameters of *P*- and *S*-wave sources.

Table 4.1: Measured properties of samples

Sample	***L (mm)***	***D (mm)***	***PZT(mm)***	***SZT(mm)***	**ρ*(Kg/m^3)***
AL	77.48	38.40	19.05	15.86	2697.8
PMMA	49.15	38.17	19.05	15.86	1144.0

Figure 4.1: A photo of the cylindrical AL sample in contact with S-wave transducers (a). S-wave source and receiver in contact (b).

In order to model the measured waveforms from the above experiment, the samples modelling parameters such as *E, v* and density (ρ) are reported in Table 4.2.

Table 4.2: Material modelling properties

Sample	***E (GPa)***	***v***	***ρ (Kg/m^3)***
AL	69.00	0.350	2700
PMMA	6.065	0.316	1200

4.3. Modelling of waveforms using *P*-wave source

Ultrasonic wave propagation is modelled using Abaqus finite element analysis software through its Explicit module, reported as Abaqus/Explicit. The explicit modelling of wave propagation is based on the central difference algorithm and only a few parameters such as *E*, *v* and ρ *(*as shown in Table 4.1) are required to deal with homogeneous and isotropic samples such as AL and PMMA.

In this section, I compare the waveforms modelled using the *P*-wave source and receiver transducers. I use various source inputs such as the measured PZT shown in Fig4.1(*b)*, measured Laser Doppler interferometry (LDI) (Nourifard and Lebedev 2018) and a theoretical source input with Ricker wavelet amplitude (Wang 2015). For a robust match of the waveforms, I show the results of the normalization methods discussed in chapter 3 and finally display the wave field images for various step times.

4.3.1. Source comparison

The waveforms are modelled using *PZT*, *LDI* and Ricker wavelet source inputs and shown in Figure 4.2 (a-c). The first break traveltimes from all the sources tend to coincide well. The waveforms using *PZT* correlate better than any other source inputs. A poor correlation is observed using *LDI* input.

Figure 4.2: P-wave waveforms transmitted in AL using 3 different sources such as a) - Ricker wavelet, b) PZT, and c) LDI sources. The results are obtained using 1MHz source frequency for the AL sample reported in Table 4.2.

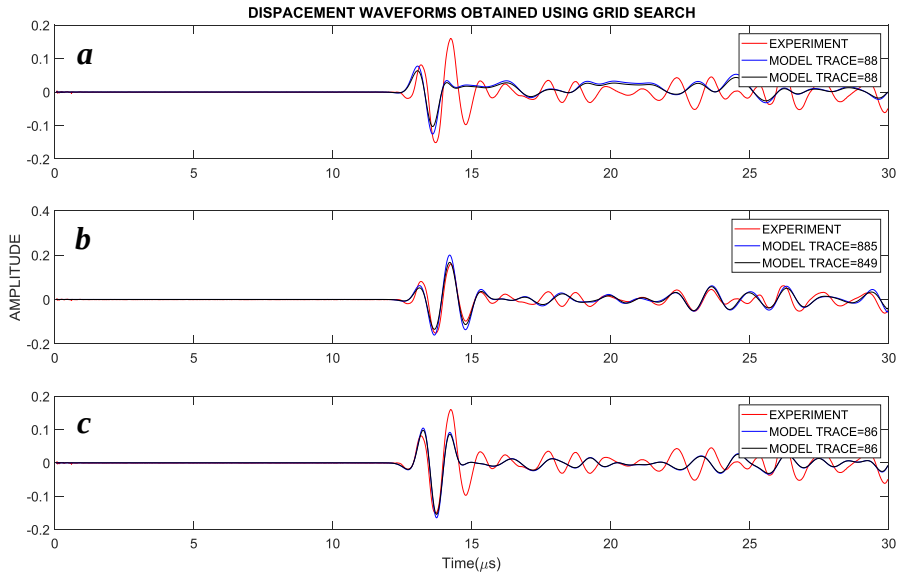

Table 4.3: Comparison of P-wave traveltimes and velocities using cross-correlation with measured data for various sources.

Methods	***First break (μs)***	***P-velocity (m/s)***	***Goodness of fit %***	***Average difference %***
Experiment	12.42	6200	100	0.00
LDI	12.34	6240	0.3	50.29
PZT	12.42	6200	40	8.72
Ricker	12.42	6200	20	20.85

The *P*-wave velocity is estimated as the ratio of *L* and the cross-correlated traveltimes reported in Table 4.3. The goodness of fit quantifies the discrepancy between experimental and synthetic waveforms and the average difference from various source inputs are computed as the difference between the mean value of the experimental and model data. The velocity error between Ricker and other sources is about 0.6 % (or travel time difference of about 0.08 μs), while the velocity remains the same for PZT and LDI.

The best match is achieved for PZT (40 %). The same source input results in the lowest average error (9 %), which confirms the best waveform match shown in Figure 4.2. These tests show that the robustness of the waveform relies a priori on the knowledge of the source input.

4.3.2. Effect of normalization methods

In chapter 3 I have introduced two normalization methods ABN and NBA. Now, I will test and validate these methods using the *P*-wave source in a range of frequency between 0.1 and 2 *MHz.* Figure 4.3 shows the transmitted experimental (red) and the modelled (blue) waveforms in the AL sample using various frequencies. The left-hand side (LHS) of Figure 4.3 figure is obtained using the NBA, while on the RHS, ABN was used to process the waveforms.

Figure 4.3: Waveforms transmitted in AL using two kinds of normalization methods. The left image follows step 1 and the right image step 2. From bottom to top, the source frequencies are 0.1, 0.25, 0.5, 1 and 2 MHz. The red is the experiment compared with the model data in blue.

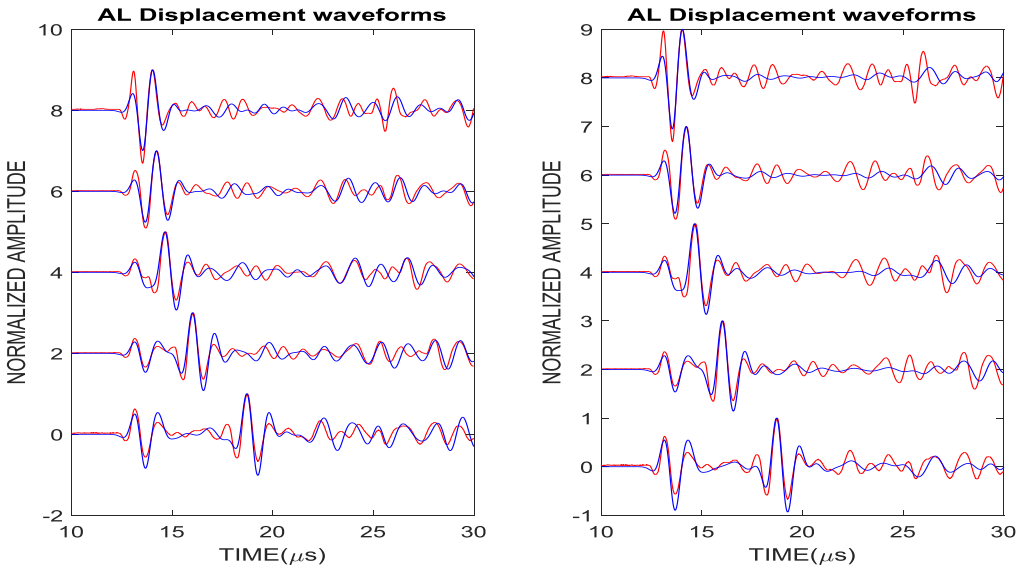

Quantitatively, for any trace in Figure 4.3, the goodness of fit decreases from 85 % (right) to 40 % (left) for all the frequency ranges. The average difference approaches 1 % for the NBA and about 25 % for ABN. Most of the later events (reflections from the boundary for instance) match the experimental data very well using the NBA. However, in the other method, they only agree well with only *P*-wave arrivals. I apply the same workflow to reproduce the waveforms acquired from the PMMA sample. The results are shown in Figure 4.4. Both normalization methods match the measured data very well. Their cross-correlation coefficient is similar and is about 1 % for the different frequency range. This smaller error is due to almost not observable later events in the waveform caused by the larger sample diameter.

To robustly reproduce the waveforms in any sample and to avoid later events misfit, the average waveform should be computed using an NBA scheme.

Figure 4.4: Displacement waveforms of PMMA using NBA and ABN defined in chapter 3. From bottom to top, the P-wave source frequency is 0.5, 1 and 2 MHz, respectively. The experimental data (red) compare well with the model data (blue).

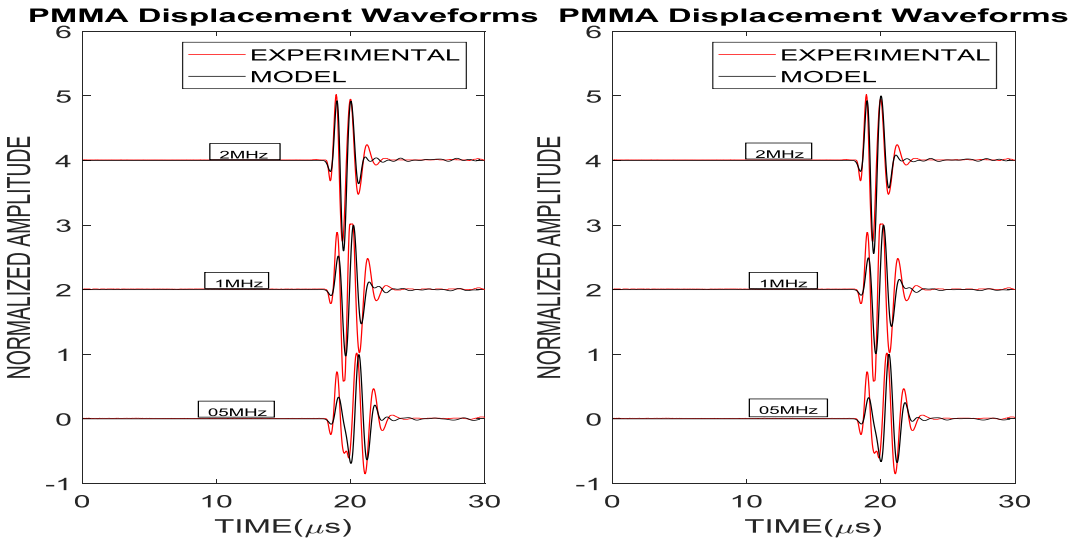

4.3.3. *P*-wave wavefield snapshot

In this section, I present the snapshot of the wave motion in PMMA and AL for visualization purposes. I also visually compare the P-wave traveltimes with the earlier cross-correlated results. Figure 4.5 and Figure 4.6 show the wavefields in the AL and PMMA samples.

The transmitted P-wave energy near 12.42 µs (Figure 4.5b) agrees well with the measured traveltime reported in Table 4.3. As time elapses, more wave modes, like reflected *P* and converted *PS* are back-propagated. Unless appropriate processing techniques are used to remove noises and unwanted waves, *S*-wave traveltimes using *P*-wave transducers can be erroneously estimated. In this study, the PMMA sample has a larger diameter than AL and its waveforms do not show a significant effect of the boundary reflection (Figure 4.6). There is almost zero disturbance visible after the P-wave arrival confirming the low appearance of later events in PMMA in Figure 4.4 as well.

Figure 4.5: Wavefield images for AL sample at a)-t=7.24μs and b)-t=12.42μs.

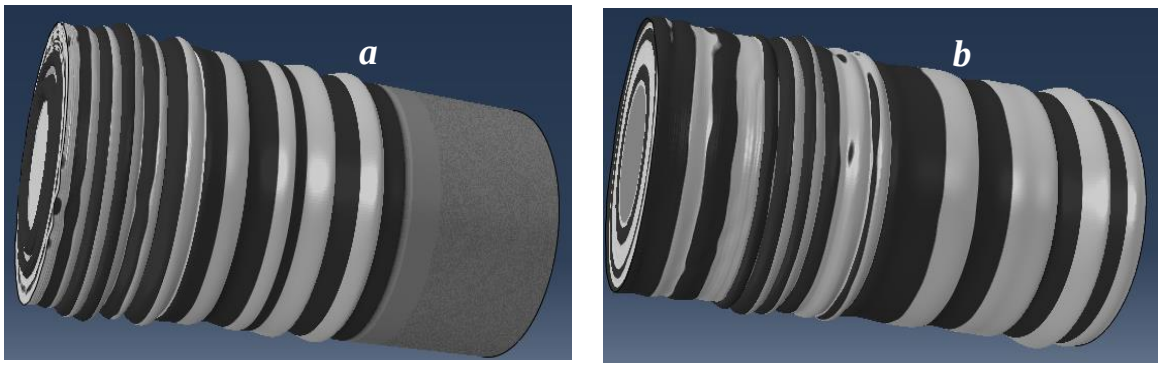

Figure 4.6: Wavefield images for PMMA sample at a)-t=7.9μs and b)-t=18.72μs.

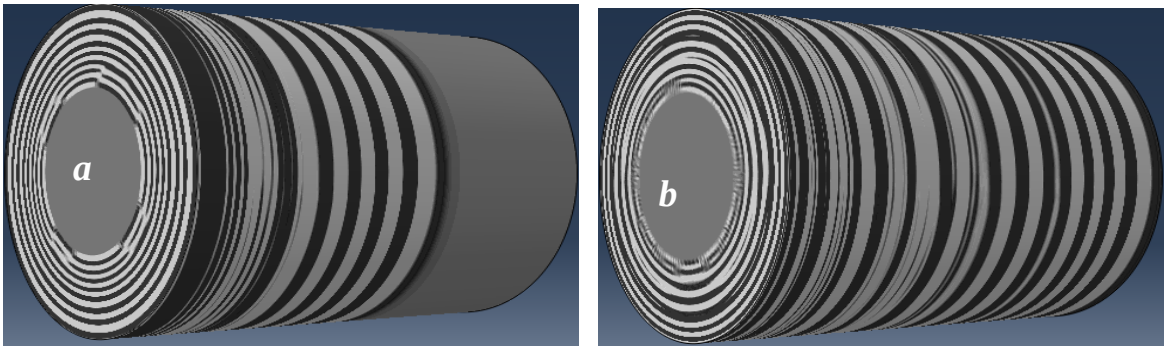

4.4. Modelling of waveforms using S-wave source

In this section, the synthetic waveforms in the PMMA and AL samples are modelled using the *S*-wave transducer source. In order to best model the presence of *P*- and *S*-waves in the measurement, I assume that the shear wave vibration reaches the sample surface with a very slow inclination angle and also that the *S*-wave transducer induces a *P*-wave mode of less than 1 % of *S*-wave magnitude (Olympus 2007). I used PMMA and AL samples to test and validate the assumptions. For future reference, the first assumption will be referred to as the inclination approach.

In the inclination approach, the user is required to input the degree of inclination of the shear displacement vector (the angle between the radial axis and shear displacement vector). The initial inclination angle can be estimated from Equation 4.1

$$\theta = \arctan(\text{measured P-wave amplitude} / \text{measured S-wave amplitude}) \quad (4.1).$$

S-wave amplitude much bigger than *P*-wave amplitude when using S-wave transducer, so the initial value of θ_{input} is small enough for the modelling purpose. Note that in an ideal case (pure

linear elastic) there will be no *P*-wave recorded at all. Due to effects caused by the complex character of intermolecular forces in the real material, there will always be both types of waves in the waveform. Their relative amplitude depends on the shape of the sample and the size of the sample-transducer contact. However, I will not go beyond linear elastic approximation in this work.

Experimentally, I estimated from equation 4.1 an initial value of θ from both the PMMA and AL waveforms to be $\theta \approx 2^{\circ}$ (labelled as θ_{output}). Assuming that the input angle is less than 1 %, I use θ_{output} as an estimate for input θ_{input}. The resulting waveforms are represented in black in Figure 4.7 showing the modelled waveforms using the *S*-wave source inclined for various angles such as 0.8°, 1.15°, 1.72°, 2.3°, 2.9° and 5°. The other way to model the waveforms is to use a percentage of initial *P*-wave displacement instead of inclination angle. The results of this method are shown in blue.

Figure 4.7: Displacement waveforms of PMMA using a 15 mm S-wave transducer at 1MHz frequency. The experimental data are shown in red, and the inclination model in black for 0.8°, 1.15°, 1.72°, 2.3°, 2.9° and 5°. In blue the S+% of P, where P-wave varies 1, 2, 3, 4, 5 and 17% (initial P-wave displacement varies from 1E-11 to 17E-11 for S=1E-9).

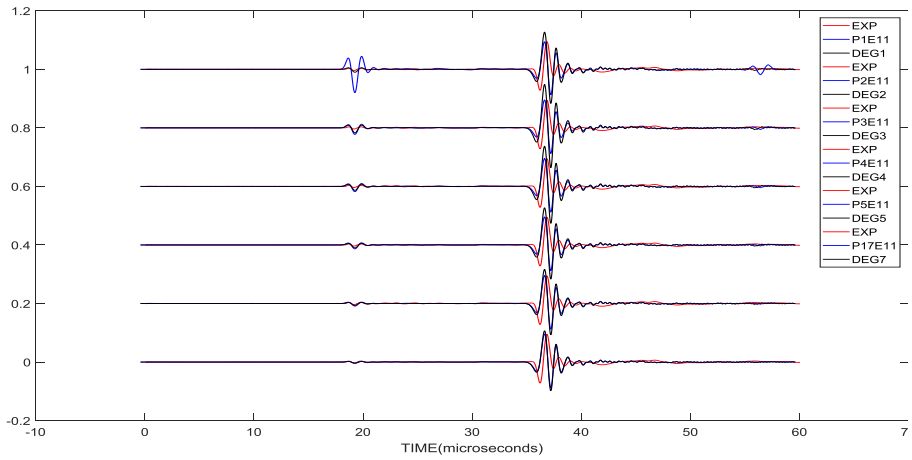

Because the transducers and sample are in hard contact, the assumptions are assumed for both source and receiver. Therefore, I need to account for the reference system and displacement orientation of the receiving transducers, whose sign is opposite to the displacement of the source transducers. Following the same experiment, as shown above, I show in Figure 4.8 that the positive and negative contribution to the initial *P*-wave displacement produces a phase shift which is zero for a negative value.

Figure 4.8: Displacement waveforms of AL using S-wave transducer with a frequency of 1 MHz. The waveforms are estimated using inclination (blue) and induced P-wave input (magenta).

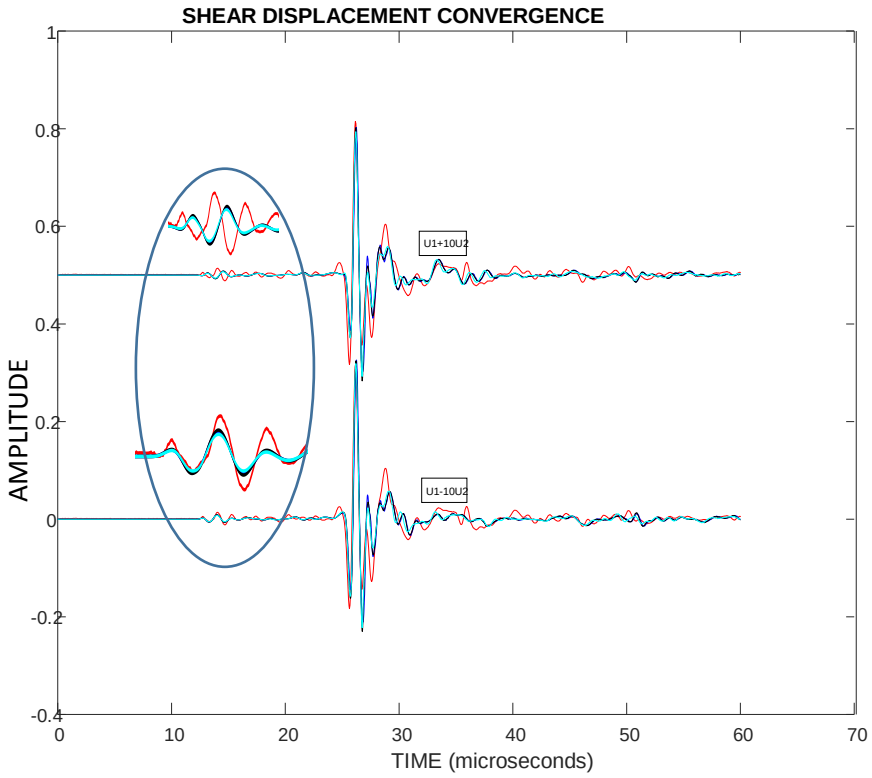

Compared to the experimental data, the best inclination angle is equal to 0.8°. By increasing both the inclination as well as the *P*-wave displacement input, the modelled *P*-wave amplitude increases linearly with the test set. From these observations, it is possible to reduce the waveform misfit between the model and measured data. The best match is obtained for about 1° *of* inclination and 1 % of induced *P*-wave displacement. The accuracy of the waveforms relies on the best inclination of the shear motion along the sample surface or the amplitude of the induced *P*-wave displacement.

4.5. Inversion of waveforms using a homogeneous and isotropic real sample

The inversion of elastic parameters can be time-consuming and very expensive due to the amount of iteration during the traditional search algorithm in the forward model workflow (Nzikou *et al.* 2018). As discussed in Nzikou *et al*. (2018), this section will deal with the inversion of ultrasonic waveforms transmitted using S-wave transducers in the above experiment.

4.5.1. Inversion workflow

In the following figure, the inversion workflow algorithm is schematically shown.

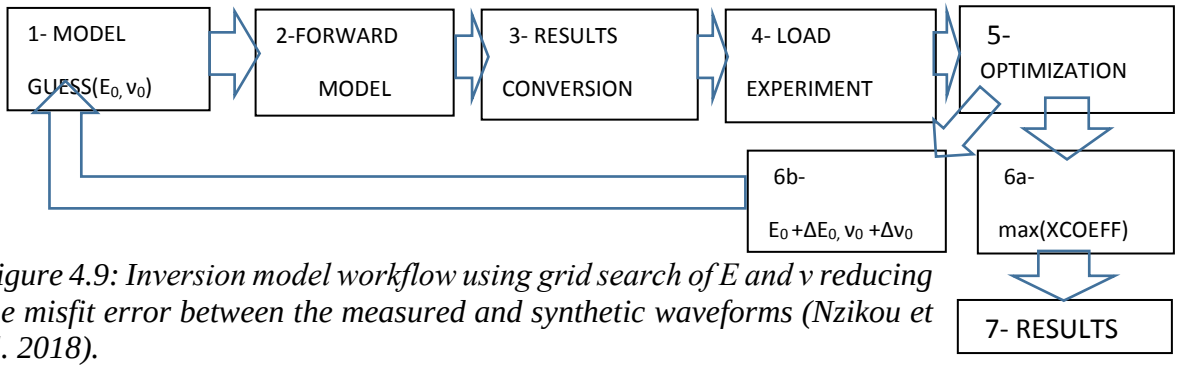

Figure 4.9: Inversion model workflow using grid search of E and v reducing the misfit error between the measured and synthetic waveforms (Nzikou et al. 2018).

This section deals with the inversion of the transmitted waveforms in the AL and PMMA samples following the workflow shown in Figure 4.9 (Nzikou *et al.* 2018). This method gives good results for elastic parameters estimation using a homogeneous and isotropic sample since the amplitude of the signal is only a function of the frequency input. The optimization algorithm is based on the cross-correlation function.

4.5.2. Results validation

To validate the results acquired from *S*-wave transducers in the AL and PMMA samples, I used the ultrasonic frequency source of 1 MHz and applied both inclination and induced *P*-wave input to match the measurement and forward model above. In Figure 4.10, the *S*-wave waveforms are modelled using pure *S*-wave input. The blue and black show the inverted and forward model compared with the experiment (red). These results agree well for both *P*- and *S*-wave amplitude.

Table 4.4: Inverted elastic parameters of the AL sample using three methods.

Methods	***P*-wave (*μs*)**	**S-wave (*μs*)**	***P*-velocity (*m/s*)**	***S*-velocity (*m/s*)**
S+%P and Inclination	12.38	25.40	6322	3022
Experiment	12.38	25.40	6322	3022

As a results inversion, I get very good estimates of the elastic parameters for E=69 *GPa* and v=0.35. Then using cross-correlation methods to identify first breaks (discussed in chapter 3), I estimate the traveltimes T_P, T_S and velocities V_P, and V_S reported in Table 4.4 for AL sample.

Figure 4.10: Inverted waveforms of AL using 1 MHz S-wave transducer. (a) Pure shear motion, and (b) Shear suffering with less than 1 % inclination. The experiment is in red, and forward in blue (top figure) and inversion in black.

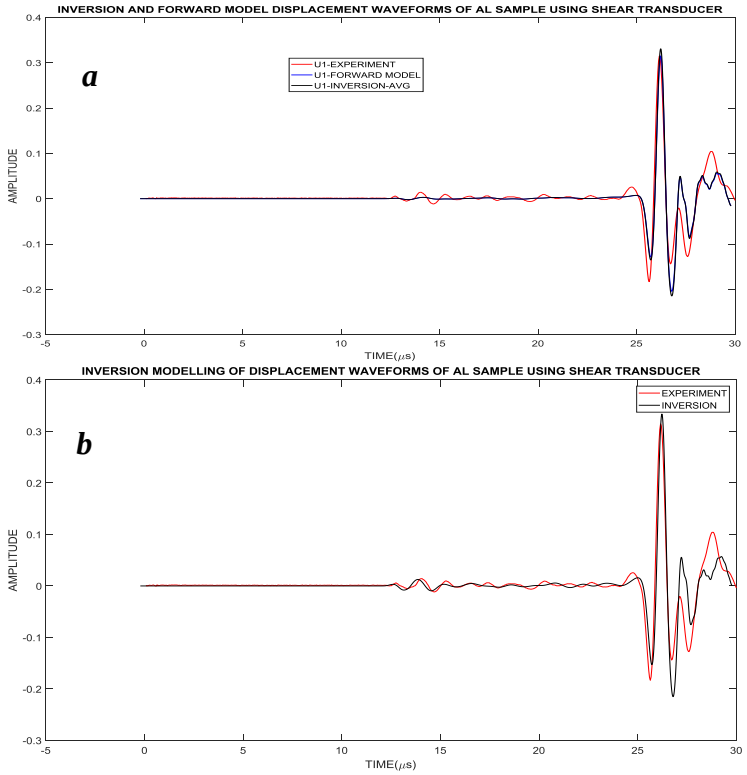

The robustness of the inversion is tested for accuracy and efficiency using the PMMA sample. In order to find the range of inclination angle and initial induced *P*-wave displacement, I show in Figure 4.11 the waveforms in the PMMA sample for various initial *P*-wave displacement values. Similarly to Figure 4.5, by increasing the percentage of the initial U_2 input, the *P*-wave amplitude output increases. For *S*-wave displacement $U_2=1$ nm, the best waveform match lies for U_2 between 0.01-0.02 nm *(*about 1 to 2 % of the required induced *P*-wave displacement input*).* For all the iteration, the inverted elastic parameters are E=6.065 *GPa* and ν=0.316.

Figure 4.11: Inverted waveforms of PMMA using S-transducer with 1MHz frequency. The source S induces a slight displacement along the axial direction of magnitude ranging from 1E-11 m to 17E-11 m. In red and black are the experimental and model data, respectively.

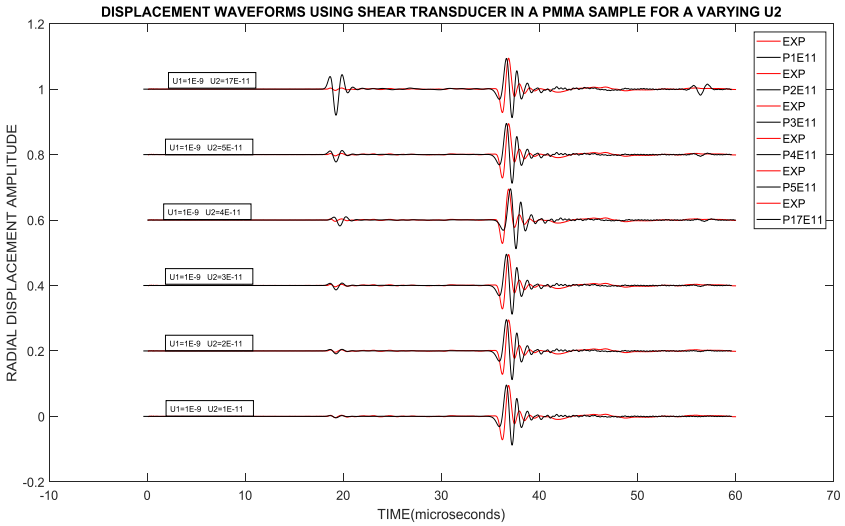

4.6. Results Discussion

The waveforms of the AL and PMMA samples have been investigated and their elastic parameters accurately modelled. The best waveform match depends on the source input. The higher waveform correlation has been shown using the experimental input known as PZT. The waveforms misfit of later events is best achieved using a normalization workflow earlier described as NBA. The validity of this normalization process is shown in Fig 4.3 and they fit the later events especially well. There was not even a slight difference for the PMMA sample due to its larger diameter. The normalization of the individual traces should be accounted for to compute the average waveform from the entire set of traces that correspond to the receiver.

The inversion results accurately reproduce the waveforms and the elastic estimates of both PMMA and AL. To match the observed *P*-wave first breaks and amplitude shapes in the measured data, the source and receiver transducers are assumed to suffer a few degrees of inclination angle or initial induced *P*-wave displacement. The two assumptions show that with less than 1 % of the value of inclination angle and *P*-wave displacement, the full waveforms can be accurately inverted as well as the elastic parameters.

Chapter 5: Modelling the effect of saturation using ultrasonic waveforms

Most of this thesis assumes that ultrasonic measurements are made using homogeneous samples. However, in some applications, most samples are inhomogeneous on some scales. While ultrasonic measurements cannot resolve small scale inhomogeneities such as pores or small fluid patches, they can help understand inhomogeneity on a scale larger than or comparable with the wavelength. One example is ultrasonic measurements during gas sorption in nanoporous media (Schappert and Pelster 2014, Page *et al.* 1995). When gas pressure increases, the gas is adsorbed gradually and uniformly. Any spatial fluctuations of the adsorbed fraction are much smaller than the wavelength, and their analysis requires the use of poroelasticity theory, which is beyond the scope of this thesis. Conversely, when gas pressure decreases, the sample dries from the surface (desorption), forming a distinct large scale cylindrical structure. Thus treating the sample as uniform may lead to unphysical conclusions. In this chapter, I model ultrasonic wave propagation during desorption of a hydrocarbon gas by the nanoporous glass (Page *et al.* 1995). Excellent agreement between my simulations and experimental data confirm my assumptions about the spatial distribution of liquid saturation during desorption.

5.1. Introduction

In petroleum geophysics, the saturation of a porous medium is a topic of interest and has been used to extract the permeability of fluid reservoirs. Also, many natural and synthetic materials of industrial relevance have a micro-to-nanoporous structure, providing high surface area per unit mass and being capable of fluid adsorption and desorption. The interaction of the fluid with a porous solid matrix depends on the contact types and areas between the solid and fluid. The presence of fluid in pores changes the overall stress and other physical properties of rocks (Caspari *et al.* 2011, Gor *et al.* 2017, Rouquerol *et al.* 2013, Mavko and Nur 1975, Toms *et al.* 2007).

The rock properties, for instance, are affected by the state of patches and inhomogeneities of the rock matrix, causing the squirt flow of the fluid within interconnected pores (Mavko and Nur 1975, Müller *et al.* 2010, Brajanovski *et al.* 2005). While the volume of fluid adsorbed by a nanoporous sample can be routinely measured (Rouquerol *et al.* 2013), the spatial distribution of the fluid (patches) inside it is not easy to estimate. The non-uniformity of the fluid distribution in a nanoporous sample affects many of its physical properties. Pore fluid-induced stresses strongly depend on the saturation of pores (Gor *et al.* 2017): therefore, the spatial distribution of fluid affects the strains in materials. The strains can affect the permeability of such media (Pan and Connell 2007).

One method that can shed light on the details of fluid distribution during sorption (adsorption and desorption) is the ultrasonic technique: specifically, the dependence of ultrasonic velocity on saturation. The theory of poroelasticity demonstrates that the dependence of the elastic modulus on liquid saturation is controlled by the size of the patches (Toms *et al.* 2007).

On adsorption (when vapour pressure increases), the spatial distribution is largely uniform. Ultrasonic data suggests that there are some slight spatial heterogeneities, but these are much smaller than the ultrasonic wavelength. Thus velocity variation and attenuation are probably related to wave-induced fluid flow between patches, described using the theory of poroelasticity (Page *et al.* 1995, Gurevich *et al.* 2019). However, the poroelastic analysis is beyond the scope of this thesis.

On desorption (when vapour pressure decreases) the fluids dry from the surface, forming a radially dependent pattern of patches. The characteristic scale of this pattern is larger than the

ultrasonic wavelength. Hence the fluid flow between patches is neglected because wave attenuation is dominated by the reflection. Therefore this situation can be described by the theory of elasticity (with the modulus of each part of the sample described by the Gassmann theory (Gor and Gurevich 2018)). This thesis only focusses on the modelling of ultrasonic measurements during desorption of hydrocarbon gas by the nanoporous glass. Note that 100 % saturation for adsorption means pores are fully saturated with liquid, while for desorption the same means that pores are totally empty (dry sample).

In Figure 5.1 a somewhat strange pattern can be seen in the relative change of moduli (Page *et al.* 1995, Gurevich *et al.* 2019). The *P*-wave modulus at some intermediate saturation is lower than for dry media. Moreover, this is accompanied by attenuation, which is not expected for elastic media. This pattern could be explained by the heterogeneity of fluid distribution (patches). Indeed, if the scale of the saturation pattern is larger than the wavelength, then the concept of the effective medium is inapplicable, and the concept of modulus loses its meaning.

Figure 5.1: P-wave modulus relative change for desorption experiment (Page et al. 1995).

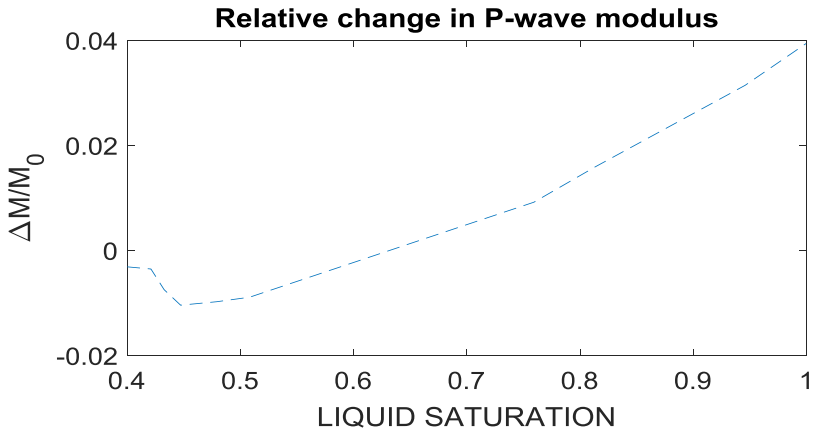

Figure 5.2: Relative change of the P-wave velocity during desorption (Page et al. 1995).

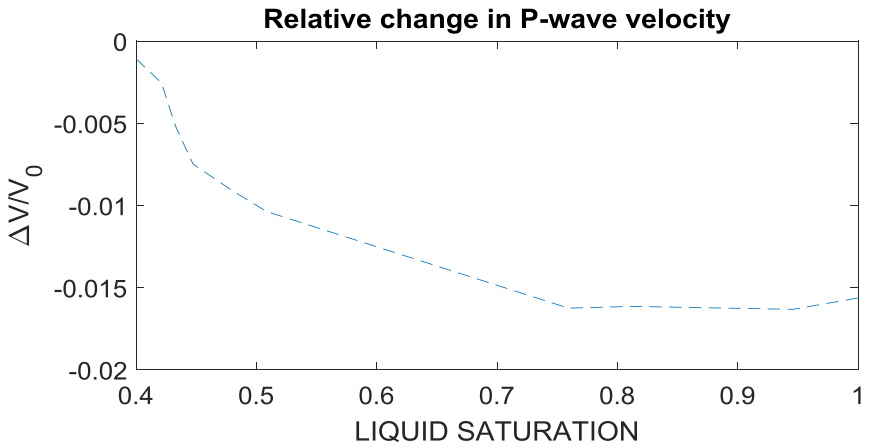

In Figure 5.2, the velocity versus saturation plot shows that as the saturation decreases, the velocity initially remains almost the same as in the fully saturated sample. This suggests that at large saturations (>75 %) the wave travels largely in the inner fully saturated core of the cylindrical sample. However, computing the modulus using the velocity and density of the entire sample, gives an anomalously low modulus (and attenuation anomaly) at intermediate saturations (Page *et al.* 1995, Gurevich *et al.* 2019).

To confirm the above hypothesis, it is useful to carry out FEM simulations of the transmitted ultrasonic waves, extract propagation velocities and attenuation from the modelled waveforms, and compare the modelled velocities and attenuation against laboratory measurements.

5.2. Data Acquisition

The ultrasonic experiments were performed with the Vycor glass sandwiched between two time-delay rod samples of fused quartz, which were in contact with the transducer source and receiver (Page *et al.* 1995). To ensure optimum ultrasonic transmission, Page *et al.* (1995) use a sample with diameter d=7 mm and length L=3.8 cm, *P*-wave source and receiver transducer with diameter *0.5* in at four frequency ranges between 3 to 15 MHz. A 0.5 in diameter time-delay rod was pressing both ends of the Vycor glass (Page *et al.* 1995).

Using their results, I investigate not only attenuation but also visualise the signal distortion caused by the saturation of n-Hexane in Vycor glass.

5.3. Modelling Workflow

In order to model the experimental data presented in Paige et al., (1995) I disregard the time-delay rod since it was homogeneous and isotropic so the signal does not attenuate in it. This assumption not only reduces the computing time required for a finite mesh grid but simplifies the model experiment as well.

In desorption of n-Hexane in the Vycor glass model, I assume that the source and receiver transducers are directly in contact with the Vycor sample. During desorption, the sample dries out from the surface while the middle core remains fully saturated. As relative pressure and liquid saturation are reduced, the wave travels through this fully saturated core with the same velocity and is not affected by the reduced overall saturation until this core becomes relatively

thin. To mimic the above process, I conduct numerical simulations of elastic wave propagation in a cylindrical configuration shown in the Figure 5.3:

Figure 5.3: Finite element simulation design. The area painted red (of radius Ri) is the fully saturated, and the white area is 40 % partially saturated (R-Ri).

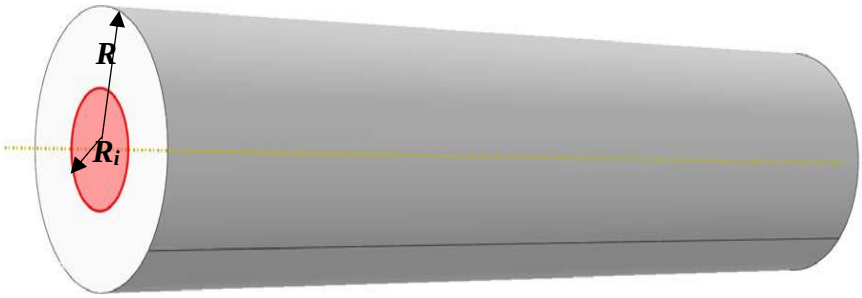

Figure 5.3 shows two concentric homogenous cylinders. The two cylindrical regions are assumed to be elastic with the dry sample shear and bulk modulus (K_{sat}) of a porous medium with porosity ϕ given by the Gassmann-Wood model (GW), which combines Gassmann equation

$$K_{sat}(K_W) = K_0 + \frac{\alpha^2}{\phi} K_W \tag{5.1}$$

with the Wood equations for the fluid mixture modulus K_W (Mavko *et al.* 2009).

$$\frac{1}{K_W} = \frac{1-S}{K_{gas}} + \frac{S}{K_l} \tag{5.2}$$

where K_0 and K_m are bulk moduli of the empty and solid glass, $\alpha = 1 - K_0/K_m$, K_{gas}, and K_l, are the bulk moduli of gas and liquid, respectively, and S is the liquid fraction. In the inner core of the sample S=1, while in the outer shell S=0.4.

To replicate the experiment, the source and receiver transducers fully cover the sample base. The modelling required the user to input the parameters reported in Table 5.1. Some of these parameters are derived from the following equation:

$$\rho_{sat} = \rho_0 + \phi S \rho_l \tag{5.3}$$

$$K_{sat} = M_{sat} - 4/3 G_0 \tag{5.4}$$

where S, ρ_{sat}, K_{sat}, M_{sat}, *and* ρ_0, G_0, ϕ and ρ_l are the percentage of saturation, the mass density of the saturated sample, saturated bulk and *P*-wave modulus, dry density and shear

modulus and porosity and liquid density, respectively. The indices *0*, *l*, *sat* and *40sat* stand for dry, liquid, full saturation and *40 %* saturation, respectively.

Table 5.1: Abaqus/Explicit material properties and fluid adsorb.

ρ_0 *(kg/m^3)*	ρ_l *(kg/m^3)*	K_0 *(GPa)*	G_0 *(GPa)*	ϕ	*Esat (GPa)*	ρ_{sat} *(kg/m^3)*	*E40sat (GPa)*	ρ_{40sat} *(kg/m^3)*
1540	660	10.1	6.86	0.309	17.024	1744	16.781	1622

Two source inputs are used for modelling and they emit a short pulse of about $3\mu s$ at a frequency of 6.2*MHz*. The model is run for 15 μs. To simulate the drying process, the radius R_i of the fully saturated (inner) region is iteratively increased up to the radius of the sample. Note again that *100 %* saturation for desorption means that the sample is dry.

5.4. Application to sorption phenomenon

In this section, I estimate the ultrasonic velocities, elastic moduli and attenuation during the fluid desorption in the porous Vycor glass sample.

Firstly, the ultrasonic velocity and modulus are estimated using a sinusoidal source. Secondly, to measure the performance of the developed inversion workflow and to verify the validity of this algorithm, the desorption experiment is re-run using a Ricker wavelet source input. Finally, the results are compared.

5.4.1. Estimation of elastic parameters using sinusoidal wavelet

Here I present the transmitted waveforms, velocities and attenuation using the sinusoidal *P*-wave source input.

5.4.1.1. *P*-wave waveforms

To produce the waveforms shown in the following figure, the porous Vycor glass sample is sandwiched between the source and receiver.

Figure 5.4: Transmitted ultrasonic waveforms in the Vycor glass sample partially to fully saturated with n-Hexane. The sinusoidal wavelet was used as a source with frequency of 6.2 MHz. The bottom trace is computed from initial saturation (S=40 %) and increment R_i by 2.4 % up to full saturation (S=100 %).

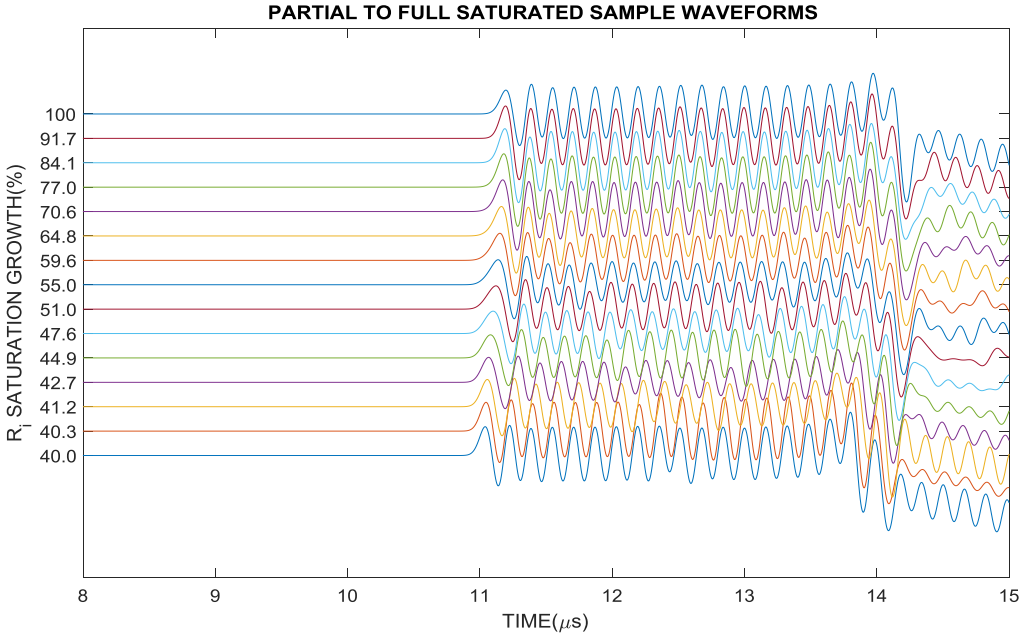

Figure 5.4 shows the waveforms in the porous Vycor glass sample at different liquid saturation levels. The bottom trace corresponds to the smallest value of R_i, while the top trace corresponds to R (dry sample). The intermediate traces are the result of 4 % consecutive increase from the lowest R_i. There is no distortion visible in the entire set of traces of Figure 5.4 between 11 µs to 14 µs. However, there is a strong signal alteration due to boundary reflections later.

5.4.1.2. Velocity and modulus estimation

This section deals with the estimation of *P*-wave velocities and moduli ratio using the sinusoidal source. In order to estimate the velocities, I take a reference trace to be the top trace that corresponds to the dry sample (S=100 %) and manually pick its first break traveltimes. Then I cross-correlate the reference trace with all other traces to estimate their traveltimes (Goshtasby *et al.* 1984). Finally, I calculate the velocities as the ratio of the sample length to the traveltime.

Figure 5.5: Relative change of velocity during desorption of n-Hexane in the Vycor glass.

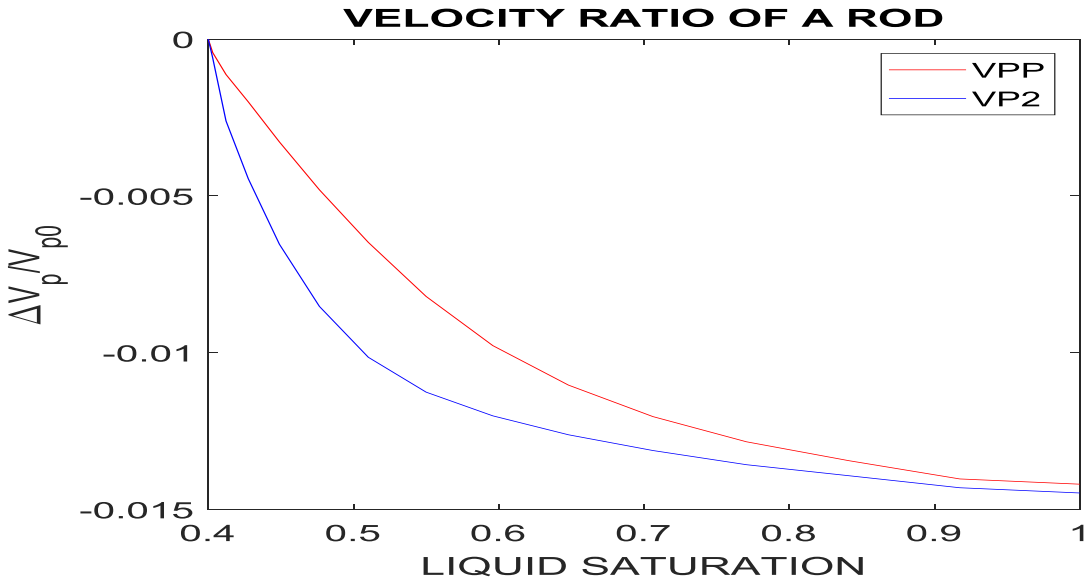

Figure 5.5 shows the wave velocity ratio during desorption of in the Vycor glass sample. In red, the velocity is estimated from the *P*-wave peak amplitude traveltimes, while in blue the velocity is obtained using cross-correlation. The ratio of the velocity is computed using the following equation:

$$\frac{\Delta V}{V_0} = \frac{V - V_0}{V_0} \tag{5.3}$$

where V is the velocity of the individual radius, and V_0 the velocity for the smallest radius.

The percentage change in the velocity ratio decreases by about *1.3*. It is clear that the ratio of change between these two ways of calculation is very small. The two ways of calculation can be used individually to track the rate of change during desorption and further be used for other experiments.

In order to calculate the modulus I used the following equation:

$$M = \rho V^2 \tag{5.4}$$

where the longitudinal modulus *is* M, ρ and V the effective density and velocity. The ratio of moduli is obtained similarly to equation 5.3 by replacing V with M.

Figure 5.6: P-wave moduli relative change during desorption of n-Hexane in Vycor glass.

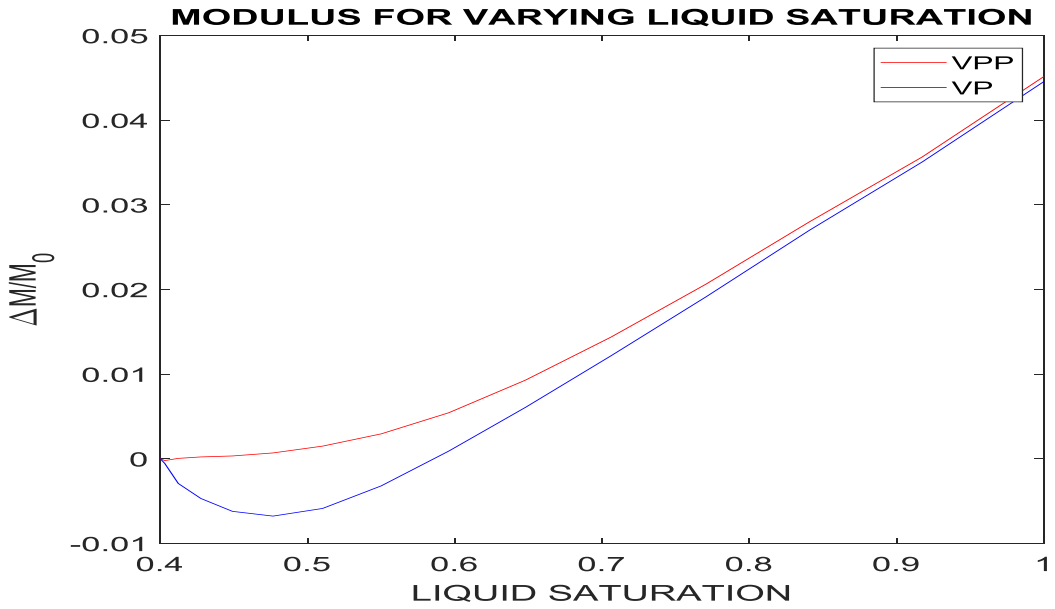

Figure 5.6 shows the change in *P*-wave during desorption. The colour code is the same as in Figure 5.5. The moduli ratio changes by about 4.5 % using the first break velocity. An anomaly of about 0.8 % is visible near liquid saturation of about 46 %, then a rapid rate of increase for the higher saturation. The anomaly of the *P*-wave modulus obtained from modelling agrees well with experiment. This can be an indication of the point of a hysteresis between desorption and adsorption observed in Paige *et al*. (1995).

5.4.2. Estimation of *P*-wave parameters using Ricker wavelet

The aim of this section is to use a *P*-wave source input with the Ricker wavelet amplitude to model both *P*-wave waveforms and their velocity as a function of saturation.

5.4.2.1 *P*-wave waveforms

To test the robustness of the inversion algorithm presented in Chapter 4, I iteratively used a grid search to invert the displacement waveforms using the Ricker wavelet. I estimated the relative change in moduli similarly to section 5.4.1.2.

Figure 5.7 shows 25 inverted waveforms using the Ricker wavelet at a frequency of 6.2 MHz for various percentages of saturation.

Figure 5.7: Transmitted ultrasonic waveforms in the Vycor glass sample partially to fully saturated with n-Hexane. The Ricker wavelet was used as a source with frequency of 6.2 MHz. The bottom trace is computed from initial saturation (S=40 %) and increment R_i by 2.4 % up to full saturation (S=100 %).

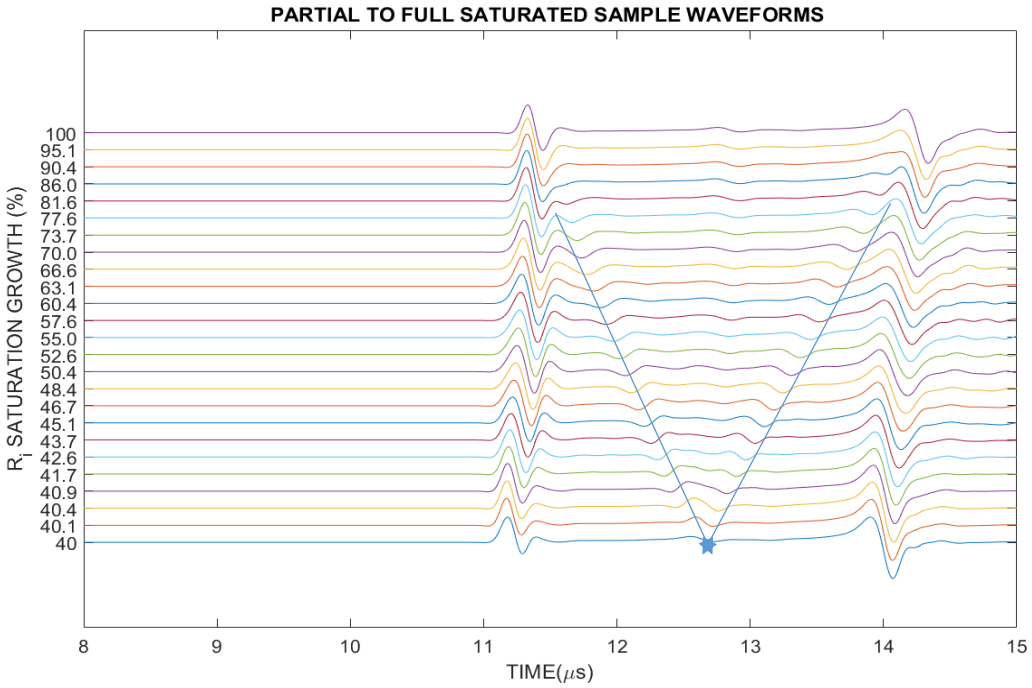

Comparing Figure 5.7 with Figure 5.4, one can see that the waveforms using the Ricker wavelet source are less distorted after 14 µs. Also, two major peaks are observed between 11 µs and 14µs, with the second peak being stronger in amplitude than the first peak (almost by a factor of 2). The higher intensity might be due to the effect of boundary reflection and in-phase interference of once reflected waves. There are a few later events forming a V-shape after the *P*-wave first break arrivals as shown in figure 5.7. This source input makes it possible to analyse the waveforms in more detail for incoming wave packets after the first arrivals.

5.4.2.2 Relative change of the P-wave moduli

Following the calculation in section 5.4.1.2, the relative change of moduli is shown in Figure 5.8. In red and blue are the peak amplitude and the cross-correlation velocities. Contrary to the sinusoidal cross-correlation reference trace, here I used the trace of the lowest saturation (S=0.4).

Figure 5.8: Relative change of the moduli during desorption of n-Hexane in the Vycor glass using the Ricker wavelet source input at a frequency of 6.2 MHz.

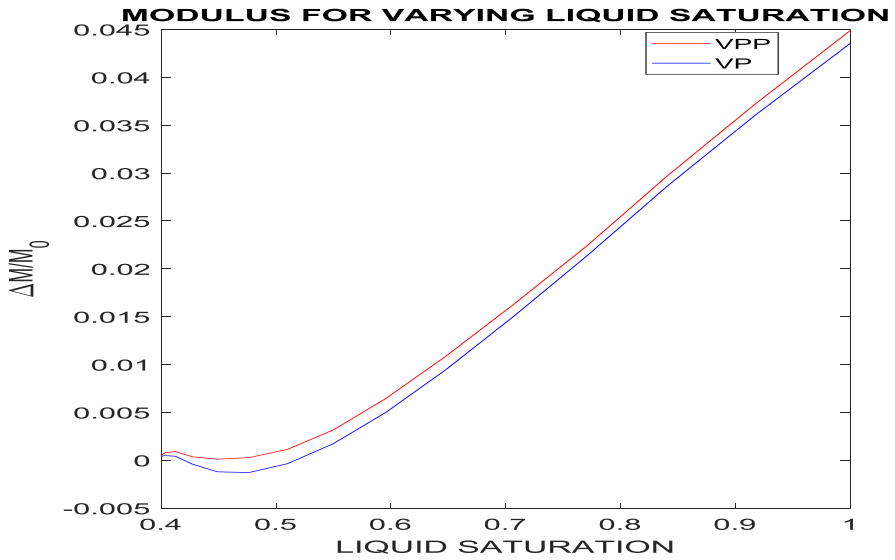

An anomaly of about 0.13 % is observed near liquid saturation of *46 %*. This is 10 % less than the result using a sinusoidal input. Similarly, a rapid increase in the relative change of the moduli is visible for the higher saturation. The general trend is very similar to the sinusoidal input. Also, the total change due to saturation from 40 to 100 % is the same and about 4.5 %.

5.4.3. Estimation of the ultrasonic attenuation

During the propagation of the wave through the saturated medium, the fluid interaction and motion on a pore-scale cause the dissipation of energy. This effect produces the distortion of the signal: in particular, amplitude and velocity become dependent on the frequency of the wave. This is known as the attenuation (*1/Q*) and velocity dispersion. When this occurs, velocities become complex so do moduli as well. The parameter *Q* is called the quality factor and its reciprocal gives the measure in attenuation.

In a complex harmonic representation of waves, *1/Q* is the ratio of 2**Im*(M)/*Re*(M) where M is the appropriate modulus. The higher *Q* means that the medium is closer to the elastic one. There are also different ways to calculate *Q*, one of them is to use the particle displacement of the medium. To describe the attenuation of the ultrasonic waveform during desorption, I used equation 5.5 (Mavko *et al.* 2009):

$$\frac{1}{Q} \approx \frac{1}{\pi} ln \left[\frac{u(t)}{u(t+T)} \right] \tag{5.5}$$

where T is the period of the wave propagating wave through the medium and $u(t)$ is the displacement at any time *t*. I use maximal displacement (amplitude) taking time at *t=0* and at *t=T* to calculate *1/Q*. The results of both measured and modelled attenuation for different saturations are plotted in Figure 5.9.

Figure 5.9: Longitudinal attenuation of the ultrasonic waveform during desorption of n-Hexane. Square and dotted lines represent the experimental and modelled results.

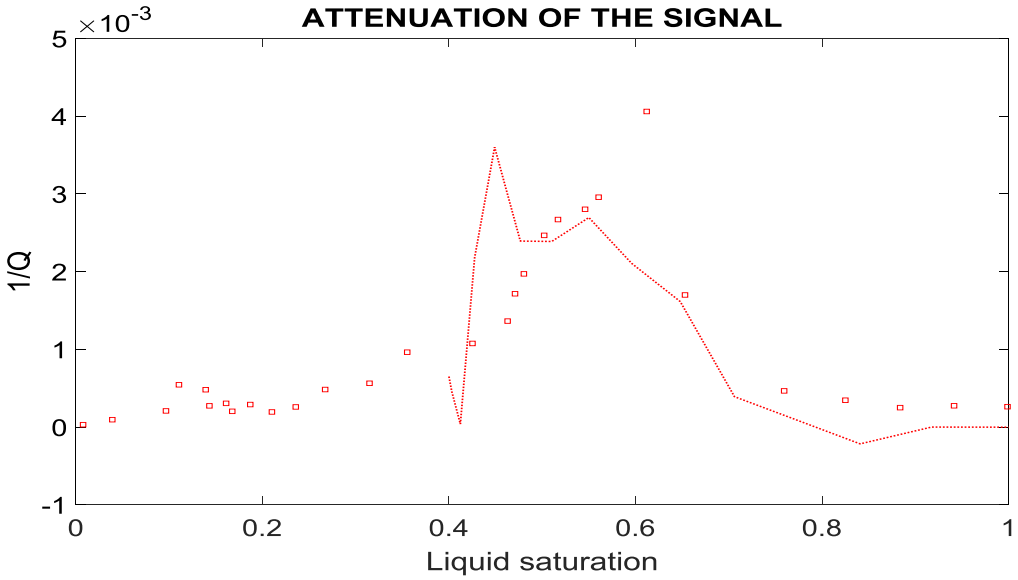

A good agreement is observed from 40 to 100 % saturation. The amplitude decay during desorption of n-Hexane is about 0.5 %. The attenuation of the signal grows for about 0.4 % before its maximum point, then decreases slowly to become stable at higher saturation. The small variance in synthetic and experimental data might be caused by numerical errors. Almost the same results are obtained using a different source input.

5.5. Discussion

The saturation of the porous medium affects the elastic parameters as well as the attenuation. Evidence of these effects is visible through velocity as well as modulus changes for any type of source. The waveforms using the Ricker wavelet are much more informative than those using the sinusoidal input, which is very much distorted after the *P*-wave arrivals due to the interference of reflected waves.

The relative changes in the velocity are about 1.5 %, while the moduli are 4.5 % for any modelled source input. The difference in the anomaly observed in the relative change of moduli for both sources is 10 %. The anomaly of the modulus and the apparent peak of the attenuation

(~46 %) represent the beginning of the hysteresis observed during the adsorption and desorption phenomenon. The anomaly is an indication of the changes in patch size during desorption. The results confirm that for large saturations (>75 %) the wave travels largely in the inner core of the cylindrical sample. Furthermore, the apparent peak of attenuation may be caused by a complex interference pattern between wave arrivals through different parts of the sample and the radial heterogeneity of the fluid distribution.

As the vapour pressure decreases, the liquid fraction drops from 100 % to about 40 % in a cylindrical layer close to the outer surface, while the inner cylindrical core remains fully saturated. As vapour pressure decreases, the thickness of the 'under-saturated' cylindrical layer increases, but the ultrasonic wave still mainly propagates in the fully saturated inner core, until this core becomes too thin, at which point the wave arrival through the under-saturated zone begins to dominate.

5.6. Conclusion

Ultrasonic measurements can reveal the heterogeneous structure of samples on a wavelength scale or a larger one. Numerical simulations can help interpret these measurements. Even though the sample is assumed to be homogeneous, the modelling results are in very good agreement with laboratory measurements. Also, even without the knowledge of the source input, Ricker wavelet and sinusoidal source input give good results. This confirms my assumptions about the cylindrical symmetry of the fluid spatial distribution during desorption. Therefore, the inversion procedure developed in this thesis is robust and can be applied to many other nanoporous materials.

Chapter 6: Estimation of the ultrasonic attenuation

Estimation of the ultrasonic attenuation from waveforms is particularly difficult as the amplitudes and power spectra may be affected by the interference of different arrivals. In addition, most attenuation estimation methods assume that Q is independent of frequency, which may lead to errors if this assumption is violated. Numerical simulations can help estimate attenuation without any such assumptions. In this chapter, I develop a workflow to estimate attenuation from ultrasonic waveforms and apply this workflow to ultrasonic data measured on the same sample at different relative humidities (RH). These waveforms were measured in the Curtin rock physics lab by Yurikov *et al.* (2018) with very good signal to noise ratio. Yurikov *et al.* (2018) estimate attenuation for each RH using the centroid frequency shift method.

Here I model the above experimental waveforms using Abaqus. I estimate attenuation by finding the parameters that provide the best match between measured and simulated waveforms. In order to find the best match, I use waveform inversion (FWI) for elastic and viscoelastic media. In this chapter, I develop a time domain wave mode decomposition approach (MD)-based FWI using the misfit between modelled and measured *P*- and *S*-wave peak amplitudes. This approach firstly mitigates the trade-off between cross-correlation (higher time cost) and peak amplitude match. Secondly, using axisymmetric and full sample modelling, the viscoelastic parameters were accurately inverted.

6.1. Theoretical assumptions

Viscoelastic FWI (VFWI) is a powerful method used to estimate the elastic and viscoelastic parameters of the subsurface, such as *P*-and *S*-wave velocities and attenuation (Tarantola 1986, Mora 1987, Vigh *et al.* 2014). Some inversion algorithms have been applied simultaneously in both the frequency and time domains. However, mixing the frequency and time domains might increase the nonlinearity of the solution (Sirgue *et al.* 2008). By taking into account both modes trade-off and or coupling effects, the viscoelastic inversion can be less accurate (Sirgue *et al.* 2008).

In this thesis, I assume that *P*-and *S*-waves cross-talk is minimal since the sandstone sample is homogeneous (Yurikov *et al.* 2018). Also, the amplitudes of both *P*- and *S*-waves can be manually picked and therefore can be considered separately (Wang and Cheng 2017). Moreover, these waves are most prominent in the laboratory data. To reduce the nonlinearity effects, only compressional and shear modes were considered (Operto *et al.* 2013).

In the experiment done by Yurikov *et al.* (2018) attenuation was estimated (for each RH) using the centroid frequency shift method. However, this method assumes that attenuation factor *Q* is independent of frequency. Hence the *Q* estimates are biased (Gurevich and Pevzner 2015). This method also requires careful separation of signals (to avoid any interference between different arrivals that would distort the power spectrum). I suggest that waveform inversion may give more robust results and even allow us to estimate the frequency dependency of *Q*.

The displacement within the medium $\mathbf{u} = \mathbf{u}(u_x, u_y, u_z)$ is the resulting disturbance coming from *P*- and *S*-waves, so that $\mathbf{u} = \mathbf{u}^P + \mathbf{u}^S$, where $\mathbf{u}^P = \mathbf{u}^P(u_x^P, u_y^P, u_z^P)$ and $\mathbf{u}^S = \mathbf{u}^S(u_x^S, u_y^S, u_z^S)$ are independent (Zhang and McMechan 2010, Wang and Cheng 2017). Even though the separation of wave modes is valid for a homogeneous medium, the assumption considered in this chapter is sufficient to obtain satisfactory results (Wang and Cheng 2017).

6.2. Experimental setup

The data acquisition main system as shown in Figure 6.1 includes two transducer source/receivers 5077PR (Olympus Ltd.), a TDS 3034C oscilloscope and desiccator (enclosed container with the sample inside). In order to reach a stable condition for the relative humidity (RH) measurement, the sample remained enclosed in the desiccator for a minimum of 3 days (Yurikov *et al.* 2018).

Figure 6.1: Experimental setup (Yurikov et al. 2018).

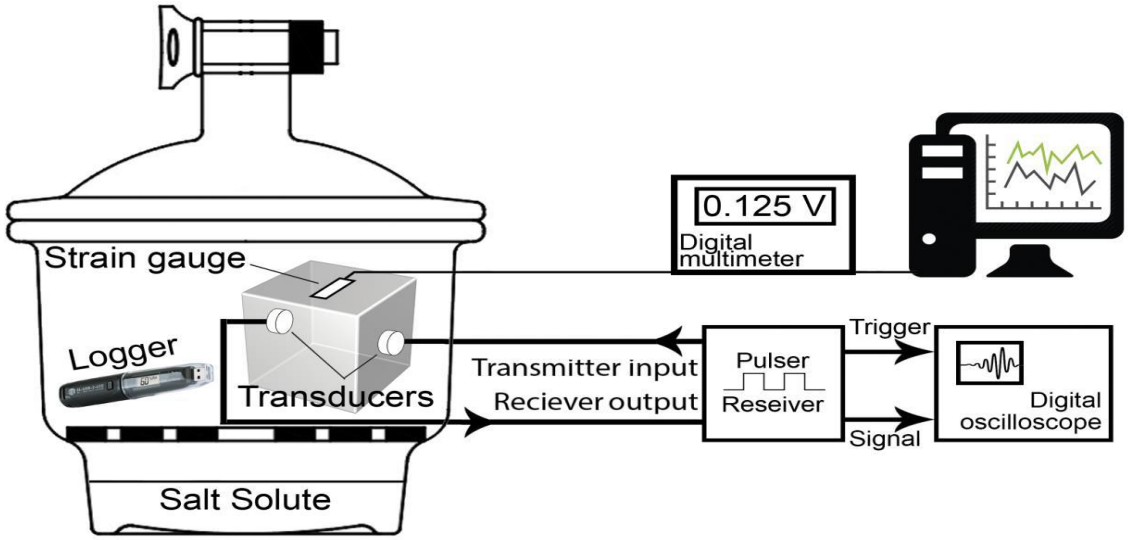

The experimental data were acquired using Bentheim sandstone. The sample was almost homogeneous and isotropic and was mainly composed of 95 % of quartz (Klein *et al.* 2000). Sample total porosity was about 24 % obtained by comparing the mass contrast between fully dried and fully humid sample. To estimate the change in the sample properties caused by water sorption, for various RH, the ultrasonic waveforms were recorded using transmission mode from two shear PZT sources and receivers (V153 1.0 MHz / 0.5 in) glued to the opposite sample faces (Yurikov *et al.* 2018).

6.3. Modelling approach

In order to mimic the experiment with the sandstone sample subjected to ultrasonic frequency S-wave source input of 1 MHz for various RH, I used a model of a cubic sample with two circled surfaces on opposite faces to represent the source and receiver-sample contact.

Figure 6.2: Cubic sample of sandstone (a)-solid model with circle array representing the S-wave transducers with frequency 0f 1 MHz, and (b) meshing grid as an example. The actual mesh grid uses both radial and global set such as RM=0.45 mm AM=0.1 mm.

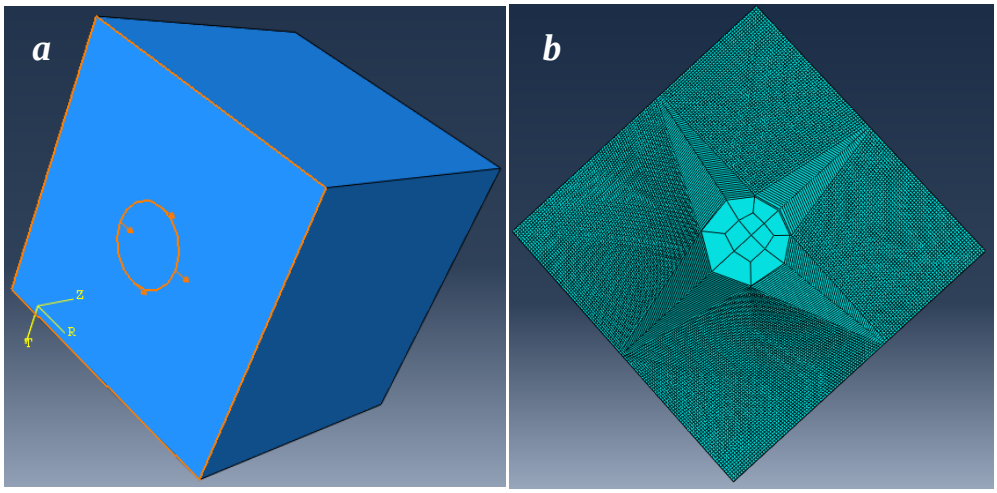

As already mentioned in chapter 2, viscoelastic modelling requires additional parameters *k*, *g* and *τ*. In this workflow, the *RH* is not directly used as a parameter but it is implicitly accounted for through the Prony pair *k* and *g*.

The measured data are not smooth: they contain outliers and therefore they need to be smoothed for later use. The Generalized Maxwell model is sufficient to accurately represent the medium for the waves that propagate in the relatively narrow frequency band. To invert the viscoelastic parameters, I use the workflow below:

1- For the highest RH=100 (which corresponds to the highest attenuation) I define a range of τ to be between $0.7/f_c$ and $1.4/f_c$, where f_c is the wavelet central frequency.
2- Iterate *Re*(*G*), *Im*(G), and τ for *S*-wave mode until the *S*-wave arrival matches the measured arrival.
3- Using the obtained τ, *Re*(*G*) and *Im*(*G*) in step 2, I iterate *Re*(*K*), *Im*(*K*) until I achieve the best match of the *P*-wave arrivals (modelled and measured).
4- Then, I repeat the above steps for all other RH values keeping τ constant.

Using the Generalized Maxwell model the attenuation as a function of frequency is of Gaussian type, as shown in the next figure:

Figure 6.3: Log-log plot of attenuation versus frequency.

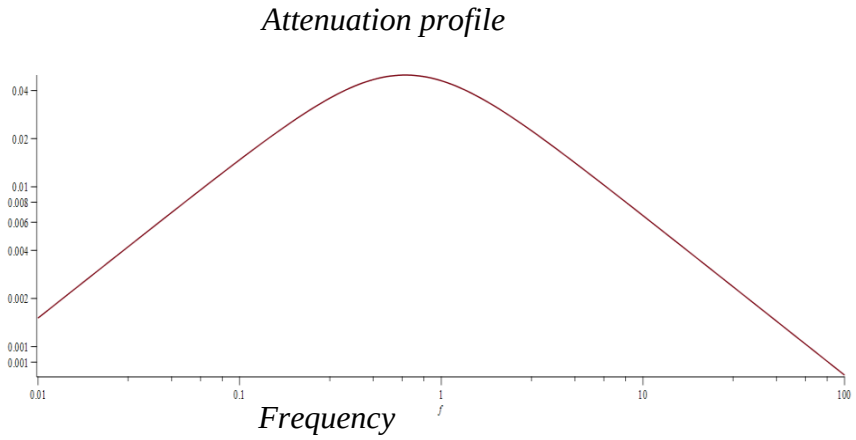

In order to extract the initial value of τ that corresponds to 1 MHz central frequency of the source, a log-log plot was constructed. It gives τ≈0.27 μs, which corresponds to $1/Q \sim f^{0.27}$. By using inversion in step 1, the optimal value of τ≈0.24 μs. Strictly speaking, *Q* is not constant but not too far from constant. However, previous assumptions that constrain *Q* to constant value may be biased (Gurevich and Pevzner 2015).

To avoid the longer computational cost, I modelled the waveforms for the highest and lowest value of RH which gives the range for *E* and the Prony pair (*k*, *g)*. To achieve that, I defined:

- Initial guest parameters E_0, ν_0, k_0, g_0, then run the inversion workflow of chapter 4 (Nzikou *et al.* 2018) for a constant relaxation time τ=0.24μs, to find E_{min}, ν_{min} as well as k_{min} and g_{min} corresponding to the minimal value of RH (13 %).
- The same procedure is then repeated to estimate E_{max}, ν_{max}, k_{max} and g_{max} corresponding to the maximal value of RH (~100 %).
- Finally, the intermediate waveforms are calculated iteratively using a discretization such as $E = E_{min}: \Delta E: E_{max}$, $k = k_{min}: \Delta k: k_{max}$, $g = g_{min}: \Delta g: g_{max}$, where ΔE, Δk, Δg are the step sizes.

This workflow will result in the estimation of the viscoelastic parameters as a function of humidity.

6.4. Viscoelastic parameters estimation using axisymmetric modelling

To estimate the viscoelastic *P*-wave attenuation in the sandstone sample for various RH, I use axisymmetric modelling. To accurately estimate the medium parameters, I first test the

sensitivity of two optimization functions (cross-correlation and peak amplitude function). Then the results of P-wave waveforms, velocities and attenuation are presented.

6.4.1. Sensitivity of optimization functions

Knowing the value of τ, before conducting step 2 and 3 it is important to investigate the effect of the time-window width on cross-correlation results. I used several time-window widths. The sensitivity of the above effect is tested and validated using experimental data for RH=13 %. Figure 6.4 shows the variation of the cross-correlation coefficient for various values of *k* for different time-window sizes.

Figure 6.4: Cross-correlation methods using GSM inversion for a coarse grid k=0:0.25:0.125 for a relative humidity RH=13 %. The mesh grid is set such as RM=0.45 mm AM=0.1 mm and the transducer frequency is 1 MHz.

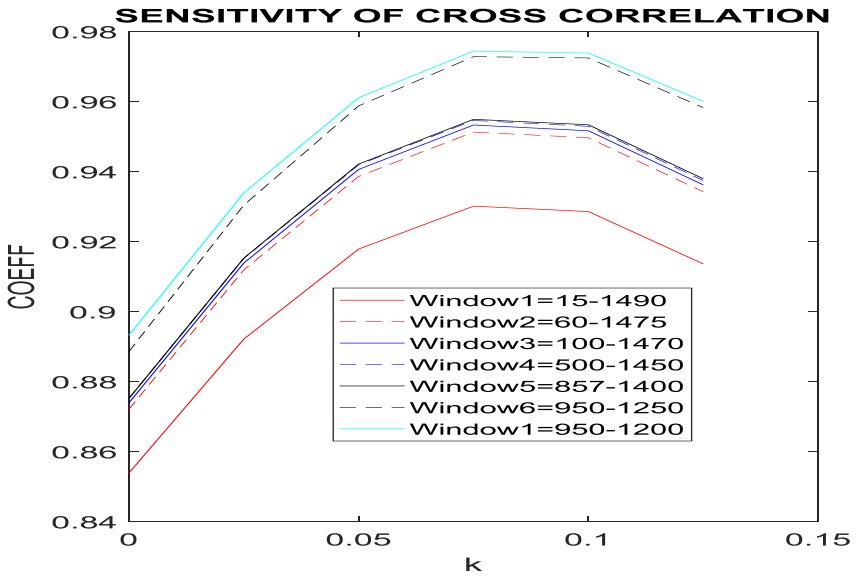

Two types of window such as coarse and finer have been used to investigate the efficiency of the cross-correlation function. For a coarse grid *k*=0:0.25:0.125, the cross-correlation coefficient increases with the window refinement. From all the windows, the maximum cross-correlation coefficient corresponds to *k*=0.075.

Figure 6.5: Cross correlation (a) and Peak difference (b) methods using GSM inversion for refined grid k=0:0.01:0.175 for a relative humidity RH=13 %. The mesh grid is set such as RM=0.45 mm AM=0.1 mm and the transducer frequency is 1 MHz.

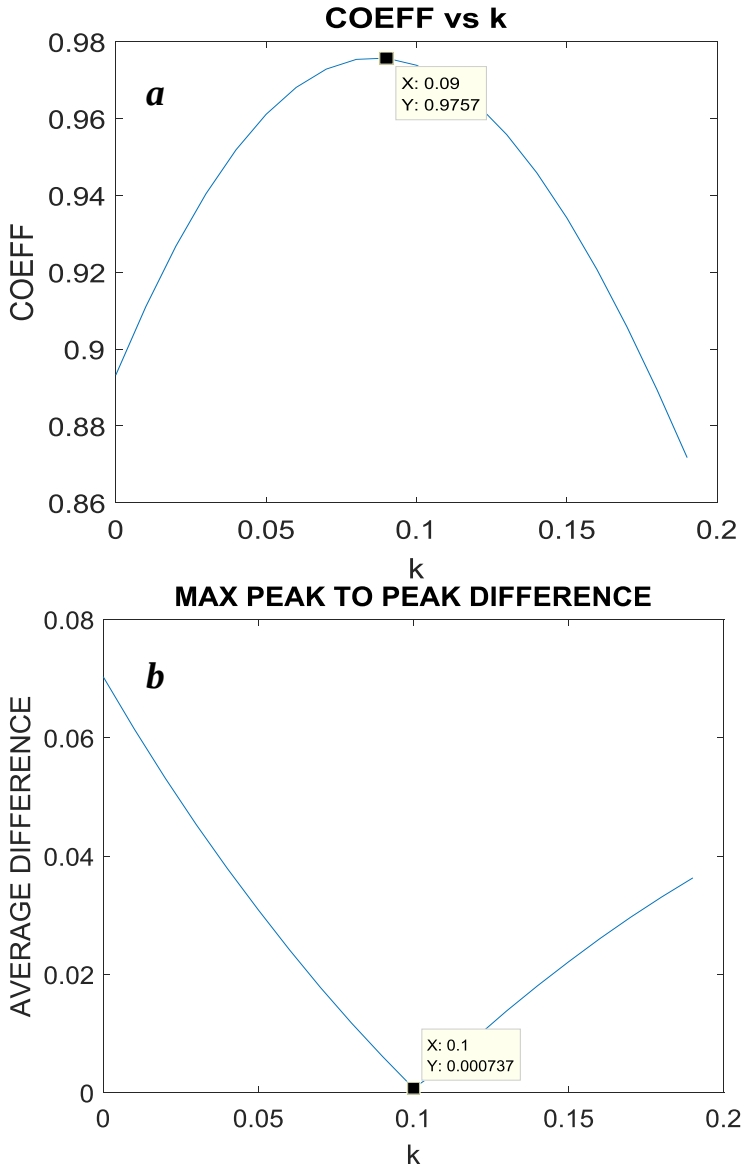

To compare the two optimization functions, I used cross-correlation in one hand and the minimum difference between measured and modelled peak amplitude in the other. Figure 6.5 shows the results of cross-correlation and minimum peak difference. Let label $k_C=0.09$ and $k_P=0.1$, the estimated values associated with the maximum cross-correlation coefficient and minimum peak difference. The results of (*a*) are 11 % lower than (*b*) which match the waveforms shown in Figure 6.6 well.

The top traces show the waveform obtained using amplitude peak difference, while the bottom represents the cross-correlation functions. The red, blue and black traces are the experimental, average and best waveforms match, respectively. The misfit between the estimated values of *k* is shown in Figure 6.6. As previously discussed, the visual difference between the values of *k* of about 11 % between the two functions is shown by the peak amplitude deviation of about 6.5 % from the cross -correlation method in comparison to the experimental data.

Figure 6.6: Displacement waveforms of sandstone at a relative humidity RH=13 % using (a) cross-correlation and (b) minimum peak difference methods. The red, blue and black colors are the experimental, average GSM, and (k_C=0.09 and k_P=0.1) displacement waveforms. The mesh grid is set such as RM=0.45 mm AM=0.1 mm and the transducer with frequency is 1 MHz.

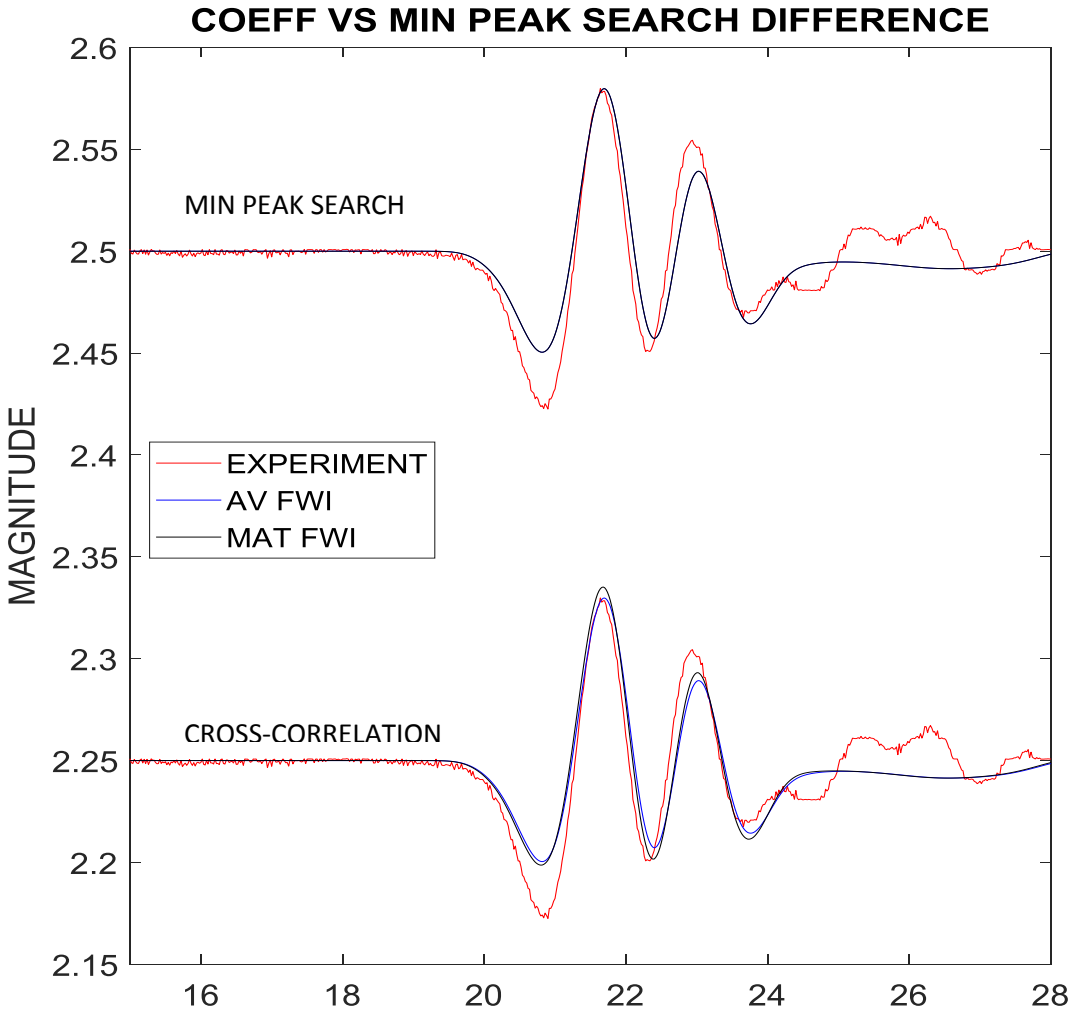

To test the validity of the peak difference optimization function, I include the second sweeping parameter g, whose values represent cross-talk between wave modes. In Figure 6.7 I show the result of the amplitude peak difference by varying k and g simultaneously. The results show the maximum for *k*=0.1 and *g=0.0.*

Figure 6.7: 3D parameter sweep test, which validates the minimum peak difference at k=0.1 and g=0.0. Also, the intermediate maximum is shown in the embedded table.

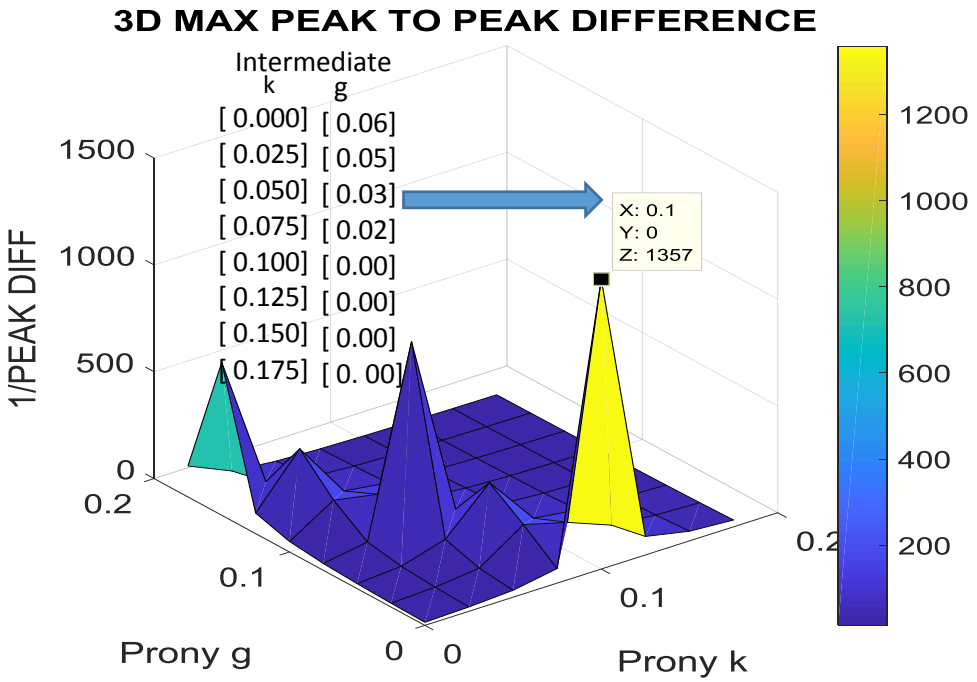

Figure 6.8: Displacement waveforms for RH=13 % obtained using 3D parameter sweep.

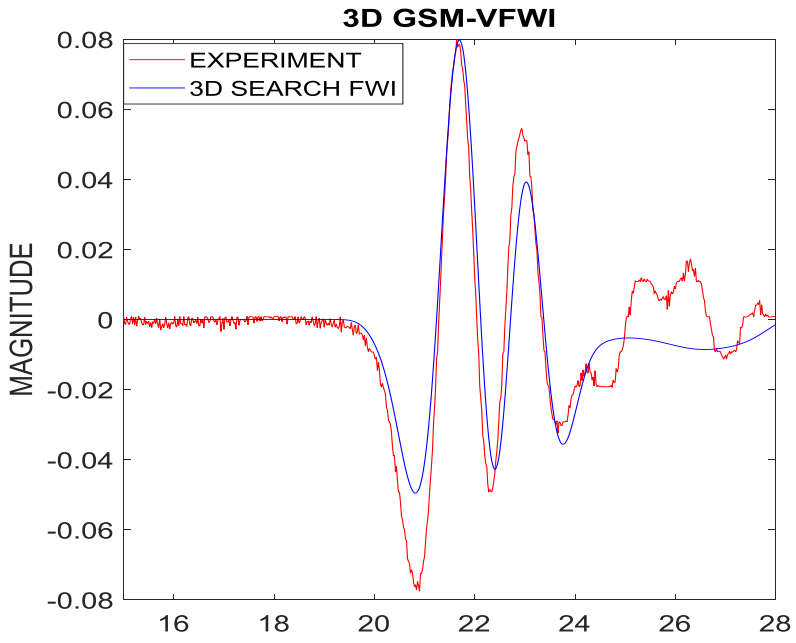

Alternatively, in Figure 6.8 I show the waveforms obtained for k=0.1 and $g=0.0$ which confirm the results of Figure 6.6 (top). The experimental and 3D search results are in red and blue. The inversion using grid search approach even in 3D efficiently reproduces the Prony parameters and elastic parameters of the sample for RH=13 %. There are several intermediate peaks for the various values of g. This test confirms that *P*- and *S*-wave cross-talk does not have an effect using the peak amplitude optimization function.

6.4.2. Computational cost

The main goal is modelling in 3D because of most of the samples are anisotropic in general. That is why I compare the computational cost in 2D versus 3D. Note that in 2D, three parameters E, k and g are varied.

In axisymmetric modelling, for a total time of 28 μs, $k=0:0.125$ and $\Delta k=0.025$ five iterations are needed to cover the entire range of k, assuming that g is fixed. One iteration in Abaqus takes up to 45 seconds for the grid size used above. Therefore, for the entire range of k, the computational cost is about 4 minutes. For the chosen k-grid, the results do not converge (for the cross-correlation as shown in Figure 6.5(a) and 6.6(bottom)), therefore, a finer grid is required. To cover the same range of k with a finer grid, I set $\Delta k=0.01$ which creates 13 iterations. This takes about 10 minutes to reproduce the same results.

The axisymmetric modelling is less costly when using peak difference for about 70 % of the time of the cross-correlation method. However, when both k and g vary, the above cost is multiplied by the number of iterations g. For example, if $g = k$, the required computational time will be 16 minutes for the coarse grid and 100 minutes for the finer grid.

However, using full 3D sample modelling the problem becomes very costly. This is because one iteration takes about 15 minutes. Therefore, using the same (k, g) grid and step sizes, the required time is about 25 times the axisymmetric modelling scheme for both the coarse grid and finer grid.

6.4.3. Results

This section discusses the *P*-wave velocity and attenuation results obtained through the inversion of measured data. Firstly, the *P*-wavefields of the initial and final RH are compared. Secondly, the *P*-wave waveforms and velocities are presented. Finally, the modelled attenuation is compared with the experimental results. Note that the experimental attenuation

in Alexey *et al.* (2018) is estimated using the centroid frequency shift method with RH=13 % as the reference trace (Pevzner *et al.* 2012).

6.4.3.1. *P*-wave displacement wavefields

To investigate the dependence of attenuation on humidity, I showed the displacement wavefields for the two extreme humidity values. The displacement waveforms for RH=13 % and 98 % are shown in the following figure, where half of the source is on the bottom left for each panel. Note that the diameter of the source is smaller than the sample diameter.

Figure 6.9: Ultrasonic wavefield half-snapshots in sandstone sample at a relative humidity RH=13 % and traveltimes of (a)-10.55 μs and (c)-19.53 μs (near first break), and same for RH=98 %. The mesh grid is set to RM=0.45 mm AM=0.1 mm and the P-wave transducer frequency is 1MHz.

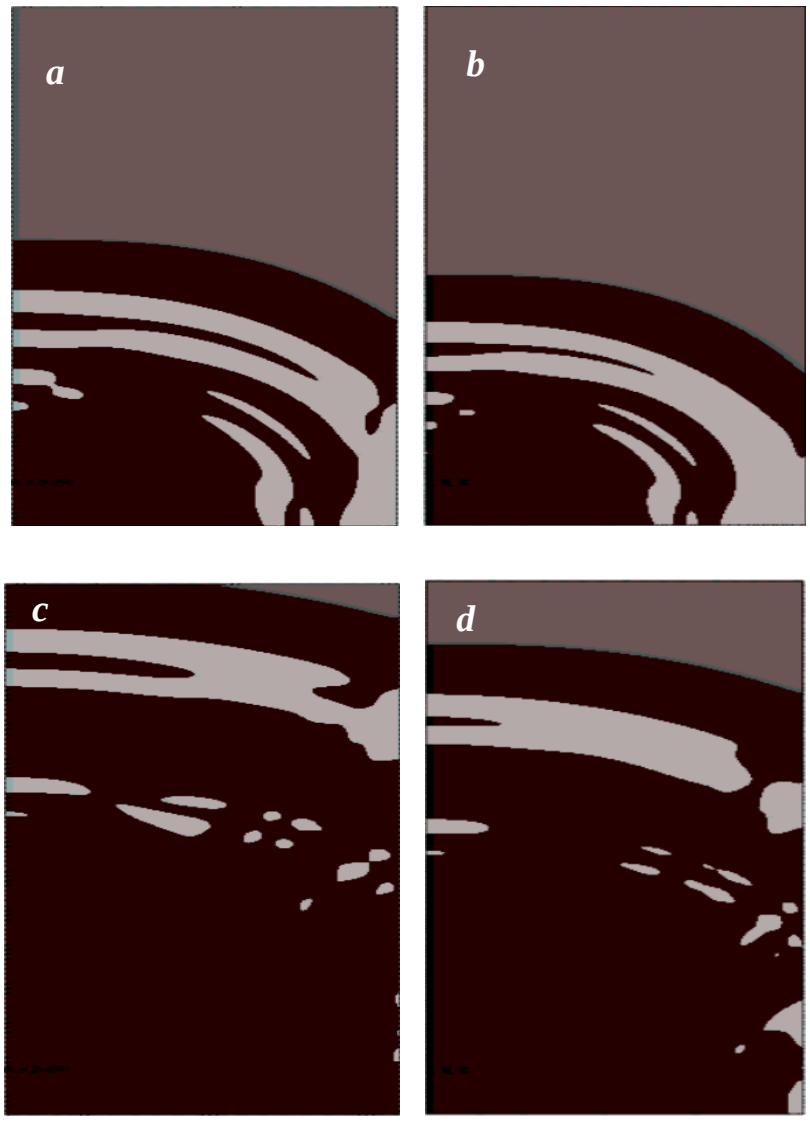

A slight difference in amplitudes for a white spheroidal shape could be seen in figure 6.9 (*a* and *b*). The left centre shape tends to break on a higher value of RH as a consequence of higher attenuation (lower amplitudes). Also, in Figure 6.9 (*c* and *d*) there is a notable difference in wave packets. In (*d*) the wider white amplitude regions are interconnected for higher *RH*, while the smaller ones tend to connect.

The scattering of these nugget-shaped amplitudes is an indication of boundary effects (superposition with reflected waves). Their presence can be used to estimate the effect of reflected waves. This phenomenon is attributed to the saturation of the medium. Also, the attenuation causes the broadening of the wave pulse. However, these images show the time delay caused by the different RH, which can be used as a time calibration.

6.4.3.2. *P*-wave waveforms and velocities

In this section, I present the *P*-wave waveforms and estimated velocities using a standard model with elastic moduli *E* and *v*.

Figure 6.10 shows the waveforms for various RH. The bottom and the top traces correspond to the lowest and highest value of RH. The nugget-shaped areas observed in Figure 6.9 are present in the experimental waveforms but not in the synthetic data. This might be due to the reduction of lower amplitude reflected wave packets during the averaging of the total traces. For the highest RH, the waveform is well correlated. The disagreement of the later events can be due to the time-window of the source input used for the modelling.

Furthermore, I focus on minimizing the misfit between the *P*-wave amplitude of the synthetic and measured data. The general trend of the signal for any RH agrees well with the experimental data: therefore, the waveform inversion is robust.

Figure 6.10: Inverted displacement waveforms using ultrasonic frequency P-wave source input in sandstone for various RH. The waveforms obtained experimentally and by inversion are in red and blue.

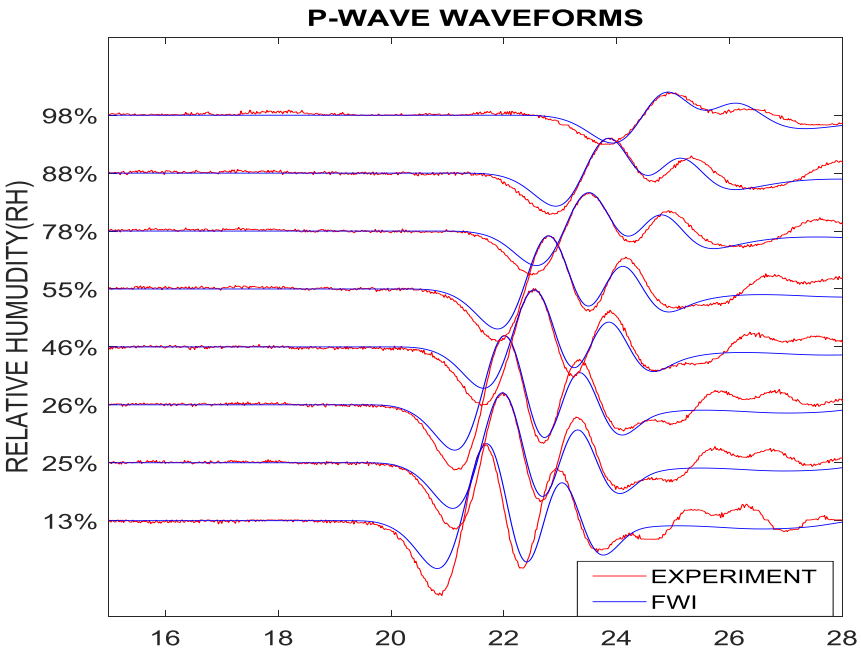

To obtain the elastic velocities, I used cross-correlation to estimate the *P*-wave travel time. The velocities of experimental data are calculated using the traveltimes with the lowest RH as the reference trace (*P*-wave first break is about *19.53 μs*). To calculate the modelled velocities in equation 6.1, I used the inverted value of E_i and ν where i =1…15.

$$V_P^{PRONY} \equiv V_P^i = \sqrt{\frac{E_i(1-\nu)}{\rho(1+\nu)(1-2\nu)}} \tag{6.1}$$

Note that ν=0.06 is constant as a result of inversion (best waveform match for all values of RH). Wave velocities are a function of RH as a consequence of E_i being a function of RH. With increasing RH, E_i decreases, so velocities decreases as well.

Figure 6.11 shows the results of the velocity comparison between the experimental and synthetic data (using Prony parameters E_i and ν). It shows a good velocity agreement. The velocity difference is less than 1 % and it can be attributed to the uncertainty introduced in manually picking the travel time of the reference trace.

Figure 6.11: P-wave velocities obtained from modelled (red) and experimental (black) data for a frequency of 1 MHz using a source input with P-wave amplitude for RH=13 %.

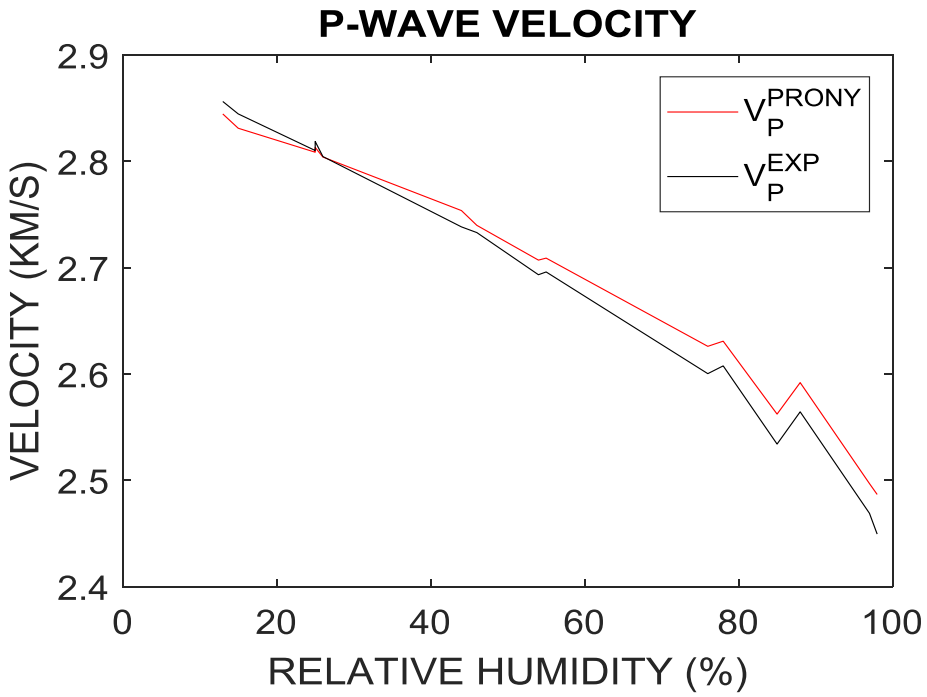

Both approaches used to estimate the velocities are consistent and efficient enough.

6.4.3.3. *P*-wave attenuation Qp

To estimate *P*-wave attenuation, I used the following equation:

$$Q_P^{-1} = \frac{K_0}{K + \frac{4}{3}G} \tag{6.2}$$

where the equilibrium bulk modulus is given by K_0. The shear (*G)* and instantaneous bulk (*K)* moduli are given by:

$$K_0 = \frac{E}{3(1-2\nu)} \tag{6.3}$$

$$G = G_0 = \frac{E}{2(1+\nu)} \tag{6.4}$$

Following Prony formulation:

$$K = K(RH) = K_0\left[1 - k_i\left(1 - e^{-RH/\tau}\right)\right] \tag{6.5}$$

where k_i and τ are the dimensionless bulk modulus and relaxation time, respectively.

Figure 6.12 shows the attenuation of the waveforms and high correlation. A linear dependency is observed for the attenuation in Figure 6.12. However, the data tend to jump a little bit for

close values of RH. This dependency is due to the small change of the Prony parameter k_i in modelled data. The same behaviour is observed on experimental data as well. For an increase of RH from 13 to 100 %, both attenuation results increase by about 25 %.

Figure 6.12: P-wave attenuation profile. The red circles represent the modelled attenuation, while blue is the experimental data (Yurikov et al. 2018).

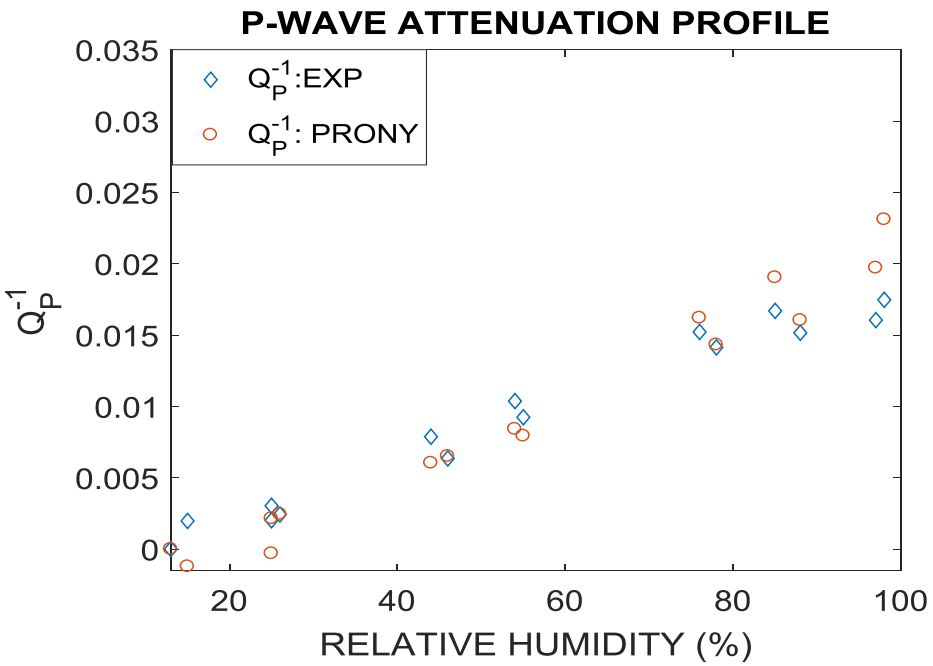

The approach taken for modelling is in excellent agreement with the measured attenuation. Therefore, the behaviour observed with the measured data can be interpreted as a viscoelastic effect. Following this workflow more parameters (k_i, τ, G, K and E), which constitute the viscoelastic behaviour, can be estimated accurately and validated using the misfit between waveforms. This procedure is very robust and mode separation theory confirms its feasibility for sandstone.

6.5. *S*-wave modelling

This section deals with the full modelling of *S*-waves. The model source input is taken to be the *S*-wave amplitude for the lowest RH. Similarly to section 6.4.3, I first present the S-wave wavefield snapshots. Secondly, the waveforms and velocities are highlighted for various RH. Finally, the attenuation estimates are discussed and compared with the measured data.

6.5.1. S-wave displacement wavefield snapshots

To obtain the ultrasonic displacement wavefield snapshots shown in Fig 6.13. I used the source input described above. Then following the workflow shown in the *P*-wave source above, full modelling is conducted instead of axisymmetric. Half of the source is centred for each panel.

One can see very similar behaviour using S-wave source input, as that earlier described for *P*-wave wavefields. The wave field at $t=9\ \mu s$ shows very similar features and the visual difference is the size of the apple-shaped amplitude in white at the centre of the motion. More scattered amplitudes of various shapes are observed for the lower RH. The decrease in scattering for higher RH might be due to saturation of the medium.

Figure 6.13: Ultrasonic wavefield half-snapshots in the sandstone sample at a relative humidity RH=13 % and traveltimes of (a)-9.00 µs and (d)-32.20 µs (near first break), and same for RH=98 %. The mesh grid is set to RM=0.45 mm AM=0.1 mm and the S-wave transducer frequency is 1 MHz.

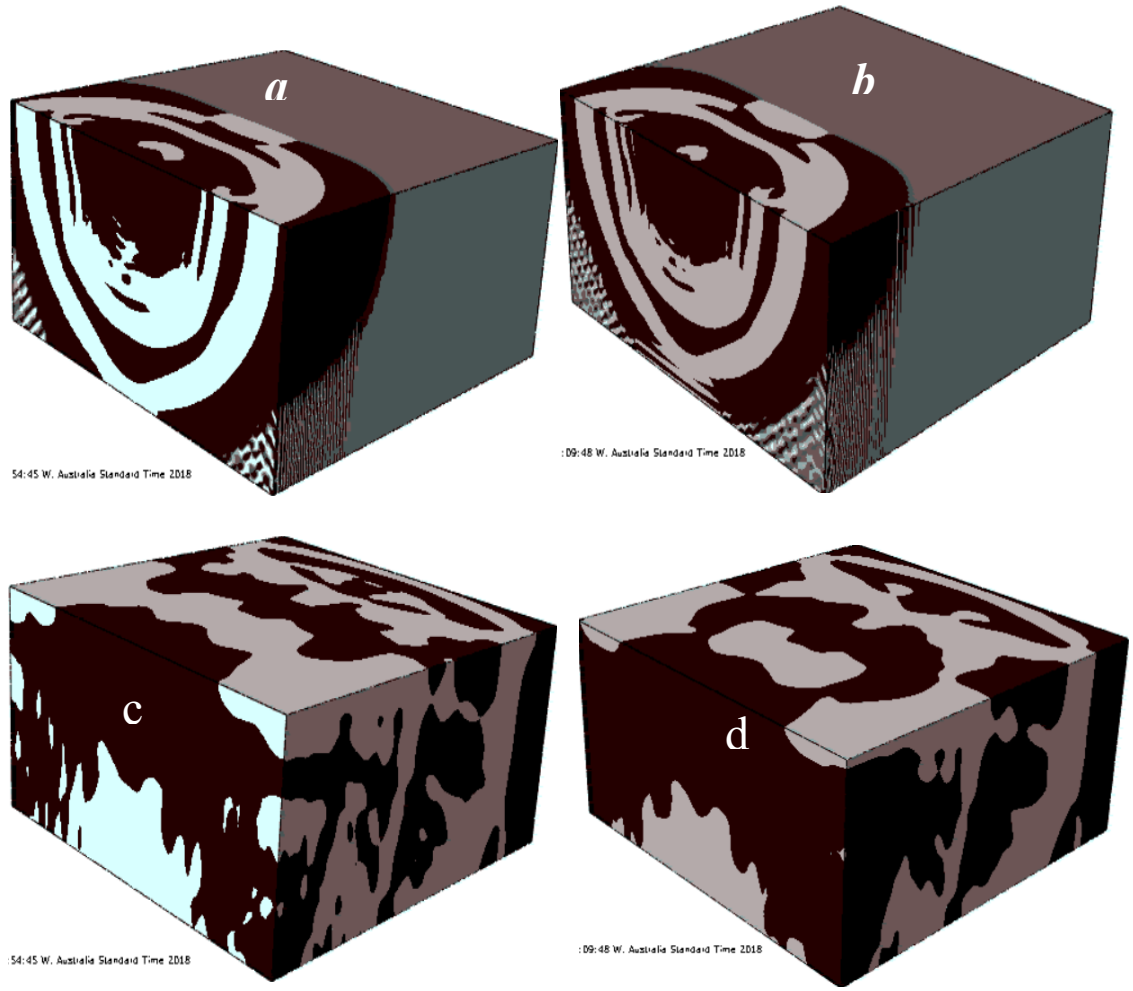

6.5.2. *S*-wave waveforms and velocities

This section deals with the *S*-wave waveforms and velocities. Firstly, the waveforms are computed and shown for various values of RH. Secondly, the *S*-wave velocities are shown and compared following the earlier described procedure for *P*-wave waveforms.

Figure 6.14: Inverted displacement waveforms using ultrasonic frequency S-wave source input in sandstone for various percentages of relative humidity. The waveforms obtained experimentally and by inversion are shown in red and blue respectively.

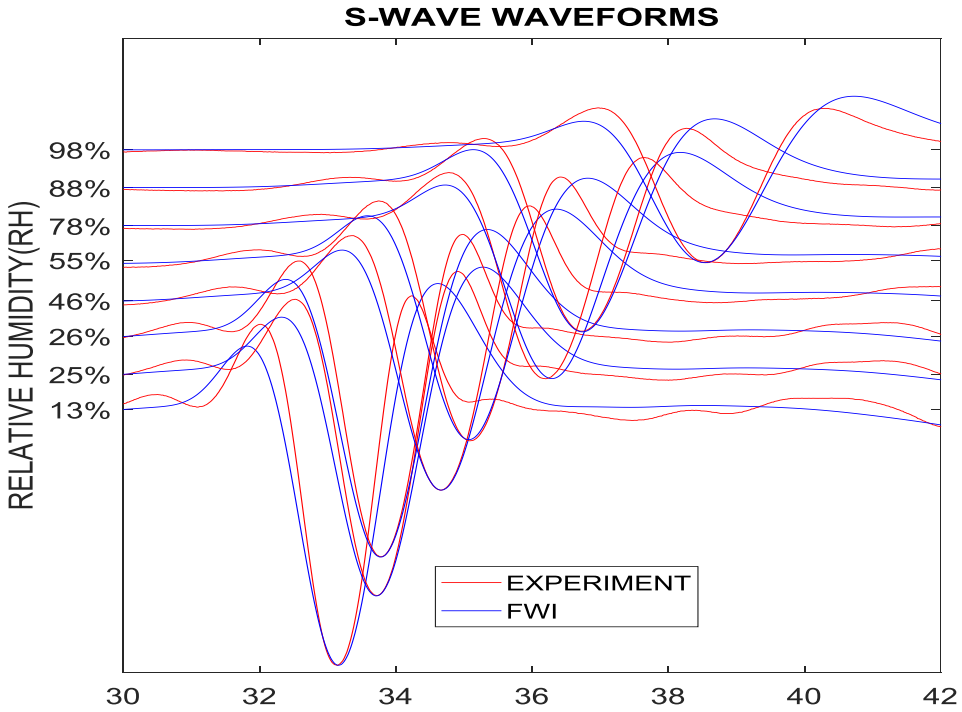

Overall, the modelled waveforms agree well with the measured ones. The misfit of *S*-wave amplitudes (broadening in modelled waveforms) is an indication of the velocity dispersion in the experimental data. Up to this point, I did not account for this dispersion effect in the model.

Figure 6.15 shows the ultrasonic velocity results in the sandstone sample for various RH. The velocity estimated using cross-correlation of the measured waveforms is shown in black, while the red line represents the result of Equation 6.6.

$$V_S^{PRONY} \equiv V_S^k = \sqrt{\frac{E_k}{2\rho(1+\nu)}} \tag{6.6}$$

where E_k need to be converted from instantaneous value to equilibrium one, or vice versa.

$$E_k = E_k(RH) = E_0\left[1 - \mathrm{g}_i\left(1 - e^{-RH/\tau}\right)\right] \tag{6.7}$$

Figure 6.15: S-wave velocities obtained from modelled (red) and experimental (black) data for a frequency of 1 MHz using a source input with P-wave amplitude for RH=13 %.

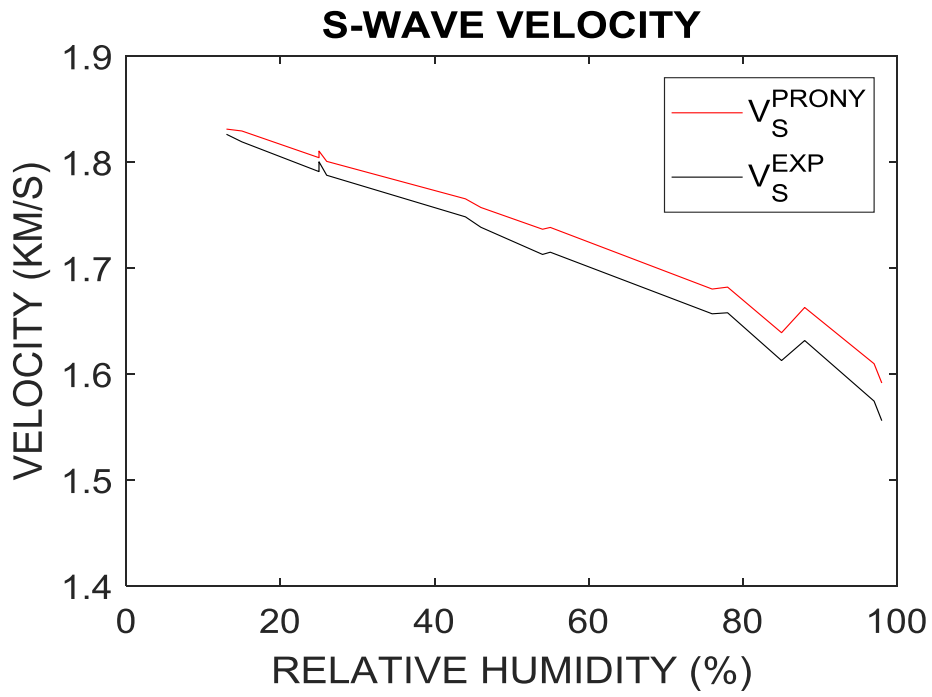

The experimental data corresponds to E_k when the sample is in equilibrium state. Since instantaneous E_k is used in modelling, the results of the velocity calculations should be corrected. After the correction using equation 6.7 was applied, the results are in much better agreement, with the error dropping from 8 % to 1 %.

6.5.3. *S*-wave attenuation Q_S

In order to estimate the *S*-wave amplitude attenuation, I used the formulation in the following equation:

$$Q_S^{-1} = \frac{G_{loss}}{G_{storage}} \tag{6.8}$$

where G_{loss} and $G_{storage}$ are the shear loss (imaginary part of G) and shear storage modulus (real part of G) (Vappou *et al.* 2009). During a wave's propagation through a viscoelastic medium, its amplitude will decay and there will also be a phase shift between the stress and strain. These effects can be inferred to $G_{storage}$ and G_{loss}, which refer to the underlying material elasticity and viscosity, respectively.

Figure 6.16: S-wave attenuation profile. The red circles represent the modelled attenuation, while the blue is the experimental data (Yurikov et al. 2018).

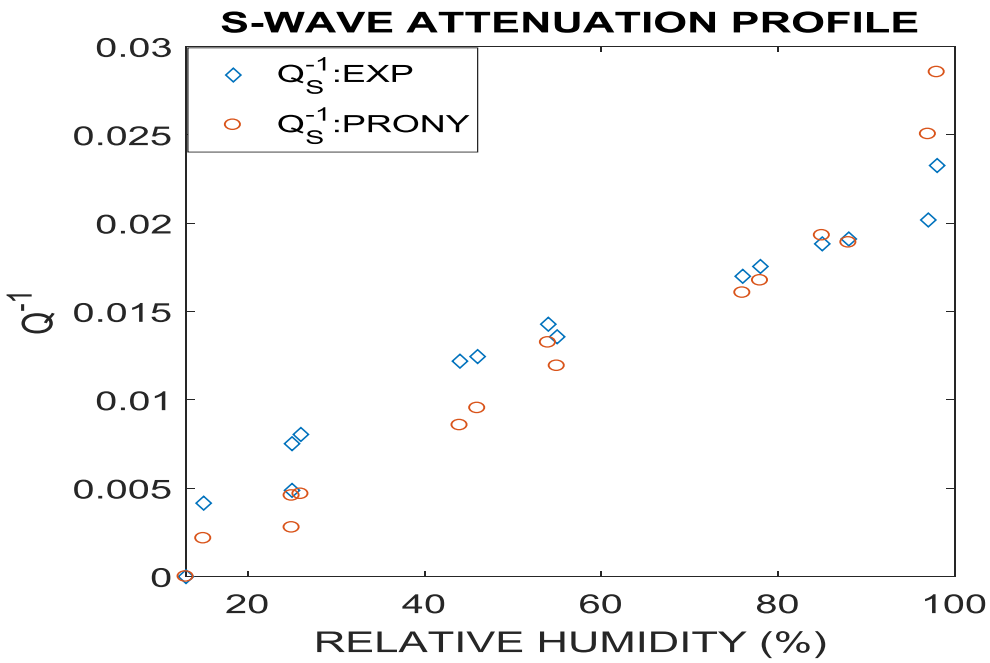

Figure 6.16 shows the *S*-wave attenuation as a function of RH. Similarly, to the *P*-wave model, the *S*-wave attenuation increases for about 29 % with increasing RH. The accuracy of the attenuation estimation relies on the match of the wave amplitude peak which corresponds to the Prony g for *S*-wave. Note that the biggest jump in the data is observed after 90 % of *RH (*about 50 % of the relative attenuation change for the entire intervals.*)*. This could indicate the condensation of vapour on the contacts between sand grains. During wave propagation, the motion of the condensed water will be induced, resulting in higher attenuation in the experimental data. Also, the viscosity of water is higher than vapour: this will results in the jump in the modelled attenuation (see Prony formulation).

6.6. Discussion

The modelling of waveforms can be done using axisymmetric (for *P*-wave) and full (for *S*-wave) model. However, it is possible to account for cross-talk to model both waves simultaneously. There is a need for correction when using either the instantaneous or equilibrium modulus in Abaqus.

The waveform amplitude results can be affected by the grid size of the Prony pair *k* and *g*. However, using a peak amplitude optimization, the modelling is faster than the cross-correlation function in the inversion. The attenuation generally shows almost a linear behaviour for both modes up to 90 % of RH. The small attenuation jumps observed for close values of

RH are possibly caused by the fact that the sample state of equilibrium was not reached. The huge jump in *S*-wave attenuation after the humidity reaches 90 % of RH can be attributed to vapour condensation causing the shear viscosity to increase suddenly.

Numerically, the advantage of the signal separation is that the user can independently investigate both modes. Also, I showed that the elastic modulus E can be used as a third parameter for model testing and validation. In future work, it will be important to account for the slight variation of the relaxation time to correct the broadening of the wavelet.

In situations where the signal is highly distorted, the cross-correlation optimization function does not give satisfying results. The best way to achieve higher accuracy is to use the peak amplitude optimization function. The advantage of this scheme is minimal computational time.

6.7. Conclusion

I developed a workflow for the estimation of attenuation by numerical inversion of waveforms, and the results are broadly consistent with estimates by the frequency shift methods. In order to invert the viscoelastic parameters, I used the assumption of *P*- and *S*-waves mode separation, which was justified by a very good agreement between synthetic and experimental data. Also, the presented workflow can be used to estimate the frequency dependency of attenuation.

Chapter 7:

Conclusion and recommendations

7.1. Conclusion

Transmission ultrasonic experiments are widely used to characterize the elastic and viscoelastic properties of rocks and other materials. Traditionally, ultrasonic velocities have been computed from traveltimes, which are estimated from recorded signals by first break picking or waveform cross-correlation approaches. However, these approaches can sometimes produce significant errors due to the presence of attenuation and dispersion, which smear signal onset and distort the waveforms.

These effects can be mitigated by using an alternative approach: namely inversion of the entire waveform, which I have implemented in the commercial software package Abaqus-FEA. To this end, I have developed a set of Python modules in Abaqus-FEA for numerical simulation of ultrasonic signals for both elastic and viscoelastic samples. I have also developed inversion modules to estimate the elastic moduli and attenuation factors by matching the simulated waveforms to those recorded in the actual measurements.

To achieve higher accuracy of the simulated waveforms, I designed a model for a homogeneous and isotropic sample then later a viscoelastic sample. By using Abaqus, the synthetic waveforms were successfully simulated. Also, the convergence and grid size effects were tested. Theoretically, the grid sizes have a strong effect on the waveform amplitude: the finer the grid the higher the waveform amplitude. To confirm this, the same workflow was applied to compare synthetic with experimental data acquired using Aluminium (AL) and Polymethyl methacrylate (PMMA) samples.

The transmitted synthetic waveforms in the forward and inverted model through AL and PMMA, using both *P* and *S*-waves ultrasonic source and receiver transducers at various frequencies, give the same results. The overall difference between synthetic and measured waveforms is about 2 %. Instead of using a theoretical input signal, a better waveform match is obtained with measured source input. Sometimes the source input signal is unknown. In that case, I showed that the use of Ricker wavelet and sinusoidal source inputs in the inversion workflow give reasonably good results too. Therefore, the inversion procedure developed in

this thesis is robust and can be applied to many materials. When an S-wave transducer is used as a source, an input from *P*-wave is also needed to obtain better accuracy of the modelled waveform. The presence of the *P*-wave occurs even when modelling the shear displacement with a small angle (less than 2 degrees) between sample surface and transducer at the contact, which agrees with measured data.

I then applied the proposed forward modelling workflow to ultrasonic measurements performed during *n*-Hexane desorption in a nanoporous glass sample. Desorption occurs when a fully saturated sample is immersed in vapour with gradually decreasing pressure. Ultrasonic measurements performed during desorption showed a rather confusing pattern, with a *P*-wave modulus lower than the modulus of the dry sample and significant attenuation at intermediate liquid saturation. It was previously suggested that these effects could possibly result from the fact that during this process, desorption (drying) begins from the surface of the sample and proceeds inwards. Thus, at a given pressure, the cylindrical sample effectively consists of two distinct parts: a fully saturated inner core (with a radius depending on vapour pressure) and an outer shell with uniform liquid saturation of about 40 %. Ultrasonic waves travelling along such a system can create a complex interference pattern that can only be analysed numerically. To this end, I numerically simulated the ultrasonic experiment described in the literature using the workflow developed earlier in the thesis. While the experimental waveforms were not available for comparison, the pressure dependency of the phase velocity and of the apparent attenuation estimated from the simulated waveforms match the laboratory measurements very well. Given that my model has no adjustable parameters, this confirms that the two-layered structure accurately represents the saturation distribution during desorption. Conversely, adsorption, which occurs during vapour pressure increase, is known to create liquid patches much smaller than the wavelength, and thus requires the use of poroelasticity theory, which is beyond the scope of this thesis.

For porous rocks, the quality factor *Q* depends on scales of heterogeneities and consequently on frequency. Most *Q* estimation methods (such as the spectral ratio method or the centroid frequency shift methods) assume that *Q* is independent of frequency, which may lead to errors when this assumption is violated. Furthermore, these methods use only the power spectrum of the signal and ignore phase information. Numerical inversion of the entire waveforms offers an appealing alternative. To test this, I applied my viscoelastic inversion workflow to ultrasonic waveforms recorded for a sandstone sample at different relative humidities (RH). These

measurements show very clean waveforms with an apparent effect of attenuation, which increases with increasing RH. The viscoelastic effects were modelled using the so-called Prony formulation with single relaxation time. To increase the robustness of the algorithm and reduce the number of unknown parameters, I used mode separation to perform *P*- and *S*-wave waveforms inversion separately in the time domain. The results for *Q* broadly agree with estimates by the centroid frequency shift method, but also show a modest frequency dependency of *Q*, which can be used to gain further insight into the mechanism of ultrasonic attenuation in room-dry rocks.

The significance of this work is the possibility to calibrate and validate elastic parameters from seismic observation. The forward and inverse modelling developed for both the homogeneous and viscoelastic medium creates the possibility of bypassing the use of conventional first break traveltimes picking completely. Also, it minimizes errors caused by velocity dispersion and unwanted events. The inversion developed for the viscoelastic medium could be extended to study more complex media, such as fractured, porous and fluid-saturated media on different scales.

7.2. Recommendations for future work

The local displacement of the transducer is an important parameter for modelling. It is often not measured, or it is occasionally measured using laser Doppler interferometry (LDI) techniques. However, as earlier discussed, the resulting LDI input does not produce better modelled data than the source input measured from two transducers in direct contact. The contact between transducers and sample surface might have a significant effect on the source input amplitude and shape. A possible way to mitigate some of these issues is to directly measure the source surface displacement i.e. its local displacement while in contact with a transparent sample using LDI. Then, the same procedure should be done while keeping the source away from the sample surface. The two measured signals are then subtracted from each other, which gives the estimate of the contact effect. This could be used to calibrate the measured transducers-transducers input, which could later be used to improve the full-wave inversion (FWI) results.

The effect of heterogeneity significantly contributes to the attenuation of the signal. Even for the sample with a very small degree of heterogeneity, the cross talk between *P*- and *S*-waves

can be significant. To correct this effect, numerical inversion should be applied to the entire waveforms including *P*- and *S*-wave arrivals, reflections from the sample surface and multiples.

The GSM data inversion becomes prohibitively expensive with the increase of the number of parameters to recover. To address this issue, a number of alternative optimization methods such as Nelder-Mead method, quasi-gradient and random directions search methods (McKinnon 1999, Swann 1972, Haelterman et al. 2015) can be used.

Another issue to explore is numerical dispersion. Since in Abaqus the time step is automatically selected for waveform convergence, the numerical dispersion has a negligible effect on the attenuation. However, this may be computationally expensive. Future work should be conducted to estimate the effect of the numerical dispersion for various grid sizes.

Finally, it will be useful to apply my inversion workflow to various rocks to explore the ultrasonic attenuation and, very importantly, its frequency dependency as a function of rock porosity, texture and composition. It can also be useful to compare this attenuation to the attenuation measured at seismic frequencies in the laboratory.

List of figures

List of tables

List of symbols

AL: Aluminium

ABN: Average before normalizing

C: Courant number

CFL: Courant-Friedrich-Levy

c_{ijlk}*: Elastic stiffness tensor*

$\boldsymbol{C}^{*}$*: complex relaxation function*

$\boldsymbol{C}'$*: Real part of* $\boldsymbol{C}^{*}$

$\boldsymbol{C}''$*: Imaginary part of* $\boldsymbol{C}^{*}$

D: Sample diameter

Δt*: Time step*

Δx*: Grid size*

E_0*: Equilibrium modulus*

ε_{ik}*: strain tensor*

EV: elementary volume

E: Young Modulus

E_k*: Instantaneous modulus*

FEA: Finite Element Analysis

FEM: Finite Element Methods

FDM: Finite Difference Methods

FWI: Full-Wave Inversion

FE: Finite Element

f_i*: Internal forces*

f_c*: Central frequency*

F_0: Free energy

GSM: Grid Search Method

G_0: Shear modulus of the dry sample

G_{loss}: Shear loss modulus

$G_{storage}$: Shear storage modulus

GM: General Maxwell

g: Non-dimensional P-wave modulus or P-wave Prony constant

Hz: Hertz

HEX: Hexagonal

HEXD: Hexagonal-dominated

HMI: Harmonic Motion Imaging

Im: Imaginary part

k: Non-dimensional shear modulus or shear Prony constant

K: Bulk modulus

kHz: kilohertz

K_{sat}: Bulk modulus of the saturated sample

λ: Lame Parameter

L_e: External load vector

L_i: Internal load vector

L: Sample length

LDI: Laser Doppler Interferometry

LHS: Left Hand Side

M_{sat}: P-wave modulus of the saturated sample

MHz: Megahertz

M: Mass matrix

M: Modulus

MD: Mode Decomposition

$\boldsymbol{n}_i$*: Unit vector*

NBA: Normalized before average

NDT: Non-Destructive Testing

Q_P*: P-wave quality factor*

Q_S*: S-wave quality factor*

PZT: Piezoelectric transducer

PMMA: Polymethyl methacrylate

ϕ*: Porosity*

RH: Relative Humidity

RHS: Right Hand Side

RPM: Rock Physics Models

Re: Real part

v: Poisson Ratio

ρ*: Material mass density*

ρ_{sat}*: Mass density of the saturated sample*

ρ_0*: Mass density of the dry sample*

ρ_l*: Fluid density*

σ_{ik}*: Stress tensor*

S: Saturation percentage

TET: Tetrahedral

θ*: Inclination angle of the shear wave motion vector*

T: Period of oscillation

τ*: Relaxation time*

T_P*: P-wave first break travel time*

T_S: *S-wave first break travel time*

$\boldsymbol{u}$: *Displacement vector*

$\ddot{u}$: *Particle acceleration*

$\dot{u}$: *Particle velocity*

U_2, U_1, U_3: *Displacement magnitude along each coordinate system*

μs: *Microseconds*

μ: *Shear modulus*

VFWI: Viscoelastic FWI

V: Velocity

V_0: *Velocity of smallest inner shell*

V_P^{PRONY}: *P-wave velocity using Prony formulation*

V_S^{PRONY}: *S-wave velocity using Prony formulation*

V_P: *P-wave velocity*

V_S: *S-wave velocity*

V_{PP}: *P-wave Peak velocity*

V_{SS}: *S-wave Peak velocity*

W: Strain-energy potential

X, Y, Z: Coordinates of an orthogonal reference system

References

Alles, E. J., M. D. Verweij, and K.W.A. Van Dongen. 2010. "Reconstruction transducer surface motion by inverse extrapolation of measured pressure wavefields:." IEEE International Ultrasonics Symposium Proceedings:1458-1461.

Amundsen, L., and M. Rune. 1994. "Estimation of phase velocities and Q-factors from zero-offset, vertical seismic profile data" Geophysics 59:500–517.

Arregui-Mena, J.D. , P.D. Edmondson, L. Margetts, D.V. Griffiths, W.E. Windes, M. Carroll, and P.M. & Mummery. 2018. "Characterization of the spatial variability of material properties of Gilsocarbon and NBG-18 using random fields." Journal of Nuclear Materials 511:91-100.

Assie, A.E., M.A. Eltaher, and F.F. Mahmoud. 2010. "Modeling of viscoelastic contact-impact problems." Applied Mathematical Modelling 34:2336-2352.

Barbero, E.J. 2007. "Finite Element Analysis of Composite Materials." CRC Press (Boca Raton, Florida).

Barbero, E.J. 2013. "Finite Element Analysis of Composite Materials Using Abaqus." CRC Press.

Batzle, M.L. , D.H. Han, and R. Hofmann. 2006. "Fluid mobility and frequency-dependent seismic velocity — Direct measurements: ." Geophysics 71 (1):1-9.

Beloborodov, M. 2017. "Compaction trends of shales: Rock Physics and Petrophysical properties." Curtin thesis (PhD).

Biot, M.A. 1956. "Theory of propagation of elastic waves in a fluid-saturated porous solid: Part 2-Higher frequency range." Journal of the Acoustical Society of America 28: 179–191.

Boubez, T. I., W. R. J. Funnell, D. A. Lowther, A. R. Pinchuk, and P. P. Silvester. 1986. "Mesh generation for computational analysis." Computer Aided Eng. J.:190-201.

Brajanovski, M. 2010. "Theoretical introduction to rock physics: Lecture on the Theory of Elasticity and Poroelasticity." Institute of Acoustics - Chinese Academy of Sciences.

Brajanovski, M., Gurevich B., and M. Schoenberg. 2005. "A model for P-wave attenuation and dispersion in a porous medium permeated by aligned fractures." Geophys. J. Int. 163:372-384.

Brostow, W. , and J.P. Dussault. 1978. "Construction of Voronoi polyhedral." J. Computational Physics 29:81-92.

Caspari, E., T.M. Müller, and B. Gurevich. 2011. "Time-lapse sonic logs reveal patchy CO2 saturation in-situ." Geophysical Research Letters 38:L13301. doi: http://dx.doi.org/10.1029/2011GL046959.

Cavendish, J.C., D.A. Field, and Frey W.H. 1985. "An approach to automatic three-dimensional finite element mesh generation." Int. J. Numer. Meth. Eng. 21:329-347.

Christensen, R.M. 2003. "Theory of viscoelasticity " Dover Publication 2nd edition.

Christensen, R.M. 2005. "Mechanics of composite materials." Dover Publication.

Daley, P. F., and F. Hron. 1977. "Reflection and transmission coefficients for transversely isotropic media." Bulletin of the Seismological Society of America 67:661-675.

Dellinger, J., and L. Vernik. 1994. "Do travel times in pulse-transmission experiments yield anisotropic group or phase velocities?" Geophysics 59 1774-1779.

Gladwin, M. T., and F. D. Stacey. 1974. "Anelastic degradation of acoustic pulses in rocks." Physics of the Earth and Planetary Interiors 8:332–336.

Gor, G.Y., and B. Gurevich. 2018. "Gassmann theory applies to nanoporous media." Geophys. Res. Lett. 45 (1):146-155.

Gor, G.Y., P. Huber, and N. Bernstein. 2017. "Adsorption-induced deformation of nanoporous materials—A review." Applied Physics Reviews 4 (1):011303. doi: 10.1063/1.4975001.

Goshtasby, A., S.H. Gage, and J.F. Bartholic. 1984. "A Two-Stage Cross Correlation Approach to Template Matching." IEEE 375-378.

Gurevich, B., G. Gor, and M.M. Nzikou. 2019. "Modelling acoustic properties of partially saturated nano-porous media." 5th International Workshop on Rock Physics.

Gurevich, B., and R. Pevzner. 2015. "How frequency dependency of Q affects spectral ratio estimates." Geophysics 80:39-44.

Haelterman, R., D.V. Eester, and D. Verleyen. 2015. " Accelerating the solution of a physics model inside a tokamak using (Inverse) Column Updating Method." Journal of Computational and Applied Mathematics 279:133-144.

Hatherly, P.J. 1986. "Attenuation measurements on shallow seismic refraction data." Geophysics 51:250–254.

Ho-Le, K. 1988. "Finite element mesh generation methods: A review and classification." Computer-aided design 20:27-38.

Hossain, M.M. 2017. "Experimental and Modelling approaches to determine the effect of moisture contents, grain contact and confining pressure on effective elastic properies of rock." Doctoral dissertation.

Hujeirat, A. 2003. "A method for relaxing the CFL-condition in time explicit schemes." arxiv.

Jannsen, D., J. Voss, and F. Theilen. 1985. "Comparison of methods to determine Q in shallow marine sediments from vertical reflection seismograms." Geophysical Prospecting 33:479–497.

Kam, K. K. 2010. "Poroelastic finite element analysis of a heterogeneous articular cartilage explant under dynamic compression in Abaqus."

Klein, B., P. Baud, T. Reuschle, and T. F. Wong. 2000. "Mechanical behaviour and failure mode of Bentheim sandstone under triaxial compression." Physics and Chemistry of the Earth, Part A: Solid Earth and Geodesy 26 (1-2):21-25. doi: https://doi.org/10.1016/S1464-1895(01)000175.

Kolesnikov, Y. I. 2008. "Estimation of possible effect of intrinsic velocity dispersion on the results of materials elastic moduli determination." XX session of the Russian Acoustical Society: 180-183.

Kruger, M., C.U. Grosse, and F. Lehmann. 2013. "Automated shear-wave techniques to investigate the setting and hardening of concrete in through-transmission. ." Nondestructive testing of materials and structures (Springer Nederlands).

Landau, L.D., and E.M. Lifshitz. 1970. "Theory of Elasticity " Permagon Press 7.

Lee, W. M. , and W. F. Waite. 2009. "High-frequency normal mode propagation in aluminum cylinders." Scientific investigators report 5142 (USGS).

Liesa, C.L., and R.J. Lisle. 2004. "Reliability of methods to separate stress tensors from heterogeneous fault-slip data." Journal of Structural Geology 26:559–572.

Liu, F., L. Huang, Y. Pang, Z. Shi, P. Xiao, and G. Fang. 2018. "Airborne AFMAG method motion-induced noise simulation and suppression." Journal of Applied Geophysical 159:241-247.

Liu, H., and L. Peselnick. 1983. "Investigation of internal friction in fused quartz, steel, plexiglass, and Westerly Granite from 0.01 to 1.00 Hertz " Journal of Geophysical Research: Solid Earth 88:2367–2379.

Matsushima, J., M. Suzuki, Y. Kato, T. Nibe, and S. Rokugawa. 2008. "Laboratory experiments on compressional ultrasonic wave attenuation in partially frozen brines: , 73, no. 2, N9–N18." Geophysics 73 (2):9-18.

Matsushima, J., M. Suzuki, I Matsugi, Y. Kato, and S. Rokugawa. 2014. "Attenuation estimation using sweep signals in ultrasonic laboratory measurements." Geophysics 79:115-130.

Mavko, G., T. Mukerji, and J. Dvorkin. 2009. "The Rock Physics Handbook: Tools for Seismic Analysis of Porous Media." Cambridge: Cambridge University Press. doi: doi:10.1017/CBO9780511626753.

Mavko, G., and A. Nur. 1975. "Melt squirt in the asthenosphere." Journal of Geophysical Research 80 (11):14444-1448.

McCrum, N.G. , C.P. Buckley, and C.B. Bucknall. 2003. "Principles of Polymer Engineering." Oxford Science Publishing 2nd edition.

McDonal, F.J., F.A. Angona, R.L. Mills, R.L. Sengbush, R.G. Van Nostrand, and J.E. White. 1958. "Attenuation of shear and compressional waves in Pierre shalt." Geophysics 23: 421–439.

McKinnon, K.I.M. 1999. "Convergence of the Nelder-Mead simplex method to a non-stationary point." SIAM Journal on Optimization 9: 148-158.

Meyers, M.A., and K.K. Chawla. 2009. "Mechanical Behavior of Materials." Cambridge University Press, Cambridge. 2nd Edition.

Meza, J., C.M. Faria, R.M. Souza, and J. Cruz. 2007. "Using the ratio: Maximum load over unload stiffness, Pm/Su2, on the evaluation of machine stiffness and area function of blunt indenters on depth-sensing indentation equipment." Materials Research 10:437-447.

Mikhaltsevitch, V. , M. Lebedev, and B. Gurevich. 2014. " A laboratory study of low-frequency wave dispersion and attenuation in water-saturated sandstones." The leading edge, special section: attenuation dispersion. 614-622.

Mora, P. 1987. "Nonlinear two-dimensional elastic inversion of multioffset seismic data." Geophysics 52 (9):1211–1228.

Müller, T.M., B. Gurevich, and M. Lebedev. 2010. " Seismic wave attenuation and dispersion due to wave-induced flow in porous rocks—a review." Geophysics 75:147-164.

Norose, Y., K. Mizutani, N. Wakatsuki, and T. Ebihara. 2015. "Noise reduction in ultrasonic computerized tomography by preprocessing for projection data." Japanese Journal of Applied Physics 54:1-4.

Nourifard, N., and M. Lebedev. 2018. "Research note: the effect of strain amplitude produced by ultrasonic waves on its velocity." Geophysical Prospecting:1-8.

Nzikou, M.M., A. Yurikov, M. Madadi, M. Lebedev, and B. Gurevich. 2018. "Forward and inversion modelling of the ultrasonic wave in a homogeneous medium using P-wave transducers." ASEG Extended Abstracts 1 (1):1-7. doi: https://doi.org/10.1071/ASEG2018ABP074.

Olympus, NDT. 2007. "Advances in Phased Array Ultrasonic Technology Applications."

Operto, S., Y. Gholami, V. Prieux, A. Ribodetti, R. Brossier, L. Metivier, and J. Virieux. 2013. "A guided tour of multiparameter full-waveform inversion with multicomponent data: from theory to practice." Leading Edge 32 (9):1040–1054.

Page, J.H. , J. Liu, B. Abeles, E. Herbolzheimer, H.W. Deckman, and D.A. Weitz. 1995. "Adsorption and desorption of a wetting fluid in Vycor studied by acoustic and optical techniques." Phys. Rev. 52:2763.

Pan, Z., and L.D. Connell. 2007. "A theoretical model for gas adsorption-induced coal swelling." International Journal of Coal geology 69 (4):243-252.

Peiró, J., and S. Sherwin. 2005. "Handbook of Materials Modeling." Methods and Models 1.

Peterseim, D. , and M. Schedensack. 2007. "Relaxing the CFL condition for the wave equation on adaptive meshes." J. Sci. Comput. 72:1196. doi: https://doi.org/10.1007/s10915-017-0394-y.

Pevzner, R. , T.M. Müller, R.J. Galvin, and B. Gurevich. 2012. "Estimation of 558 attenuation from zero-offset VSP data: CO2CRC Otway Project case study." SEG Technical 559:1-6. doi: https://doi.org/10.1190/segam2012-0950.1.

Pimienta, L., J. Fortin, and Y. Gueguen. 2014. "Investigation of elastic weakening in limestone and sandstone samples from moisture adsorption." Geophysical Journal International 199:335-347.

Pimienta, L., J. Fortin, and Y. Gueguen. 2015. "Experimental study of Young's modulus dispersion and attenuation in fully saturated sandstones." Journal of Geophysics 80:57-72.

Qi, H., H. De-Hua, and L. Hui. 2015. "Laboratory measurement of dispersion and attenuation in the seismic frequency." SEG New Orleans:3090-3094.

Quan, Y., and M.J. Harris. 1997. "Seismic attenuation tomography using the frequency shift method." Geophysics 62:895–905.

Ramsay, J.G., and R.J. Lisle. 2000. "The Techniques of Modern Structural Geology Volume 3: Applications of Continuum Mechanics in Structural Geology." Academic Press, London:346 pp.

Rasolofosaon, P.N.J. , and B.E. Zinszner. 2014. "Petroacoustics - A tool for applied seismic, Chapter 2 on “Laboratory measurements”." EDP Sciences.

Rouquerol, J., F. Rouquerol, P. Llewellyn, G. Maurin, and K.S.W. Sing. 2013. "Adsorption by powders and porous solids: principles, methodology and applications." Academic Press, London 2:647p.

Saether, M., P. Lunde, and G. Ersland. 2016. "Sound velocity measurement methods for porous sandstone. Measurements, finite element modelling, and diffraction correction." Proceedings of the 39th Scandinavian Symposium on Physical Acoustics (arXiv:1604.02255):1-28.

Sams, M., and D. Goldberg. 1990. "The validity of Q estimates from borehole data using spectral ratios " Geophysics 55:97–101.

Sato, K., and A. Yamaji. 2006. "Uniform distribution of points on a hypersphere for improving the resolution of stress tensor inversion." Journal of Structural Geology 28 (972–979).

Schappert, K., and R. Pelster. 2014. "Influence of the Laplace pressure on the elasticity of argon in nanopores." EPL 105:56001.

Shan, Y., F. Gong, Z. Li, and G. Lin. 2007. "A grid-search inversion method looking for the best classification of polyphase fault/slip data." Tectonophysics 433:53-64.

Sharma, A., and G. Kumaraswamy. 2018. "Modeling the universal viscoelastic response of polymer fibers." Physical Review Materials 2:1-6.

Shin, C., D. Min, K.J. Marfurt, H. Lim, D. Yang, Y. Cha, S. Ko, K. Yoon, T. Ha, and S. Hong. 2002. "Traveltime and amplitude calculations using the damped wave solution." Geophysics 67:1637-1647.

Shragge, J., T.E. Blum, K.V. Wijk, and A. Ludmila. 2015. "Full-wavefield modelling and reverse time migration of laser ultrasound data: A feasibility study." Geophysics 80 553-563.

Shukui, L., Z. Jinying, and W. Ziyan. 2015. "Implementation of coda wave interferometry using Taylor series expansion." J. Nondestruct. Eval.:34-25.

Sirgue, L., J. Etgen, and U. Albertin. 2008. "3D frequency-domain waveform inversion using time-domain finite-difference methods." 70th EAGE Extended Abstracts:p. F022.

Siva, S., R. Shashidhara, B. Krishnan, C. Krishnamurthy, and M. Shankar. 2005. "Ultrasonic goniometry immersion techniques for the measurement of elastic moduli." Composite Structures 67:3-17.

Smith, M. 2014. "Abaqus/Standard User's Manual 6.9. ." RI: Simulia.

Spencer, J. W. Jr. 1981. "Stress relaxation at low frequencies in fluid-saturated rocks: Attenuation and modulus dispersion." Journal of Geophysical Research: Solid Earth 86:1803–1812.

Sun, L., B. Milkereit, and D.R. Schmitt. 2009. "Measuring velocity dispersion and attenuation in the exploration seismic frequency band." Geophysics 74:113-122.

Swann, W.H. 1972. "Direct search methods." In Murray, W. (ed.). Numerical Methods for Unconstrained Optimization. New York: Academic Press. 13-28.

Tarantola, A. 1986. "A strategy for nonlinear elastic inversion of seismic reflection data." Geophysics 51 (10):1893–1903.

Thierry, P., and G. Lambare. 1995. "2.5D true-amplitude migration on a workstation." 65th Annual International Meeting, SEG, Extended abstract (156-159).

Toms, J. , T.M. Müller, and B. Gurevich. 2007 "Seismic attenuation in porous rocks with random patchy saturation." Geophys. Prospect. 55 (671-678).

Toms, J., T.M. Muller, and B. Gurevich. 2007. "Seismic attenuation in porous rocks with random patchy saturation." Geophysical Prospecting 55:671-678.

Tonn, R. 1991. "The determination of the seismic quality factor Q from VSP data: A comparison of different computational methods." Geophysical Prospecting 39:1–27.

Trefethen, L.N. 1996. Finite Difference and Spectral Methods for Ordinary and Partial Differential Equations: The author.

Vappou, J., C. Maleke, and E. Konofagou. 2009. "Quantitative viscoelastic parameters measured by harmonic motion imaging." Phys. Med. Biol 54:3579-3594.

Vernik, L., and A. Nur. 1992. "Ultrasonic velocity and anisotropy of hydrocarbon source rocks." Geophysics 57:727-735.

Vigh, D., K. Jiao, D. Watts, and D. Sun. 2014. "Elastic full-waveform inversion application using multicomponent measurements of seismic data collection." Geophysics 79 (2):63–77.

Wang, T.F., and J.B. Cheng. 2017. "Elastic full waveform inversion based on mode decomposition: the approach and mechanism." Geophys. J. Int. 209:606-622. doi: 10.1093/gji/ggx038.

Wang, Y. 2015. "Frequencies of the Ricker wavelet." Geophysics 80:31-37.

Wang, Z., R. Wang, T. Li, and D.R. Schmitt. 2016. "Modelling of viscoelastic properties of porous rocks saturated with viscous fluid at seismic frequencies at the core scale." 2016 SEG Rock physics & Borehole Geophysics Workshops:9-12.

Wei, Q., D.H. Han, Q. Huang, M. Sun, and H. Yuan. 2017. "Laboratory measurements of velocity dispersion and wave attenuation in water saturated sandstones at low frequency." SEG International Exposition 87:3569-3573.

Yoshimitsu, N., T. Furumura, and T. Maeda. 2016. "Geometric effect on a laboratory-scale wavefield inferred from a three-dimensional numerical simulation." J. Appl. Geo. 132:184-192.

Yurikov, A., M. Lebedev, G. Gor, and B. Gurevich. 2018. "Sorption-Induced Deformation and Elastic Weakening of Bentheim Sandstone." Journal of Geophysical Research: Solid Earth. doi: 10.1029/2018JB016003.

Zhang, Q., and G.A. McMechan. 2010. "2D and 3D elastic wavefield vector decomposition in the wavenumber domain for VTI media." Geophysics 75 (3):D13–D26.

Zienkiewicz, O.C., R.L. Taylor, and J.Z. Zhu. 2013. "The finite element method: its basis and fundamentals (7th edition)." Oxford Butterworth-Heinemann.